University of Arkansas, Fayetteville

ScholarWorks@UARK

5-2015

Numerical Modeling of Fluid Migration in Hydraulically Fractured Formations

Toyin Christie Aseeperi
University of Arkansas, Fayetteville

Numerical Modeling of Fluid Migration in

Hydraulically Fractured Formations

Numerical Modeling of Fluid Migration in Hydraulically Fractured Formations

A dissertation submitted in partial fulfillment
of the requirements for the degree of
Doctor of Philosophy in Chemical Engineering

by

Toyin Christie Aseeperi
Obafemi Awolowo University
Bachelor of Science in Chemical Engineering, 2008

May 2015
University of Arkansas

This dissertation is approved for recommendation to the Graduate Council.

_____
Dr. Gregory J. Thoma
Dissertation Director

_____   _____
Dr. Jackson D. Cothren   Dr. Ralph E. Davis
Committee Member   Committee Member

_____   _____
Dr. Jerry A. Havens   Dr. Richard R. Ulrich
Committee Member   Committee Member

ABSTRACT

Economic production from low permeability shale gas formations has been made possible by the introduction of horizontal drilling and hydraulic fracturing. To ensure that gas production from these formations is optimized and carried out in an environmentally friendly approach, knowledge about the patterns of gas flow in the shale reservoir formation is required.

This work presents the development of a shale gas reservoir model for the characterization of flow behavior in hydraulically fractured shale formations. The study also seeks to develop more computationally efficient approaches towards the modeling of complex fracture geometries. The model evaluates the migration patterns of gas in the formations, and investigates the range of physical conditions that favor the direction of gas flux towards the wellbore and decreases the probability of gas escape into the overlying formation.

Two conceptual models that bypass the need for explicit fracture domains are utilized for this study, the semi-explicit conceptual model and the fractured continuum model. Fracture complexity is accounted for by modeling induced secondary hydraulic fractures. A novel approach to modeling the secondary fractures, which utilizes asymmetrical fractal representations is also implemented, and the governing equations for flow in the system are solved numerically using COMSOL Multiphysics 4.4b, a finite-element analysis software package. A parametric study is conducted on the reservoir and fracture properties and an assessment of their impacts on the production and formation leak off rates examined.

The study results are presented and analyzed using a combination of transient pressure surface maps, production rate data curves and transient velocity distribution maps. Optimization of gas production rates from the studied formation is shown to be achievable by the use of long lateral fractures placed orthogonal to the wellbore. There is a need for an accounting of the distinct fracture systems present in a fractured formation for the accurate prediction of production values

and flow patterns arising in the formation. This work extends the understanding associated with shale gas reservoir modeling and demonstrates the applicability of the fractured continuum model approach for the simulation of complex fractured shale formations.

ACKNOWLEDGEMENTS

DEDICATION

This dissertation is dedicated to God, my family, and my friends.

TABLE OF CONTENTS

Abstract

Acknowledgements

Dedication

Table of Contents

List of Figures

List of Tables

Nomenclature

Abbreviations

LIST OF FIGURES

LIST OF TABLES

NOMENCLATURE

Symbol	Meaning	Units
∇	gradient operator	-
∇_T	tangential gradient operator	-
θ	reservoir porosity	1
ϕ	first fractal rotation angle	rad
χ	second fractal rotation angle	rad
λ_i	kriging weights	-
ω_f	fracture volume fraction	1
∂_{ij}	kronecker delta	-
μ	fluid viscosity	$ML^{-1}T^{-1}$
A_{perf}	area of perforated region	L^2
b	fracture aperture	L
C	cubic law constant.	
C_f	isothermal compressibility of a gas	$M^{-1}LT^2$
d_f	distance between the center points of two primary fractures	L
$dl.U$	velocity magnitude	LT^{-1}
d_{sf}	extent of secondary fractures in the direction of the wellbore	L
d_{sr}	extent of radial fractures	L
$dV^{(f)}$	volume of a fracture	L^3
F	fluid source term	LT^{-1}

f	subscript to denote fracture	-
g	gravity	L/T^2
h	reservoir height	L
J	field gradient in fluid flow direction	LT^{-1}
k	intrinsic permeability of the soil or rock	L^2
$\bar{k}(x)$	mean of property value k	-
K	hydraulic conductivity	LT^{-1}
l	length of mesh element edges.	L
L_y	reservoir-extent in the y-direction	L
m	subscript to denote matrix	-
mD	millidarcy – unit of permeability	L^2
$mesh\_q$	mesh quality	1
M	molecular mass of the gas	M
M_p	amount of gas present in the formation pore space.	M/L^3
M_s	amount of gas adsorbed to the rock	M/M
MMscf	million standard cubic feet – units of production	L^3
nl	number of fractal lines	-
$\mathbf{n}$	normal vector operator	-
N	number of subdomains	1
ρ	fluid density	ML^{-3}
ρ_k	rock bulk density	M/L^3
p	pressure	$ML^{-1}T^{-2}$

psi	pound force per square inch – units of pressure	$ML^{-1}T^{-2}$
P_L	Langmuir pressure	$ML^{-1}T^{-2}$
P_{ij}	crack tensor.	L^2
$q_{wellbore}$	flux at wellbore	L^3T^{-1}
Q	volumetric flow rate	L^3T^{-1}
r	number of interpolation points	1
r_well	wellbore radius	L
R	Ideal gas Constant	
S_s	Specific storage of the rock	L^{-1}
t	time	T
T	formation temperature	Θ
T_f	transmissivity	L^2T^{-1}
ups	subscript denoting upscaled properties	-
v	velocity of the fluid	LT^{-1}
$v_i^{(f)}$	velocity in a fracture	LT^{-1}
vol	volume	L^3
V_L	Langmuir volume	L^3/M
V_{ads}	adsorbed volume	L^3/M
w_f	hydraulic fracture width	L
Xmax	upper boundary of subdomain bounding box in x-direction	L
Xmin	lower boundary of subdomain bounding box in x-direction	L

y_f	extent of primary (hydraulic) fracture in the y-direction	L
$Ymax$	upper boundary of subdomain bounding box in y-direction	L
$Ymin$	lower boundary of subdomain bounding box in y-direction	L
y_{sf}	extent of the secondary fractures in the y-direction	L
$Zmax$	upper boundary of subdomain bounding box in z-direction	L
$Zmin$	lower boundary of subdomain bounding box in z-direction	L
Z	gas pressure compressibility factor	1

ABBREVIATIONS

2-D	Two dimensional
3-D	Three dimensional
BDF	Backward Differentiation Formula
CEFoR	Center for Engineered Fracturing of Rock
DFN	Discrete Fracture Network
DOE	Department of Energy
ECM	Equivalent Continuum models
IEA	International Energy Agency
KGD	Kristonovich-Geertsma-Daneshy
NF	Natural Fractures
NRDC	National Research and Development Center
OECD	Organization for Economic Co-operation and Development
PKN	Perkins-Kern-Nordgren
REV	Representative Elementary Volume
US	United States

CHAPTER 1

INTRODUCTION

1.1.   Unconventional Gas

Natural gas is one of the major sources of energy in the United States (US), and it contributes about 22% of the country's domestic energy resource (OECD/IEA, 2012). The gas-which is part of the petroleum fluids formed as a result of thermal maturity of organic matter sediments that are deeply buried in the subsurface, can be found in both conventional and unconventional formations. Conventional formations are also referred to as reservoir rocks. They are typically a high porosity and high permeability rock formation that allow for ease of production and development but represent a small proportion of the total oil and gas reserves. Unconventional gas resources – including tight sands, coal-bed methane, and gas shales – constitute some of the largest reserves of unexploited natural gas resources. They tend to have enormous concentrations of the resource, occur in fine-grained low permeability rocks i.e. lower quality formations, and most importantly, they cannot be recovered economically without application of improved stimulation, extraction or recovery technologies. The relationship between conventional and unconventional resources can be visualized by the resource triangle in **Figure 1.1**.

Unconventional gas resources represent a potential long-term global resource of natural gas. These resources are particularly attractive to natural-gas producers due to their production life and stabilizing influence on reserve portfolios. Outside the US, with a few exceptions, unconventional gas resources have largely been overlooked and understudied. Activities required to produce gas from this sources has been previously considered as impractical because of the very poor permeability of the rock.(Chianelli et al., 2011; Rao, 2012)

1

However, research and development into the geological controls and production technologies for these resources during the past several decades has enabled operators in the US to begin to unlock the vast potential of these challenging resources. These technological advancements have resulted in a substantial increase in economically recoverable reserves that were previously thought to be uneconomic. This in turn has led to an increase in the amount of natural gas reserves the country has discovered and produced since its almost nonexistent production levels in the early 1970s. Unconventional resources have since become an important component of the US domestic natural-gas supply base for many years and the volumes of gas produced from unconventional resources in the US are projected to increase in importance over the next 25 years. In the year 2010 alone, unconventional gas accounted for 50% of the estimated recoverable reserves and nearly 60% of total gas production in the US (OECD/IEA, 2012)– See **Table 1. 1**
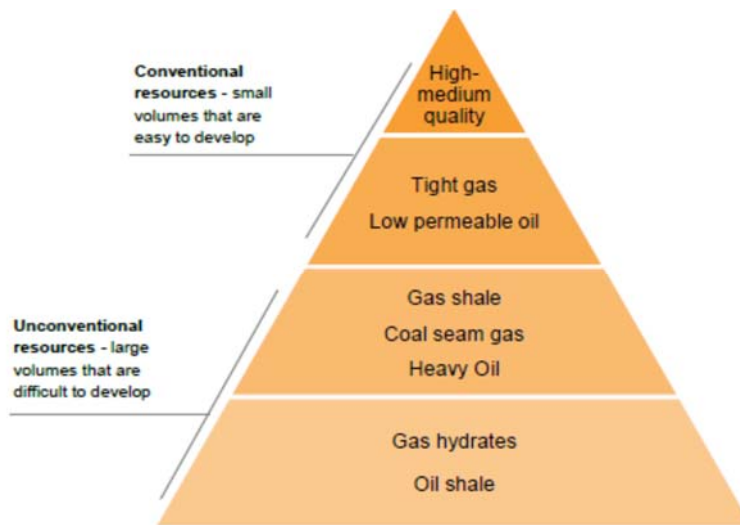
Figure 1.1   The Resource Triangle (IEA, 2012 'Golden Rules for a golden Age of Gas: World Energy Outlook Special Report on Unconventional Gas')

Table 1.1 **Remaining recoverable natural gas resources and production by type in the United States (OECD/IEA, 2012)**

	Recoverable resources (tcm)		Production (bcm)		
	End-2011	Share of total	2005	2010	Share of total (2010)
Unconventional gas	37	50%	224	358	59%
Shale gas	24	32%	21	141	23%
Tight gas	10	13%	154	161	26%
Coalbed methane	3	4%	49	56	9%
Conventional gas	37	50%	288	251	41%
Total	**74**	**100%**	**511**	**609**	**100%**

Sources: IEA analysis and databases.

1.2. Shale Formations

Shale accounts for more than half of the earth's sedimentary rock and includes a wide variety of vastly differing formations that range from the organic rich, fine-grained rocks of the Antrim Shale in the Michigan Basin to the variable facies rocks of the Lewis Shale in the San Juan Basin(Seto, 2011). Gas shales refer to fine-grained geological rock formations rich in clays which are capable of storing significant amounts of gas, that have been produced by the thermal transformation and maturation of fine organic sediments deposited in a low energy and fairly quiet environments, such as a tidal flat or a deep-water basin. These organic-rich formations were previously believed to function as source rocks and seals for gas accumulating in stratigraphically

proximal sandstone and carbonate reservoirs of otherwise conventional onshore gas developments (Frantz and Jochen, 2005; OECD/IEA, 2012).

Shale gas reservoirs are typically comprised of two distinct porous media: the shale matrix containing the majority of gas storage in the formation but with a very low permeability and the fracture network with a higher permeability but low storage capacity. Natural gas in shale reservoirs is believed to be stored as "free gas" in both shale matrix and natural fracture system, and as "adsorbed gas" on the surface of matrix particle i.e. there are three distinct forms in which shale gas can be present in the formation: as free gas in rock pores, free gas in natural fractures, and adsorbed gas on organic matter and mineral surfaces. These different storage mechanisms affect the speed and efficiency of gas production(Song, 2010).

Unlike conventional gas accumulations which exist in discrete fields, – i.e. the boundaries of the reservoir are defined over a limited area - gas saturations in shales exist over a wide area, making exploration risk associated with these plays very low. The rock is characterized by low porosity (usually less than 10% of the total volume) and low permeability (micro- to nano-darcy range). The permeability of shale is about one-millionth that of a conventional gas reservoir rock, and as such, specific technologies need to be utilized to achieve commercial gas flow rates. The low recovery rates from shale formations are also dependent on the porosity controls of the rock formation, as the gas is usually trapped within the limited disconnected pore spaces or present mostly in the adsorbed form (Cipolla et al., 2009; Seto, 2011; OECD/IEA, 2012; Rao, 2012) .

Shale gas accounts for a huge part of the unconventional gas resources present and produced in the US (as reported in **Table 1**), and the production of natural gas from shale is one of the most rapidly expanding trends in the onshore gas industry. This increased activity is made possible because of the discovery and implementation of improved exploration techniques to

recover the gas i.e. horizontal drilling and hydraulic fracturing; as well as, the favorable economics

that has been associated with natural gas production (Arthur et al., 2008; Soeder, 2012) **Figure 1.2**

shows the approximate locations of producing and prospective gas shales across the United States.
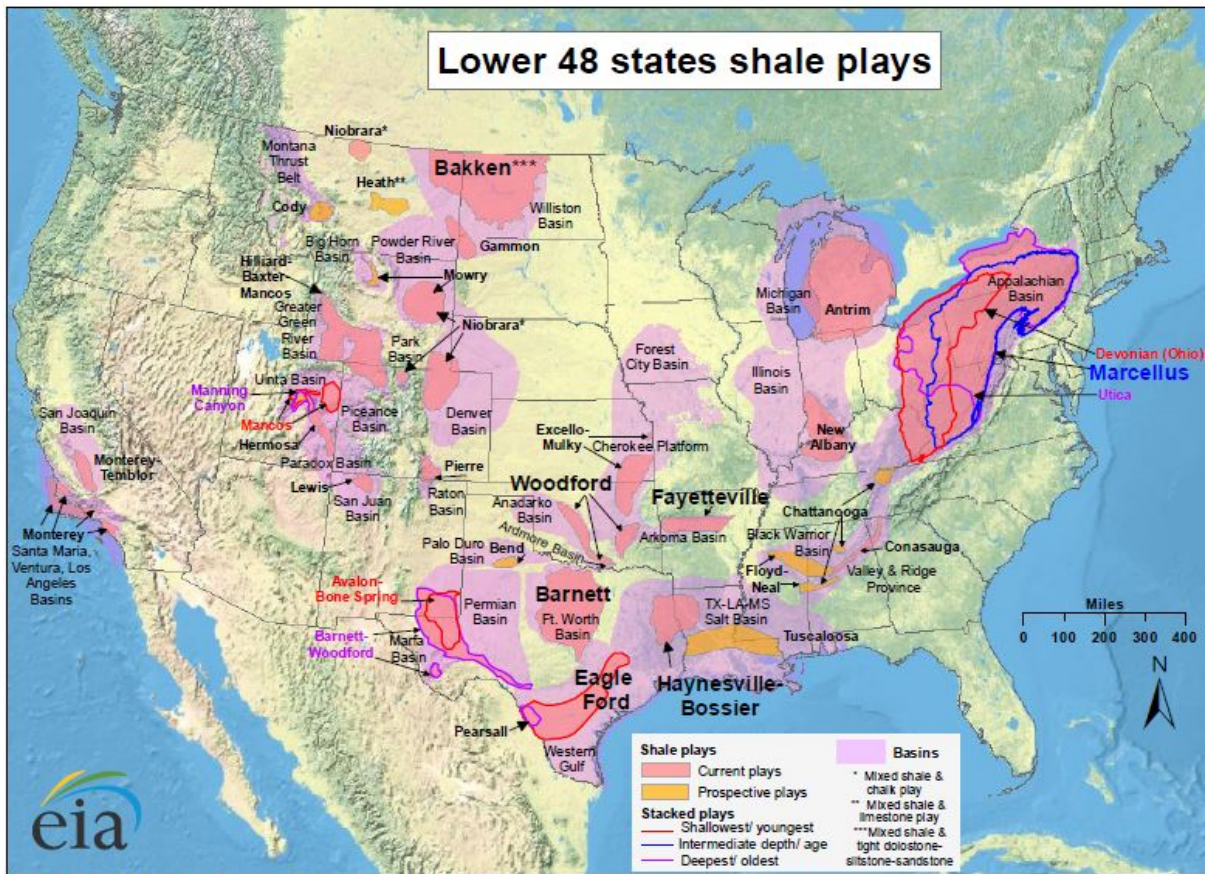
Figure 1.2   Map of Shale Gas Basins in the Lower 48 states (EIA 2012)

1.3. Hydraulic Fracturing

Over the years, a variety of technologies have been developed to enhance flow from low permeability reservoirs. These include acid injection procedures, which involve the treatment of the rock formation to dissolve some of the rock minerals and enhance the rock permeability; horizontal drilling -the use of long lateral sections in order to increase the surface area of the wellbore available for fluid recovery; and hydraulic fracturing – a process that has become the most common technology in recent years (OECD/IEA, 2012).

The process of hydraulic fracturing involves pumping proppant-laden viscous fluid at high rates and high pressures into the rock formation through encased wells. The objective of pumping a fracture treatment is to crack the reservoir rock around the borehole and place proppants, which are typically solid materials in particulate form, in the cracks to keep them open, allowing for the formation of a permeable conduit through which the rock can release its gas. The newly fractured formation has an increased effective permeability and thus enhances fluid flow and recovery to the wellbore (Veatch et al., 1989; Taleghani, 2009; ALL Consulting, 2012).

Fracturing is an enhanced oil recovery technique used as a means of stimulating flow in wells with declining production rates. The process dates back to the 1860s, when an explosive such as nitroglycerin was employed to break up the rock to increase oil flow rates. Although the increased recovery desired was achieved, the hazardous nature of the process inspired studies on safer approaches to fracturing, and in 1947, the first experimental hydraulic fracturing job-utilizing gelled gasoline and sand as the fracking fluid-was conducted by Stanolind oil in the Hugoten gas field in Kansas. With over 60 years of commercial utilization, and about a million oil and gas wells fractured in the United States alone, hydraulic fracturing has matured into a highly

developed technology, estimated to account for about 70% of North America's future natural gas development (NPC, 2011; OECD/IEA, 2012).

Hydraulic fracturing stimulations are varied. The type of stimulation depends on the geometry of the well as well as the type of resource being stimulated. Conventional hydraulic fracture treatments requiring the use of high viscosity fluids containing high concentrations of proppant are utilized to produce short wide fractures and bypass near well bore damage in small scale fracturing operations in high-quality reservoirs such as sandstone and carbonate units. Stimulation treatment in low quality reservoirs such as coal and shale gas however, makes use of large volumes of low viscosity fluids like water, with low proppant loading, at high pressures (typical pressure levels to fracture a shale rock is about 10,000 pounds per square inch), as the process is performed in multiple stages and combined with horizontal well drilling in order to promote fracture complexity and increase wellbore exposure to the reservoir. The amount of water used depends on the nature of the sub-surface. A well can require between 2 and 8 million gallons of water for a fracturing job. The fractures produced are typically long and thin(Song, 2010; Linkov, 2012; Todd Energy, 2012).

1.4.   Concerns about Hydraulic Fracturing

The increased activity associated with shale gas development using the hydraulic fracturing process has resulted in significant amount of public concern about the environmental effects of the technology.   These effects could be short term and acute, i.e. impacts related to the well construction phase such as water withdrawals and noise from drilling operations, or they could be long term effects, which are usually chronic, such as groundwater contamination (Clark et al., 2012; Soeder, 2012). In the US, where high volume water fracturing is utilized, depletions of the

ground water resource is one of such concerns. Ground water depletion can occur if more water is discharged than recharged. Large withdrawals of ground water during these times can cause the water table to fall and lead to a depletion of the aquifer. Also, ground water can become unusable if it becomes polluted and is no longer safe to drink. This occurs in areas where the material above the aquifer is permeable, allowing pollutants to seep into ground water.

A frequently expressed concern about shale gas development is that during hydraulic fracturing operations in deep shale, developers do not have complete control over where fractures will develop; therefore methane, contaminants naturally occurring in formation water, and fracturing fluids tend to migrate from the target formation into aquifers and drinking water supplies. The high pressure exerted during hydraulic fracturing and deep-well injection processes can force the toxic fluids up through any existing uncapped wells, contaminating aquifers and drinking wells (US DOE, 2009; Todd Energy, 2012). Results from a 2007 Penn State study of 200 water wells near oil and gas wells found 8% contaminated (NRDC, 2002). Evidence of water movement through unsaturated fractured rocks over vertical distances of several hundred meters and at velocities of an order of 10m/year or more, has also been observed from environmental tracers placed at a potential site for a high level nuclear waste repository at Yucca Mountain (Pruess, 2001), indicating the potential for significant subsurface migration of fluids in a fractured formation.

Hydraulic fracturing does induce new fractures into shale, and can propagate fractures thousands of feet along the bedding plane of a shale formation. Typical unfractured shales have matrix permeabilities on the order of 0.01 to 0.00001 millidarcies, in contrast, field determinations of permeability of fractured shales has been found to yield permeability values close to what is obtained for sandstone i.e. 10 to 10000 millidarcies (Chiles and de Marsily, 1993).

Concerns about potential free gas migration however, seem to be a more pressing issue in recent times. This is justifiable by the fact that the gas phase migrates much faster than the liquid phase in porous formations and this movement can be further enhanced by the presence of fractures, as flow in fractures is known to be orders of magnitude faster than flow in the porous matrix. While it has been argued that vertical separation distance and low permeability of intervening rock layers reduces the chances of ground water contamination from shale gas development techniques (See **Figure 1.4**), state regulators have not been able to disprove a connection between hydraulic fracturing and water contamination.
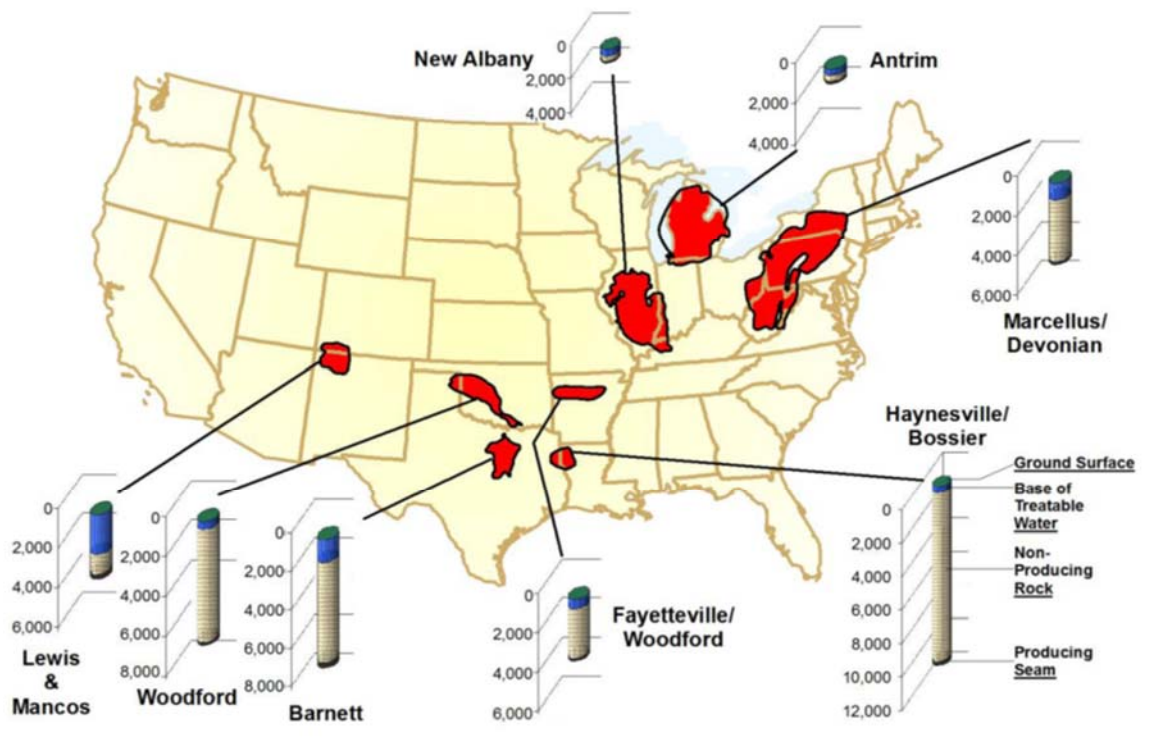
Figure 1.4   Target Shale Depths and Base of Treatable Groundwater in Select Shale Plays – distances shown in field units (US DOE, 2009)

1.5. Objectives of this Project

While innovative solutions are emerging which allow for rapid commercialization of shale gas, attending concerns about the migration patterns of fluids in the fractured formation i.e. stray gas, formation brines, and hydraulic fracturing fluids, as well as a lack of information about the linkages or consequences that this enhanced production has on the ground water resources have also grown alongside these developments. In ensuring that recoverability of gas from unconventional reservoirs is optimized and carried out in a most environmentally friendly approach, adequate knowledge about the patterns of gas flow in the shale reservoir formation is required.

The overall objective of this project is to evaluate the migration patterns of the gas present in the shale formation i.e. the free gas now exposed in the system as a result of hydraulic fracturing. This study also aims to investigate the range of physical conditions that favor the direction of gas flux towards the wellbore - and by so doing enhances gas production from the host rock and decreases the probability of gas escape into the overlying formation. The motivations of the study were modified into specific objectives stated below:

- Utilize COMSOL to predict migration patterns of shale gas in fractured media
- Estimate the effect of fracture network patterns on flow in simulated geometry
- Utilize an appropriate multi-physics boundary condition to estimate and model possible gas flux out of the system

The steps involved in the modeling process are:

- Conceptual model formulation of fractured formation
- Generation of three dimensional fracture patterns to represent expected fracture characteristics.

10

- Solution of flow and pressure fields in the model domain.

On implementation of these steps, the gas velocities and migration paths within the formation being modeled will be determined. The model is then re-simulated for different fractured strata configurations, and the estimated values averaged to get the effective values that are representative of the system within acceptable limits.

The tendency for fracture networks to be asymmetrical as they interact with natural fractures in the formation has been discussed in literature, (Bennet et al., 2005; Dershowitz and Doe, 2011) however the use of asymmetrical fractal patterns to represent the complexity of fractures originating from wellbore formations has not been presented so far in literature. This is a problem of significant interest to shale gas operators, regulators and the members of the communities who are interested in getting access to accurate information about the effects of hydraulic fracturing.

Fear of the unknown risks caused by the exploration and exploitation of gas is a major reason for the concerns raised by the public; it is the aim of this work to present a clearer understanding of the subject of gas movements associated with hydraulically fractured formations.

1.6. Outline of Thesis

This dissertation presents the tasks and results associated with research work on the subject of numerical migration of methane through hydraulically fractured formations. This chapter presents an introduction to unconventional gas resources and hydraulic fracturing. The objective of the research, which is born out of concerns associated with the hydraulic fracturing process and the need for a proper understanding of the effects of hydraulic fracturing, is also discussed in this chapter.

Chapter 2 presents the review of literature associated with flow modeling in subsurface formations. Concepts of fluid flow in porous media and in shale formations in particular is discussed. The chapter also provides information about fractures in shale formations and the conceptual models available for their description for flow modeling purposes. The review highlights the need for further research into the development of conceptual models that are capable of handling complex fractured geometries, which is still relatively sparse in literature.

In chapter 3, the sequential approach to the development of the numerical model is presented. The assumptions of the study, conceptual model selection, as well as the procedure for the representation of the fracture networks is discussed. The chapter also gives a brief description of the reservoir simulation software package, the boundary conditions utilized in the study and it ends with a look at how production from the model is estimated.

The results from the numerical studies are analyzed and discussed in chapter 4, showing possible relationships and effects of the reservoir parameters and fracture network configurations on flow through the modeled formation. Chapter 5 presents the conclusions of this study and some recommendations that are suggested for future work.

CHAPTER 2

LITERATURE REVIEW

2.1   Introduction

Fracture flow and characterization has become increasingly important in the wake of the continuous development and stimulation of underground mineral resources for economic purposes. The study of fluid flow in fractured reservoirs is particularly important in a bid to determine a causality or correlative relationship between the introduction and propagation of fractures in the reservoir and the effects it might have on the nearby environment, particularly in geologies that have not been rigorously studied such as shale.

The migration of gas at depth through saturated fractured rock has become increasingly important as a way to assess the performance and safety of radioactive waste disposal sites and of recent to assess the performance and safety of hydraulically fractured production zones (Nuclear Energy Agency, 1992; Gascoyne and Wuschke, 1997). Evidence of water movement through unsaturated fractured rocks over vertical distances of several hundred meters at velocities of an order of 10m/year or more have been observed from environmental tracers placed at a potential site for a high level nuclear waste repository at Yucca Mountain (Pruess, 2001). My intention is to be able to determine if similar migration/response information exists for natural gas movement in shale lithology.

Gas production in subsurface rock formations requires that gas flows towards strategically located wells completed in these formations. Therefore, an understanding of the principles that govern the flow of gas in porous media is essential to determining the depletion of gas from reservoir formations.

2.2   Fluid Flow in Porous Media

The mathematical equations that describe fluid flow and transport processes in porous media may be developed from the fundamental principle of conservation of fluid mass and Newton's second law of motion. Darcy's law is a simplified version of the momentum equation applied to fluid flow. The law has been derived to give a relation between flow rate, pressure forces and gravitational forces.

For the single-phase gas flow case- a condition that is generally prevalent in most reservoir engineering flow problems – the effect of gravitational forces is very small and can be safely ignored. Darcy's law then simplifies to a relation between flow velocity and pressure gradient.

$$v = -\frac{k\rho g}{\mu}\nabla p = K\nabla p \qquad\qquad (2.1)$$

where v is the velocity of the fluid, (LT^{-1})

k is the intrinsic permeability of the soil or rock(L^2),

ρ is the fluid density(ML^{-3}),

μ is the fluid viscosity$(ML^{-1}T^{-1})$,

g is acceleration of gravity(L/T^2)

∇p is the pressure gradient(1), and

K is the hydraulic conductivity (LT^{-1}),

The negative sign in the Darcy's equation implies that flow takes place in the direction of decreasing pressure. The permeability of rocks is usually reported in a field unit called the Darcy.

While it also possesses the same dimensional unit of length^2 as described above, 1 Darcy is equivalent to $1(\mu m)^2$.

The mass conservation equation for steady state flow states that the total mass flux into a certain reference volume must be equal to the mass flux out of the volume. When this law is applied to an infinitesimal Cartesian volume element, it takes the form of a partial differential equation known as the continuity equation that can be stated as:

$$\frac{\partial \rho}{\partial t} + \nabla . (\rho v) = 0 \tag{2.2a}$$

and simplified to give

$$\nabla . (\rho v) = 0 \tag{2.2b}$$

Combining equations (1) and (2) yields the partial differential equation governing 3-dimensional fluid flow in a heterogeneous and anisotropic medium;

$$\frac{\partial}{\partial x}\left(K_{xx}\frac{\partial p}{\partial x}\right) + \frac{\partial}{\partial y}\left(K_{yy}\frac{\partial p}{\partial y}\right) + \frac{\partial}{\partial z}\left(K_{zz}\frac{\partial p}{\partial z}\right) - F = S_s \frac{\partial \rho}{\partial t} \tag{2.3}$$

where,

K_{xx} K_{yy}, and K_{zz} represents the principal components of the hydraulic conductivities in the 3D space(LT^{-1}),

F is the source term for fluid – if present (LT^{-1}),

S_s is the Specific storage of the rock(L^{-1}).   and

$\frac{\partial p}{\partial x}, \frac{\partial p}{\partial y}, \frac{\partial p}{\partial z}$ represent the pressure gradients with respect to the three directions and

$\frac{\partial \rho}{\partial t}$ is the mass accumulation term.

Flow is dependent on the hydraulic conductivities and the pressure gradients in different directions as expressed by equation (2.3). For transient gas flow in deep reservoirs however, the compressibility of the gas contributes to the storativity of the reservoir, and thus the assumptions of fluid incompressibility that may be permissible when studying liquid-groundwater flow cannot be accepted. The density of the gas - which is the parameter that controls the compressibility term, is one that changes with pressure. This pressure-density relationship can be represented in a general form by the equation

$$\rho = \rho(P) \tag{2.4}$$

Because the density depends on pressure, Equation (2.3) becomes non-linear, making a direct analytical solution difficult to obtain. Early attempts to solve gas flow problems in subsurface formations utilized the method of succession of steady states (Muskat, 1946). Other attempts to obtain analytical solutions have since been looked into by Al-Hussainy et al. (1966) and Cornell & Katz (1953). The method of pseudo-pressure function was introduced by (Al-Hussainy et al. (1966) as a way of linearizing the equations and obtaining more robust mathematical solutions. The pseudo pressure concept makes use of an integral function of pressure, viscosity and the compressibility factor as a way of obtaining an average homogenized property value for the reservoir.

More recent semi-analytic models that utilize the concept of pseudo-pressures have been developed by authors such as Anderson et al. (2010) and Mattar et al. (2008). Their models however cannot accurately handle the high nonlinearities associated with shale gas reservoir modelling as the analytical solutions based on pseudo pressures do not adequately capture the effects of gas desorption or the several non-ideal cases of fracture networks that is encountered in these complex geological formations, that are not present in simple porous media formations.

Numerical simulations utilizing appropriate boundary conditions have therefore being suggested as the best approach to be employed for the solution of the non-linear gas equation in fractured formations, as the fracture properties significantly affect the reservoir performance.

2.3   Fluid Flow in Shale Formations

Shale formations are typically low porosity and low permeability media that serve both as source rock and reservoir rock.   Hydrocarbons are bound to the surface of the rock and also contributes to the total gas content in the reservoir. This hydrocarbon content is referred to as the adsorbed component. While various approaches to the fundamental physics of flow and transport in shale gas reservoirs have been proposed and implemented, the connectivity of the organic and mineral matter is not totally understood (King, 1990; Cipolla et al., 2009; Kalantari Dahaghi and Mohaghegh, 2011; Leahy-Dios et al., 2011).

According to Song (2010), there are two main types of porous media present in gas shales, the pores and the fractures. The primary porosity is made up of very fine pores which provide large surface areas and potential sorption sites where large quantities of gas may be adsorbed. A shale gas formation can therefore be simulated using a triple porosity model, in which the free gas is stored in a double porosity system that consists of the pores and the fractures and gas adsorption is modeled as the third porosity. The solution of the fluid flow equation therefore requires an adequate determination of the fluid storage parameter in the formation.

It has been suggested that fluid flow through porous media may not be the dominant phenomenon governing flow in shale, and that the physics needs to be augmented or completely replaced by other modes of flow such as flow between parallel, and diffusion controlled, thin plates or transport due to diffusion resulting from a concentration gradient, as in coal bed methane

17

formations (Rushing et al., 2008; Mohaghegh, 2013), however recent studies have disproved this assertion by being able to validate field data from shale reservoirs while making use of the Darcy-flow equations for bulk phase matrix transport of the gas (Schepers et al., 2009; Ding et al., 2014; W. Yu et al., 2014).

Gas desorption in matrix pores and fractures   Adsorbed gas & free gas flow in matrix pores   Adsorbed gas & free gas flow in fractures

● Adsorbed gas   ● Free gas   ○ Desorbed gas   ⟶ Desorption   ⟶ Flow in porous media
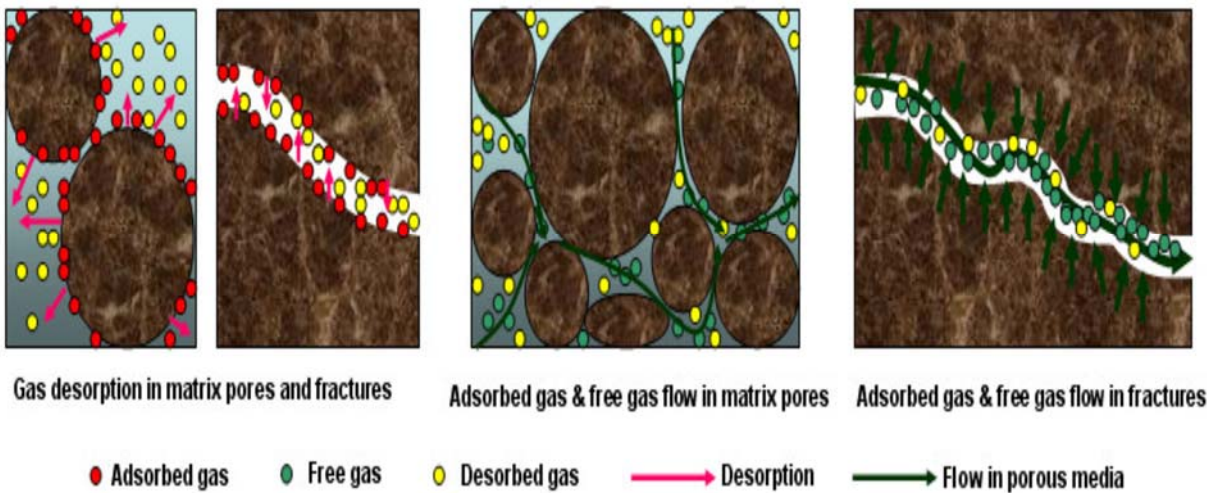
Figure 2.1   Illustration of Gas Transport Mechanism in Gas Shale (Song, 2010)

2.4   Fractures

Bear et al (1993) defined a fracture as part of the void space of a porous medium domain that has a special configuration such that one of its dimensions – the aperture- is smaller than the other two dimensions. The term is usually used to describe a naturally occurring planar discontinuity in rock that is due to deformation or digenesis (Nelson, 2001). It possesses the distinct property of having a high permeability and a low porosity, making it a poor storage medium for fluids but a good conduit for fluid flow (Huyakorn et al., 1983).

18

Fractures can by classified either by their origination mode, the scale of interest at which they are being studied, or by the parameters that govern their distribution. In shale reservoirs, often a combination of natural and hydraulically induced fractures is required for efficient gas production. In terms of scales of interest, a fracture can be classified and characterized as

a. Individual fracture – by specifying its length, orientation, location and aperture

b. A fracture network – by providing information about the number of fractures and its connectivity in the domain.

In **Figure 2.2**, a comparison of these characterizations is shown. Complex fracture networks are desirable in tight shale gas reservoirs because they maximize the contact area available for flow in the reservoir rock due to the associated increase in intensity or size. However, the complexity of a network in itself may or may not lead to increased communication between matrix and fracture blocks, further supporting the need for the detailed study of flow in these media.

a. Simple Fracture   b. Complex Fracture

c. Extremely Complex Fracture Network
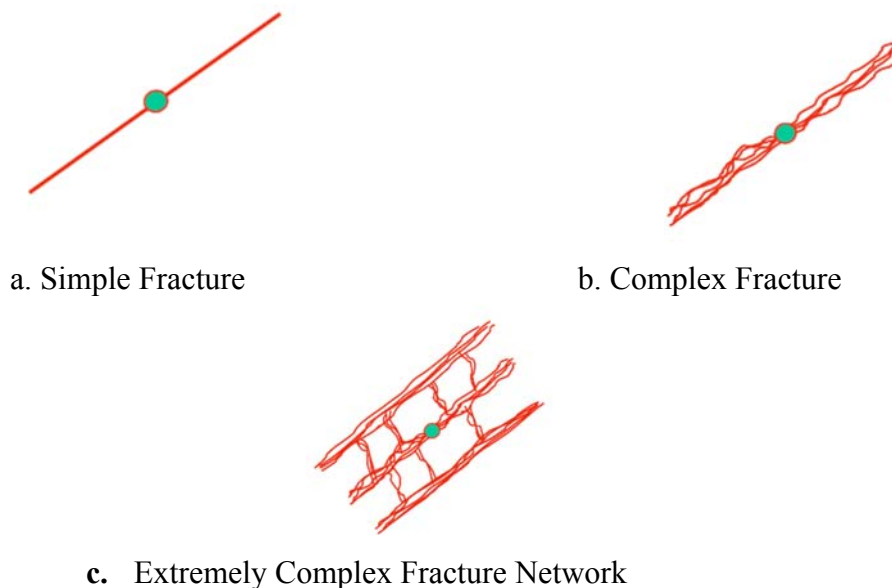
Figure 2.2   Types of fractures as depicted by (Fisher et al., 2004)

According to Warpinski et al. (2009), there is presently no method to predict the network generating capability of a given reservoir; the fracture complexity can only be observed by mapping. However, current mapping technologies do not provide adequate resolution to precisely determine the wellbore to fracture intersection or the details of the fracture geometry at a small scale. In the study conducted by Fisher et al. (2002), generation of fractal networks was carried out by fitting small sequential increments of micro seismic data into a linear regression model to determine the length and orientation of many fracture segments in the order that they are created.

Two widely accepted facts in shale literature (Curtis, 2002; Gale et al., 2007; Kundert and Mullen, 2009; King, 2012; Walton and McLe, 2013) are that:

    i.   The reservoir formation contains natural fractures

    ii.   The hydraulic fracturing process reactivates the natural fractures and opens a new porosity and permeability component in the reservoir.

Moridis et al. (2010) classifies the distinct fracture systems that are observable in a producing shale gas formation into four.

- Natural fractures – these are fractures that are already in the formation before any fracturing or well completion process is carried out. This is discussed further in a later section.

- Hydraulic fractures- these fractures are created by the injection of fracturing fluids into the formation and are used to produce a high permeability pathway in the formation.

- Secondary fractures – these are the fractures that are induced as a result of the changes in the geomechanical state of the rock during hydraulic fracture.

- Radial fractures – these fractures are created as a result of stress effects in the immediate neighborhood of the horizontal well.

A graphical illustration of these systems is presented below:
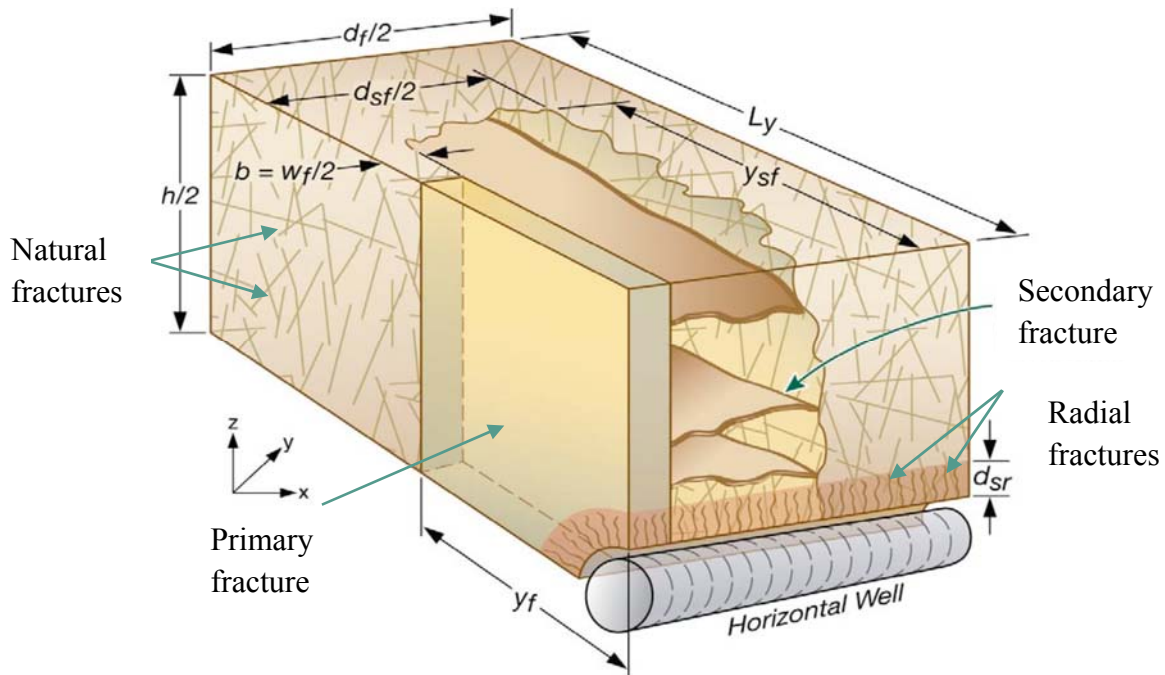
Figure 2.3   Fracture systems present in a shale-gas formation (Moridis et al., 2010)

In the figure above, h is the reservoir height, L_y is the reservoir-extent in the y-direction, d_{sf} is the length/extent of the secondary fractures in the direction of the wellbore, y_{sf} is the extent of the secondary fractures in the y-direction, d_{sr} is the extent of the radial fractures, y_f is the length/extent of the primary (hydraulic) fracture in the y-direction, w_f is the width of the hydraulic fracture, and d_f is the distance between the center points of two primary fractures- a parameter that is required when utilizing symmetry boundaries for modeling purposes.

2.4.1. Natural Fractures

Natural fractures are ubiquitous features that are associated with many reservoir formations and shale in particular. They can be divided into categories, tectonic and non-tectonic. Tectonic fractures tend to be variably oriented and differ both in size and properties on a regional scale. They are related to folding and faulting of the earth crust. Non-tectonic fractures however include joints and weak planes that are related to rock properties and generally have consistent properties such as fracture orientation and permeability, in the region of study. These are the type of fractures observed in shale formations (Fox et al., 2013).

Understanding the mechanism of formation of natural fractures and the histories of the rocks in which they are being formed is helpful in the development of predictive models of natural fracture patterns in the subsurface (Gale et al., 2007). Natural fractures are sometimes observed in outcrops but are more commonly observed when core studies are conducted, thus getting complete data descriptions of the location, extent and properties of these fractures is almost impossible. Due to these data constraints, stochastic representations of the fracture properties which are based on appropriate fracture propagation physics are employed in fluid flow and transport simulations.

The impact of natural fractures in the development of a gas reservoir can be observed in three different ways (Dershowitz and Doe, 2011):

a. Serving as planes of weaknesses that control hydraulic fracture propagation

b. Increased conductivity pathways in the formation as a result of reactivation and slips following a hydraulic fracture

c. Third, natural fractures that were conductive prior to stimulation may affect the shape and extent of a well's drainage volume.

Due to the presence of natural fractures, a fracture treatment in a tight shale formation is more likely to look like the 'very complex' fracture description than the simple case as shown in **Figure 2.2.** This geometry allows for the production of what is referred to as a fracture fairway with many fractures in multiple orientations resulting in large surface areas potentially contributing to production.

2.4.2. Hydraulic Fractures

The hydraulic fracturing process is a computationally complex one to model. This is due in part to the coupling of the physical processes that define the fracture creation process and in part to the heterogeneity of the earth structure. The classical description of a hydraulic fracture was developed from 2-dimensional fracture propagation models and is that of a single bi-wing planar crack with the wellbore at the center of two wings. The most common of these 2-D propagation models, which are being employed for decision making purposes in the hydraulic fracture design industry are the Perkins-Kern-Nordgren (PKN) geometry - which is utilized when the fracture length is much greater than the fracture height-, and the Kristonovich-Geertsma-Daneshy (KGD) geometry, used if fracture height exceeds the fracture length- See **Figure 2.4** (Perkins and Kern, 1961; Geertsma and De Klerk, 1969; Nordgren, 1972). In both cases, an assumption of constant fracture height is used in order to determine other fracture parameters.

The increasing availability of computational resources for numerical simulations however meant that the development of pseudo 3-D or fully 3-D models of hydraulic fracture geometry are being proposed. These 3-D models characterize the fracture as two-semi-ellipses, that originate from the well-bore perforation and are restricted to a plane (Rahman and Rahman, 2010, 2013) as seen in **Figure 2.4c**.
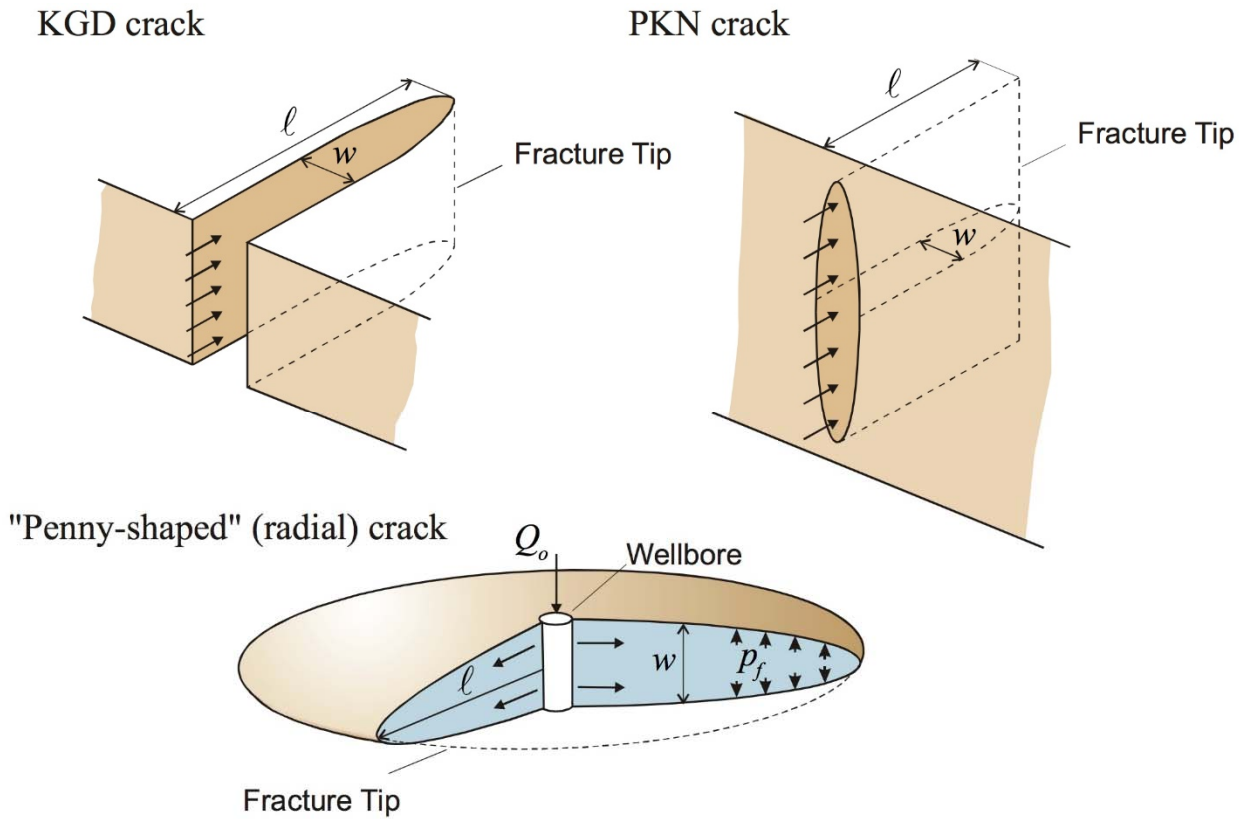
Figure 2.4   Hydraulic fracture models (a) PKN Model (b) KGD Model (c) 3-D radial model (CEFoR, 2012)

Available reservoir simulators that utilize this simplistic elliptical 3-D bi-wing assumption for representing hydraulic fracture geometry in the reservoir exist in fracture simulation literature (Gorocu, 2010; Osholake, 2010; Wang et al., 2013) These models function under the assumption that the geometry of the fracture is easily defined and that the fracture is constrained to a single plane, and are therefore not suitable for modeling fractures in shale gas formations where the broad extension of the fracture network and the nature of fracture growth makes the use of a two-wing model unrealistic. The complex nature of induced fractures in formations containing multiple layers of formation strata and utilizing horizontal wellbores for production is a phenomenon that has been reported by fracture propagation simulation studies. Abass et al. (1996) and Li et al., (2012) present results to show that fractures initiate in a non-preferred direction in a multi-layered formation and then turn and twist during propagation to become aligned with the preferred direction. Also, the complex stress state around a horizontal well or a well that is inclined to the vertical leads to the creation of a complex fracture pattern in the formation.
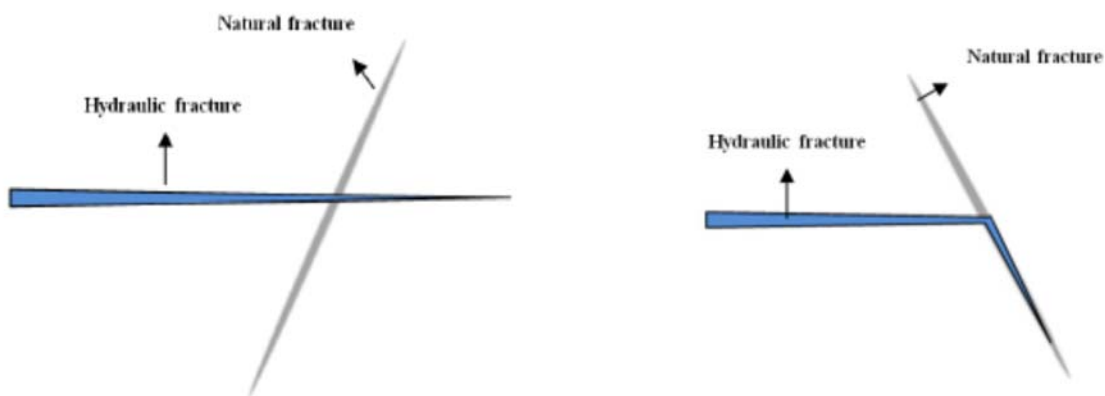
Figure 2.5   Schematic view of hydraulic fracture propagation modes in the presence of natural fractures. In mode (a) the hydraulic fracture crosses the natural fracture without any change in its path and in mode (b), the hydraulic fracture turns into the natural fracture and propagates along it. (Keshavarzi and Jahanbakhshi, 2013)

25

Results of studies presented by Gale et al., (2007) are also supportive of the assumption that in the hydraulic fracturing of deviated wells, fractures sometimes reorient and interact with natural bedding planes and other fractures as they propagate. This interconnection of fractures along existing lines of weakness has been shown to be universal. (Larsen and Gudmundsson, 2010; Li et al., 2012) Thus, a proper understanding of fracture geometry is key to the effectiveness of any stimulation program. A comprehensive study of flow in fractured shale therefore must include geometry elements describing both the natural and the hydraulic fracture components in order to obtain a conceptual model that is most representative of the formation.

Ascertaining the type of fracture geometry created during a hydraulic fracturing process is one that is associated with a high degree of uncertainty. This, in turn means that the definition of permeability pathways in the fracture formations is one that is fraught with uncertainties too. Knowledge of the principles underlying this complex fracture growth is therefore important in creating and visualizing the fracture patterns present in shale reservoirs. However, these principles are still not well understood (Mahrer, 1999; Hossain and Rahman, 2008). To address this challenge, recent modelling approaches that require the use of parametric studies to analyze various complex fracture growth patterns have been proposed in literature (Dong and de Pater, 2001; Zhang and Jeffrey, 2006).

An attempt to study the complexity that is likely to ensue around a hydraulically fractured reservoir well and its effect on production from a reservoir was implemented using a commercial reservoir simulator by Freeman et al. (2008). The geometric complexity introduced in their model included the specification of planar fractures transverse to the wellbore as well as the inclusion of thin lateral secondary fracture layers. While their approach represents an improvement to the study of characteristic fracture geometries in shale formations, the effect of fractal branches that are

oriented at an angle to the formation as well as irregular lengths or patterns of the fracture was not studied.

Yu et al. (2014) also carried out a similar study to investigate the effects of irregular fracture patterns over a small interval of a horizontal wellbore. Their study makes use of planar vertical fracture geometry in which the only controlling factor on the network complexity was the length and placement of fractures around the wellbore. Their results suggest that a difference in the placement of fractures oriented in the same direction around a wellbore can lead to significant differences in gas recovery values after an extended period of production.

In yet another attempt to study complex fracture geometries, Almulhim (2014) carried out a study to evaluate and compare two new stimulation patterns described as the Alternate and the Zipper on production optimization in a fractured formation. Their model like the ones previously reviewed also makes use of simple planar transverse fractures along with the added computational complexity of having to simulate more than one horizontal well in some of their designs.

2.5   Conceptual Models of Fluid Flow in Fractured Media

Conceptual models of flow in fractured media vary in their representation of the heterogeneity of the fractured medium. Fractured media are usually modeled by allowing the porosity and permeability to vary rapidly and discontinuously over the whole domain. Both these quantities are much larger in the fractures than in the blocks of porous rock (Chen et al., 2006). Therefore for accuracy in fluid flow modeling, conceptual models of the fractured porous medium are developed. Three major factors are considered when making the decision of the appropriate conceptual model to be used. They are:

1. The geology of the fractured rock i.e. is the system dominated by few relatively major fractures in a relatively impermeable matrix or does it consist mainly of a system of highly interconnected fractures in a relatively permeable matrix that can be represented as an equivalent continuum.

2. The scale of interest- Depending on whether the system is large scale or small scale, different models can be used to approximate properties of the system. A system that can be represented by a continuum on a large scale may actually be characterized by few relatively large fractures when being considered on a smaller scale.

3. The purpose for which the model is being developed- Relatively coarse model approximations can be used when the goal of the model is to predict an average volumetric flow rate in the fractures. If however, the model development is fueled by concerns about pollutant concentrations, a more refined conceptual model is needed for more accurate predictions.

Based on these factors, the modeling approaches to simulate flow and transport in fracture networks fall into one of three categories within the range of conceptual models for fractured rock: Equivalent Continuum Models (ECM), Discrete fracture networks and Hybrid Models (National Research Council, 1996). These techniques and their key distinguishing parameters as well as references that illustrate recent applications in the modeling approaches are summarized in **Table 2.1**, and will be discussed in detail in the next few sections.

Table 2.1 Classification of Single-phase Flow and Transport Models Based on the Representation of Heterogeneity in the Model Structure -_reproduced with permission from National Research Council._

Representation of heterogeneity	Key parameters that Distinguish Models	Examples
Equivalent Continuum Models *Single porosity*	Effective permeability tensor	Carrera et al.(1990)
	Effective porosity	Davidson (1985)
	Network permeability and porosity	Hseih et al.(1985)
	Matrix permeability and porosity	
Multiple continuum (double porosity, dual permeability, and multiple interacting continuum)	Matrix block geometry	Reeves et al.(1991)
	Non equilibrium matrix and porosity	Pruess and Narasimhan (1988)
Stochastic continuum		
	Geo-statistical parameters for log permeability: mean, variance, spatial correlation scale	Neuman and Depner(1988)
Discrete Network Models	Network geometry statistics	Herbert et al.(1991)
Network models with simple structures	Fracture conductance distribution	
	Network geometry statistics	Sudicky and McLaren (1992)
Network models with significant matrix porosity	Fracture conductance distribution	
	Matrix porosity and permeability	Dershowitz et al. (1991a)
Network models incorporating partial relationships between fractures	Parameters controlling clustering of fractures, fracture growth, or fractal properties of networks	Long and Billaux (1987) Long et al. (1992b)
Equivalent discontinuum	Equivalent conductors on a lattice	
Hybrid Models		
Continuum approximations based on discrete network analysis	Network geometry statistics	Cacas et al. (1990)
	Fracture transmissivity distribution	Oda et al. (1987)
Statistical continuum transport	Network geometry statistics	Smith et al. (1990)
	Fracture transmissivity distribution	
Fractal Models		Long et al. (1992)
Equivalent discontinuum	Fractal generator parameters	Chang and Yortsos (1990)

2.5.1. Equivalent Continuum Models

This group of models are based on the assumption that the different zones in the formation can be represented by continuum sections where the flow and transport properties can be obtained by average representative properties. For the single porosity/single continuum model case, the fractures are assumed to be sufficiently ubiquitous and distributed in a manner that can be meaningfully described statistically. The technique treats the fractured rock system as if it were an unconsolidated porous medium. Bulk parameters for the permeability of the rock mass are used, and the geometry of individual fractures or the rock matrix is not considered. This is a reasonable approach if fracturing is intense or the study domain is sufficiently large such that individual fractures have no influence on the overall flow system.

The approach plays down on the importance of the individual fractures and their significance becomes secondary to the significance accorded the average fracture properties (Pinder et al., 1993). For a system in which the number of heterogeneous regions is large however, a Representative Elementary Volume (REV) must be distinguished if the results of the EPM model computations are to be accepted. The volume of interest (REV), is considered to be large enough that, on average, the permeability can be assumed as the sum of fracture and porous media permeability- an approximation which simplifies the flow problem immensely (Pankow et al., 1986; Diodato, 1994).

The transient three dimensional fluid flow equation in a heterogeneous and anisotropic medium described in (3b) is to be solved in ECM systems, and is re-presented here.

$$\frac{\partial}{\partial x}\left(K_{xx}\frac{\partial p}{\partial x}\right) + \frac{\partial}{\partial y}\left(K_{yy}\frac{\partial p}{\partial y}\right) + \frac{\partial}{\partial z}\left(K_{zz}\frac{\partial p}{\partial z}\right) - F = S_s\frac{\partial \rho}{\partial t}$$

The terms K_{xx}, K_{yy}, and K_{zz} are now the effective hydraulic conductivities in the principal directions. These values are determined by getting average values of the contributions of the fracture network and the porous block to the overall effective conductivity.

The suitability of continuum modeling for fractured formations was studied by Pankow et al. 1986. In their study, a formation was said to be amenable to single continuum modeling if it contained a matrix with large porosity and diffusivity values and fracture components with large apertures and small inter-fracture spacing. Their study was carried out on two fractured porous systems with varying characteristics. The results obtained when validated with information from the sites studied confirmed the utility of the approach, as well as its breakdown in a highly heterogeneous formation.

The assumptions of continuum behavior break down in highly heterogeneous media, because the fundamental basis for continuum behavior, i.e., connections exist between all points in the reservoir, is no longer valid in these systems. The dual porosity modeling approach attempts to account for the non-continuum behavior by modeling the system as if it were composed of two interacting continua with different porosities. This approach was first introduced by Barenblatt et al. (1960). The model consists of a set of equations developed for slightly compressible single-phase flow and is written for both the fractures and the matrix. In this approach, equations of flow and transport for each system are linked by a source/sink term that describes the fluid or solute exchange between the two systems each of which may have very different properties relative to the other. This transfer was assumed to occur at pseudosteady state.

A simplification of the governing equations for two dimensional flow in in dual porosity systems developed by Gerke and Van Genuchten, 1993 as described by Lee, 1997 is given below:

$$S_{sf}\frac{\partial h_f}{\partial t} = \frac{\partial}{\partial x}\left(K_f\frac{\partial h_f}{\partial x}\right) + \frac{\partial}{\partial y}\left(K_f\frac{\partial h_f}{\partial y}\right) + \frac{\partial}{\partial z}\left(K_f\frac{\partial h_f}{\partial z}\right) - \frac{\Gamma_w}{\omega_f} \tag{2.5a}$$

$$S_{sm}\frac{\partial h_m}{\partial t} = \frac{\partial}{\partial x}\left(K_m\frac{\partial h_m}{\partial x}\right) + \frac{\partial}{\partial y}\left(K_m\frac{\partial h_m}{\partial y}\right) + \frac{\partial}{\partial z}\left(K_m\frac{\partial h_m}{\partial z}\right) + \frac{\Gamma_w}{1-\omega_f} \tag{2.5b}$$

where   *Subscripts f & m refer* to the fracture and matrix pore systems respectively

h is the total head (L),

K is the hydraulic conductivity (LT^{-1}).

ω_f is the fracture volume fraction

t is time (T)

S_s is the Specific storage (L^{-1}) and

Γ_w is the transfer function – an exchange term describing the transfer of fluid between the two pore systems.

Dual-porosity representations, like their other ECM counterparts can be used to model large-scale flow through well connected fractured systems. Its utility is however limited due to the difficulty associated with obtaining and validating the values of the transfer function. (Warren and Root, 1963) proposed a practical formulation that simplified the solution approach for obtaining the transfer function. Their work which is based on the assumption that the matrix blocks are of simple geometry has formed the basis of dual continuum modelling studies by other authors such as Huyakorn et al. (1983); Karimi-Fard et al. (2006); X. Wang & Ghassemi, (2012) and Wu & Qin, (2009). A schematic of the single and dual continuum model conceptualizations is presented in Figure **2. 6**.
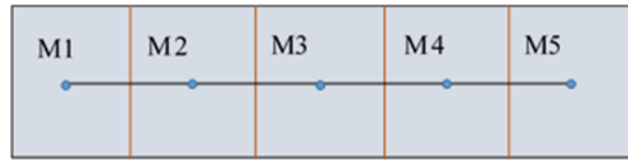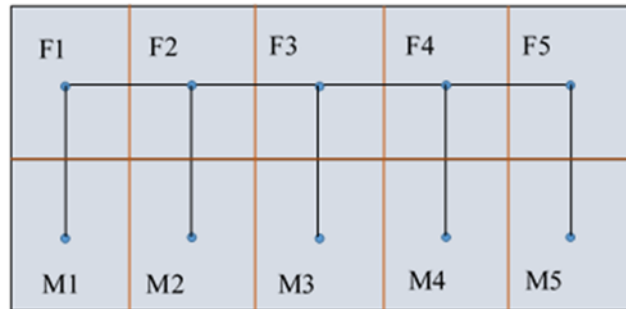
Figure 2.6   Schematic view of equivalent continuum models showing (a) a single porosity continuum formulation and (b) a dual permeability continuum formulation. F and M represents the Fracture continuum and the Matrix continnum respectively.

The advantage of the ECM Model is that it allows for a far-field and macroscopic perspective of the field of interest and thus, detailed knowledge about the individual fractures is not required. While their results have proven useful, they are limited in their ability to predict the effects of concentrated flow paths that arise as a result of discrete fractures as they use an equivalent flow conduit for their modeling. In reality however, flow is restricted to discrete pathways, and networks themselves may be finite.

2.5.2. Discrete Network Models

In the discrete fracture network modeling approach, the fractured reservoir is depicted by a network of discrete features representing fractures, combined with background permeability (La Pointe, 1997). The discrete fracture approach will result in the most physically representative description of the reservoir at the sub-continuum scale. This modeling approach however requires the generation of fracture networks based on working conceptual model developed using information on both the individual fractures and the geometry of inter-fracture relationships. This makes the approach computationally rigorous and unrealistic for field scale modeling purposes. However, the discrete fracture modelling approach has been utilized by authors in characterizing behavior of fractures on a small scale.

For most subsurface hydrogeological studies, the complexity of reality does not always allow for a complete description of the actual field. Therefore the subsurface properties are often simulated using a stochastic model and not a deterministic one because it is difficult to explicitly measure formation properties. A deterministic approach to modeling means the detailed presentation of the physical situation; however it is usually complex and at most times, obtaining and meeting the data requirements is almost impossible, particularly in highly heterogeneous formations. A stochastic approach on the other hand is based on the hypothesis that natural parameters that appear random are in reality not completely spatially and randomly distributed but have a trend and uniformity to a certain degree (Tubeileh, 2003).

The physical model is thus usually based on a complex and stochastic geometry. The main advantage of this model is that it considers the contribution of every fracture towards the overall transmissivity of reservoir and can be applied at any scale. The drawback of this model is that statistical information required for parameter estimation may also be difficult to obtain. This model

34

may become very complex at field scale and computationally intensive (Anwar, 2008). The model generation process involves the study of a fracture population, the choice of the network model i.e. random planes or random discs; and the study of the geometry of the single fracture. To a large extent, fracture size, shape and orientation can be idealized as random variables and statistical distributions can be employed to generate the fracture network. For example, the geological medium might be considered as a cube, and the fractures represented by ellipses with random distributions of eccentricity, length, position and orientation (Chiles et al, 1993; Erhel, 2007).

Wang and Ghassemi (2011) utilized discrete fracture networks to study fracture flow. Their study focuses on utilizing stochastic fracture networks to simulate flow in fractured rock using a finite element numerical model with a stochastic description on fracture distribution alongside assessment the mechanical rock mass response to stress variations caused by injection/production, i.e., the response of the system during periods of active stimulation.

Jacot et al. (2010) also utilized the DFN methodology as a tool in their research study. The aim of their model was to optimize the economics of wellbore production and seek ways to enhance production in the Marcellus shale. Although their simulation results were not unique, the study highlighted the need for a network of connected secondary fractures and the importance of technology integration in obtaining history matched solutions in the simulated formation.

Studies into the applicability of the discrete fracture network models to modeling of field abound in literature (Andersson and Dverstorp, 1987; Sarda et al., 2002; Painter and Cvetkovic, 2005; Karimi-Fard et al., 2006; Parker et al., 2012). In all these studies, the importance of having a knowledge of the connectivity of the discrete fractures as well as the scale restrictions associated with the individual representations of the fractures is emphasized.

2.5.3. Hybrid Models

Hybrid models offer a way of dealing with the scale restrictions associated with the use of DFN simulation models. This approach, which can also be thought about in terms of an upscaling methodology introduces the concept of dividing the field-scale domain into smaller sized domains, and making use of the DFN approach to deduce effective parameters that can be utilized in the solution of a simpler and computationally inexpensive model such as the continuum model for the field-scale model (National Research Council, 1996).

In the generation of hybrid models, it is assumed that the fracture network model used in the DFN simulation, i.e. the fracture distribution in each sub-domain, is representative of the fracture network in the larger domain. The hybrid modeling approach starts out by generating the full 3D DFN, overlaying a continuum grid on the generated fractures and then computing the effective property values in a tensor form (Oda, 1985; Dershowitz et al., 2004).

Parashar et al (2010) developed a fracture continuum approach using MODFLOW for the solution of fluid flow within the fracture network and low-permeability rock matrix, Their approach assumes that fractured continuum model is suitable for capturing the key aspects of flow in their study.

The use of the hybrid approach to shale modeling is supported in literature by several studies (Painter and Cvetkovic, 2005; Wu and Qin, 2009; Dong, 2010; Wang et al., 2013; Ding et al., 2014). The hybrid approach is particularly suited to shale formations as they contain fractures and faults, which exist on multiple scale ranges, and the approach ensures that the essential properties associated with these features are properly captured and represented in the model.

2.6 Summary

Understanding flow in fractured rock remains a challenge, as high transmissivity fractures control flow and transport and we are limited in our ability to predict where they occur and how they connect with other features. The importance of choosing an appropriate conceptual model cannot be overemphasized as it determines the quality of the result that is obtained. If a conceptual model is robust, different mathematical formulations of the model will likely give similar results. Identifying pertinent physical processes, developing a conceptual hydrogeological model, and recognizing appropriate field data requirements are thus critical to a successful modeling endeavor.

The review of literature has shown that complex fracture network are developed in shale formations and that proper characterization of these fractures are essential for accurate reservoir production forecasting (Carter et al., 2000; Fisher et al., 2002). Studies that utilize the knowledge of complex fracture pattern generation as a starting point for the simulation of fluid flow migration patterns in shale formations are however still sparse in literature, with those found utilizing simple fracture arrangements because of the computational intensity associated with representation of the physics associated with the complex fracture pattern (Freeman et al., 2008; Almulhim, 2014; W. Yu et al., 2014).

This work presents the development of a shale gas reservoir model for the characterization of flow behavior in shale formations. This model makes use of hybrid modeling techniques and numerical simulation methods to account for the complexity of secondary network of fractures, and investigates the relationships between the different attributes of the reservoir being studied, as well as the different configurations of fracture network, on the response of the model.

CHAPTER 3

MODELING OF SUB SURFACE CONFIGURATION

3.1. Introduction

The development of predictive models for flow and transport in shale formations is still an active area of research. While reservoir production rates and completion data are becoming available for the validation of deterministic models, the number of reservoir parameters with inherent uncertainties are still sizable enough , that the use of synthetic models i.e. mathematical representations, based on available information forms the basis for most studies.

Completion methods in shale gas formations involve inducing hydraulic fractures into a naturally fractured domain -See **Figure 3.1**. Most models in the literature (Cipolla et al., 2009; Rubin, 2010; Li et al., 2013; Ding et al., 2014) make use of conventional orthogonal transverse fractures as a way to account for natural fractures in the formation. However shale layers have been observed to be made up of mostly horizontal layers of laminated bedrock. It therefore seems that a suitable conceptual model for a shale reservoir should have horizontal fracturing network elements built into the simulation. In this study, a novel approach to modeling shale reservoirs which makes use of a hybrid model which includes semi-explicit representations of horizontal fracture laminations and hydraulic fractures, and upscaled representations of secondary fractures and microfractures.

The sequential approach to the model development process is described in the sections that follow. First, a conceptual model which takes into account the assumptions of the study, the different physical processes taking place in the formation and their governing equations is presented, with discussions of the principles underlying gas desorption as well as the cubic law for flow in fractures. Then, the procedure for the representation of the fracture networks and the

wellbore geometry in the model is addressed. As discussed in the review of literature, fractures can be modeled either as explicit (discrete fractures) or implicit (continuum) features in the domain. In an explicit model, the full geometrical characteristics of the physical feature are included in the model while in the implicit form, certain techniques are required to describe the fracture properties without specifying the fracture geometry. The semi-explicit approach to representing the natural and hydraulic fractures is therefore discussed next.

The next section discusses the representation process for the secondary fractures. These are modeled as implicit features. The procedure to obtaining the properties of the secondary fractures begins with the generation of the fractures as discrete features. This is achieved by implementing a fractal algorithm, which utilizes the locations of well-bore penetrations for the hydraulic fractures as its points of origination. Next, an upscaling procedure is employed because of the complexity of the generated secondary fracture system, and a kriging process to interpolate formation properties at points where such properties are not fully specified is presented.

With the selection of governing equations, representation of model features, and generation of simulation parameters completed, the choice of a simulation code becomes necessary. The next section follows with a brief description of the reservoir simulation software package. Also, a set of initial and boundary conditions are required in order to obtain a solution of the fluid velocities and pressure fields in the model domain. These conditions are presented and discussed. Finally, the chapter ends with a section describing how flux through the wellbore i.e., flow rate out of the formation, is calculated.
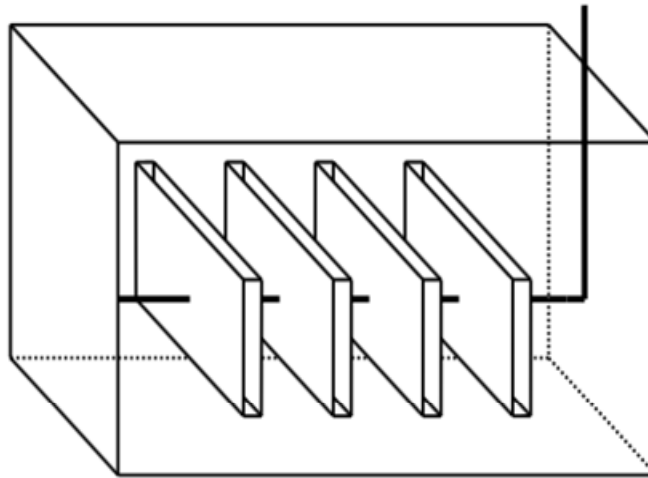
Figure 3.1 Schematic of a typical completion arrangement in shale gas production sites which makes use of transverse fractures in a horizontal well (*Dong*, 2010).

3.2. Conceptual Model of the Reservoir Domain

A conceptual model is set up based on published average reservoir data for a producing shale formation(Yu et al., 2014) and published well completion data (Ramakrishnan et al., 2011; Harpel et al., 2012). For computational tractability the model is sized around one production stage with 2 foot perforated sections located at 80 foot intervals.

The following assumptions are implemented for our studies:

i.   The formation is rectangular and contains natural and induced fractures.

ii. The formation is completed using multiple transverse fractures originating at perforations and intersecting the horizontal well.

iii. Gas in the reservoir flows into the wellbore only through the perforated intervals.

iv. The reservoir formation is dual porosity, but is represented by a single porosity system. Properties of the secondary fractures are upscaled to represent a non-homogeneous anisotropic continuum and flow in the second porosity system-the natural and hydraulic fractures- is accounted for by the specification of internal boundaries.

v. Flow in the reservoir can be described mathematically by Darcy's law.

vi. The effects of desorption are included in the study.

vii. The formation is considered to be impermeable, except in the case where it intersects a pre-existing fault or fracture –in which case a pressure boundary condition is specified.

3.3. Governing Equations for Fluid flow in Shale Formations

Depending on if the formation being studied is a dry-gas reservoir or one with significant water content, a single phase or two-phase flow model is considered as the conceptual flow model for in shale, however, since we are most concerned with the migration pattern of the gas in the formation, we assume that the water in our system is at residual saturation and immobile. This is a situation which is generally prevalent in most shale gas formations. This reduces our model to a single phase flow formulation, with the pressure gradient as the hydraulic potential.

3.3.1. Single Phase flow equations in the Shale Matrix

King (1990) describes the development of material balance equations used in estimating gas content in unconventional gas reservoirs. To account for the adsorbed gas on the solid phase

of the rock, the mass conservation equation for isothermal gas flow is modified to include the physics of adsorption as presented in the equation below.

$$\frac{\partial}{\partial t}(M_s + M_p) = -\nabla \cdot (\rho v)$$

(3.1)

where $\quad$ $\boldsymbol{M_s}$ represents the amount of mass present in the adsorbed state and

$\boldsymbol{M_p}$ is the amount of gas present in the pores in the formation.

Most researchers have been able to validate the use of Darcy- flow equations for bulk phase matrix transport of the gas and we therefore employ these equations for the purpose of our study.

$$v = -\frac{k\rho g}{\mu}\nabla p = K\nabla p$$

(3.2)

First, we seek to account for the adsorbed gas in the rock matrix. Gas adsorption is a surface phenomenon in which the molecules of the gas become bound to the surface of a solid as a result of inter-molecular attractive forces. The converse process in which the gas molecules are released from the surface of the rock is referred to as desorption and is an important element in shale gas production.

Release of gas from shale reservoirs is usually described by an adsorption isotherm (Hardy et al., 2012; Rexer et al., 2013; Wang et al., 2013). The isotherm specifies the amount of gas in equilibrium with the rock surface as a function of pressure at a constant temperature value. The

Langmuir isotherm is the most commonly used model for quantifying gas adsorption and desorption. It gives the dependency of the adsorbed gas volume on the reservoir pressure at any point in time (Leahy-Dios et al., 2011; Wu et al., 2013). The volume of gas that can be adsorbed V_{ads} is estimated by making use of the Langmuir adsorption isotherm function stated as:

$$V_{ads} = \frac{P}{P + P_L} V_L$$

(3.3)

where   **P** is the reservoir pressure

                 P_L is the pressure at which 50% of the gas is desorbed (Langmuir pressure) and V_L

                 is the gas content, (Langmuir volume) specified in scf/ton.

A typical sorption isotherm is illustrated in **Figure 3.2.**
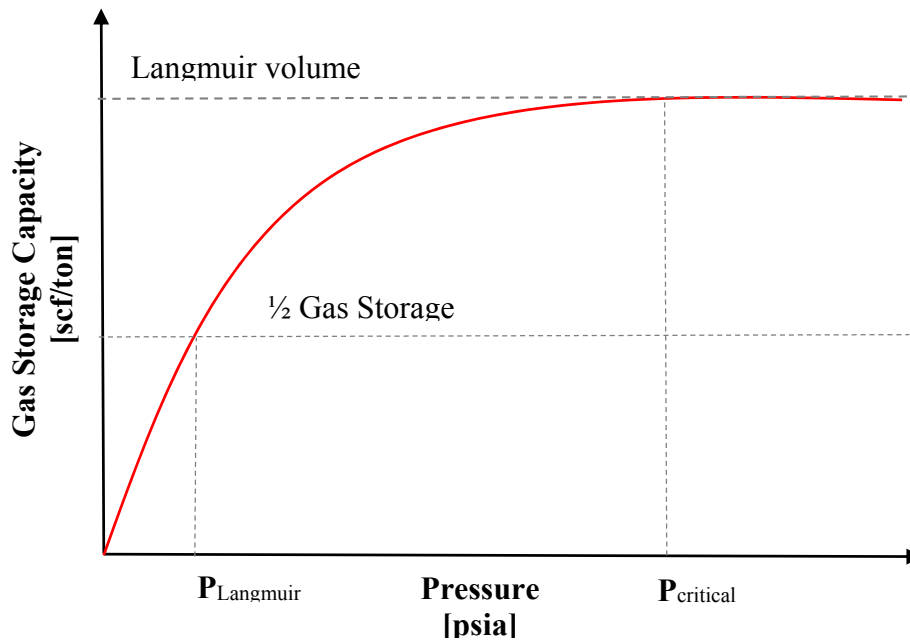
Figure 3.2   Typical Langmuir Sorption Isotherm

The mass of adsorbed gas in the formation from equation (3.1) can thus be expressed by the relationship

$$M_s = \rho_k \rho_g V_{ads}$$

(3.4)

where ρ_k is the bulk density of the rock,

ρ_g is the gas density at standard conditions and

V_{ads} is the estimated adsorbed gas volume.

For the estimations, it is assumed that there is local equilibrium between the free and adsorbed gas phases i.e. a transient lag between pressure change and desorption responses does not exist, and as such, there is an instantaneous re-establishment of equilibrium conditions when the pressure changes.

By substituting for the value of V_{ads}, we can rewrite equation (3.4) as

$$M_s = \rho_k \rho_g \frac{P}{P + P_L} V_L$$

(3.5)

$$\frac{\partial}{\partial t}(M_s) = \frac{\partial}{\partial t}(\rho_k \rho_g \frac{P}{P + P_L} V_L)$$

(3.6)

$$= \rho_k \rho_g \frac{\partial V_{ads}}{\partial P} \frac{\partial P}{\partial t}$$

(3.7)

$$\frac{\partial V_{ads}}{\partial P} = \frac{V_L * P_L}{(P + P_L)^2}$$

(3.8)

Therefore

$$\frac{\partial}{\partial t}(M_s) = \rho_g \frac{V_L * P_L * \rho_k}{(P + P_L)^2} \frac{\partial P}{\partial t}$$

(3.9)

Equation (3.9) describes the rate of change of mass of gas present in the adsorbed state in the matrix. Next, we seek to account for the gas in the pore spaces of the reservoir matrix.

The mass of gas in the reservoir pore volume can be expressed as a function of the porosity of the reservoir and the density of the fluid in the reservoir.

i.e.

$$M_p = \rho \theta$$

(3.10)

where θ is the porosity of the reservoir and

ρ is the gas density at reservoir conditions given as

$$\rho = \frac{M}{RT} \frac{P}{Z(P)}$$

(3.11)

where **M** is the Molecular Mass of the gas,

R is the value of the gas Constant,

Z is the gas pressure compressibility factor and,

T is the temperature of the formation.

The rate of change is thus given by:

$$\frac{\partial}{\partial t}(M_p) = \frac{\partial}{\partial t}(\rho\theta)$$

(3.12)

$$= \theta \frac{\partial \rho}{\partial P} \frac{\partial P}{\partial t}$$

(3.13)

The isothermal compressibility of a gas C_f is defined as $\frac{1}{\rho}\frac{\partial \rho}{\partial P}$ so that

$$\frac{\partial \rho}{\partial P} = \rho C_f$$

(3.14)

And

$$\frac{\partial}{\partial t}(M_p) = \rho\, C_f\, \theta\, \frac{\partial P}{\partial t}$$

(3.15)

Therefore:

$$\frac{\partial}{\partial t}(M_s + M_p) = \rho_g \frac{V_L * P_L * \rho_k}{(P + P_L)^2} \frac{\partial P}{\partial t} + \rho\, C_f\, \theta\, \frac{\partial P}{\partial t}$$

(3.16)

Re-writing equation (3.1) in the expanded form gives

$$\rho\, \frac{\partial P}{\partial t}\left(\frac{V_L * P_L * \rho_k}{(P + P_L)^2} * \frac{\rho_g}{\rho} + C_f\theta\right) = -\nabla.(\rho v)$$

(3.17)

Equation (3.17) specifies the governing equation for fluid flow in the shale matrix.

3.3.2. Single Phase flow equations in Fractures

Fluid flow in a single fracture is often modeled by assuming the fracture walls are analogous to parallel plates separated by a constant aperture (See **Figure 3.3**). Using this analogy, the solution of the Navier–Stokes equations for laminar flow of a viscous, incompressible fluid bounded by two smooth plates, in a direction parallel to the bounding plates, leads to an expression referred to as the cubic law, which is written as:

$$\frac{Q}{\nabla\varphi} = Cb^3$$

(3.18)

where Q is the volumetric flow rate (L^3T^{-1}),

$\nabla\varphi$ is the drop in hydraulic potential (L),

47

b is fracture aperture (L) and

C is a constant related to the properties of the fluid and the geometry of the flow

domain.

A detailed development of the cubic law is presented in Appendix A.
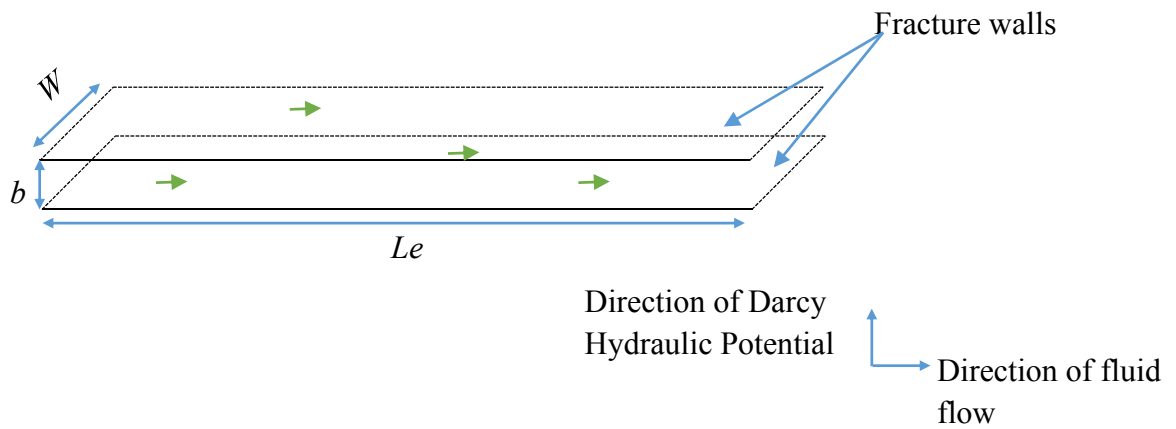
Figure 3.3   Schematic of flow through a fracture hypothesized as parallel plates

For uniform flow in Cartesian grids, the constant C has been found (Lapcevic et al., 1999),
to be given by the term:

$$C = \frac{\rho g}{12\mu} \frac{W}{Le}$$

(3.19)

The transmissivity (T_f) and hydraulic conductivity (K_f) of the fracture can be obtained by substituting the cubic law obtained in equation above into the Darcy equation for fluid flow. This yields the result

$$T_f = \frac{\rho g}{12\mu} b^3 = K_f\, b$$

(3.20)

A value for the permeability of a single fracture can be inferred from equation (3.19), as long as the value of the fracture aperture is known

$$k_f = \frac{b^2}{12}$$

(3.21)

A modified Darcy's law can be written for flow in the fracture with respect to the flow direction and the direction of the Darcy potential drop (see Figure 3.3) as:

$$v_f = K_f(\nabla_T p)$$

(3.22)

Where $\nabla_T p$ represents the tangential pressure gradient between the fracture surfaces.

A single equation in terms of pressure can be obtained for the transient flow of fluid in fractures by combining equation (3.22) with the continuity equation and integrated over the fracture cross section. This equation is given as:

$$\frac{\partial}{\partial t}\left(M_{fp}\right) = -\,\nabla_T \cdot \left(\rho K_f(\nabla_T p)\right)$$

(3.23)

Where M_{fp} is the mass of the fluid present in the fracture, and specified by

$$M_{fp} = \rho\theta_f$$

<div align="right">(3.24)</div>

θ_f is the porosity of the fracture

ρ is the gas density earlier defined.

and all other parameters are as earlier defined.

Equation (3.23) is analogous to the mass balance equation in equation (3.1) and can be rewritten in a simplified form as:

$$\frac{\partial}{\partial t}(M_{fp}) = \nabla_T.(\rho v_f)$$

<div align="right">(3.25)</div>

specifying the governing equation for fluid flow in fractures.

In reality however, fluid flow in fractures takes place in fracture networks, and the complex arrangement of fractures frequently encountered in reservoir formations often lead to difficulties in numerical modeling of these features.

3.4. Wellbore Geometry and Parameter Representation

It is important that the conditions at the wellbore be well defined as different flow behaviors can result depending on the completion model utilized for the wellbore study. Wells in shale formations are usually completed using a cased perforation completion approach – See **Figure 3.4**. The perforations serve as the pathway for the initiation of hydraulic fractures into the formation and also as the only point through which produced gas can exit the domain. The parameters for defining the wellbore recovery are defined by the perforation shot density and the perforation phasing respectively. The perforation shot density specifies the number of perforations per foot section of the well casing, while the phasing is the angle between the two consecutive perforations. (Harpel et al., 2012) reported the use of a multi-stage approach to completion operations carried out in the Fayetteville shale. Each production stage consists of $6 - 10$ perforation clusters (2 foot perforated sections) located at intervals of 80ft along the wellbore. The clusters are created by making use of a perforation shot density of 3 shots/ft and a perforation phasing of 60^0 (**Figure 3.5**).

Well diameter values reported in literature are between 0.2ft to 0.3ft. Having a wellbore with an outer diameter of 0.25ft in a domain that is hundreds of feet in size, introduces an added layer of complexity into the system to be implemented in the model domain. To address this issue, the wellbore pressure presumed to act only across the perforations i.e. along certain lengths of the fracture intersection at the boundary. Also, the studied domain is assumed to be symmetrical around the wellbore, and around each fracture stage in order to reduce the computational domain. The simulated geometry is as shown in **Figure 3.6**.
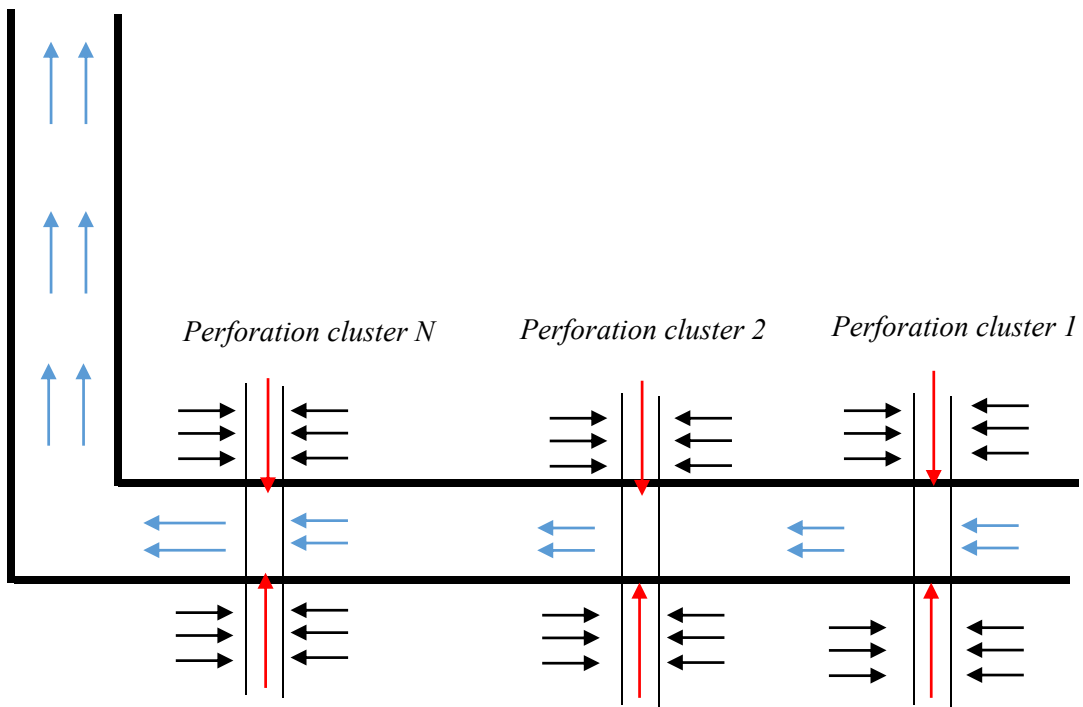
Figure 3.4   A cased perforation completion arrangement in a multi-stage fractured formation highlighting flow in the perforated cluster network, flow to the fractured cluster and flow through the wellbore
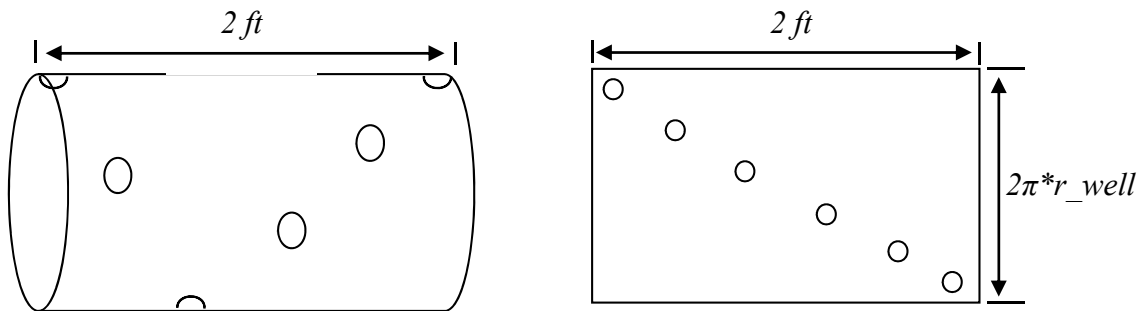
Figure 3.5   Horizontal wellbore section showing spiral perforation pattern using a 60^0 phasing angle and a shot density of 3 shots/ft over a 2 feet pipe section of radius r _well.

(a)

(b)
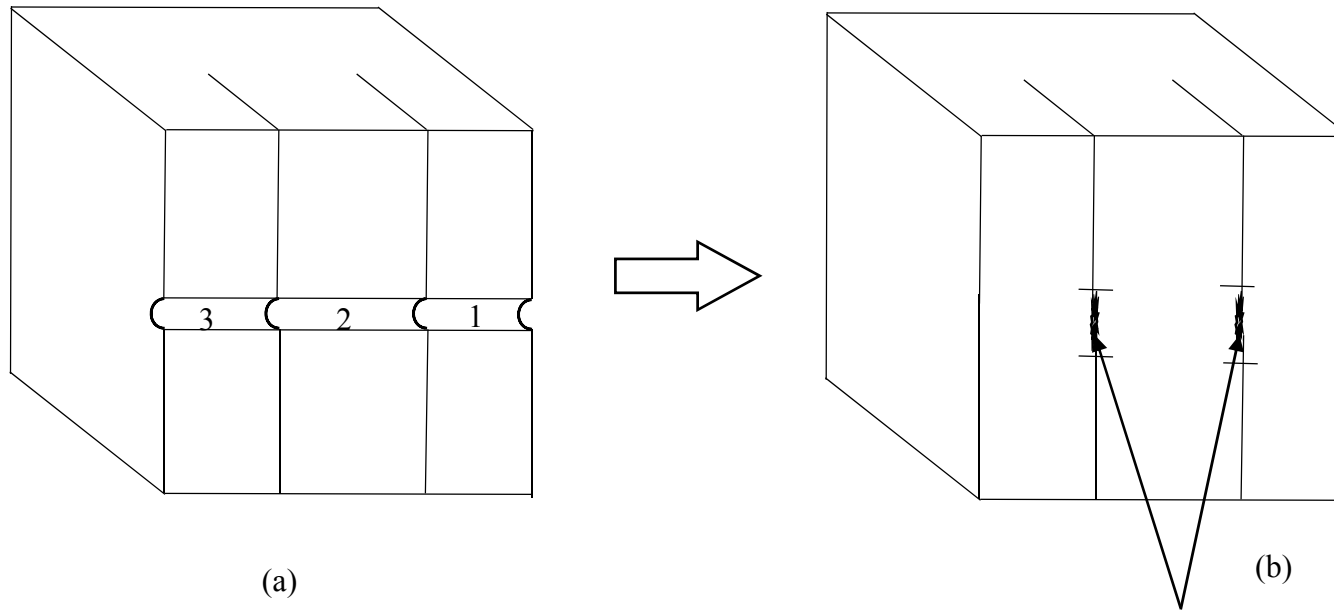
*Sections that represent physics
of interest for simulation
purposes i.e. well-bore section
through which gas is recovered.*

Figure 3.6   Conceptualization of boundary conditions along the horizontal wellbore.

As shown above, sections 1, 2 and 3 in Figure 3.6a represent well-bore boundaries that do not allow for gas escape from the formation. By reformulating the model as shown in Figure 3.6b, the wellbore pressure presumed to act only across the perforations thereby reducing the geometric complexity associated with simulating the entire well-bore.

3.5. Natural Fracture Network Representation

In the generation of synthetic (mathematical) models which represent naturally fractured formations, the parameters that are required to completely specify the characteristics of the natural fracture network are:

i.   the location of the fractures

ii.   the extent of the fractures

iii. the orientation of the fractures and

iv.   the conductive properties of the fractures.

These parameters serve as the essential controls on the topology of the fracture network generated.

Generation of natural fracture networks in literature is based on the premise that natural fractures are stochastic in nature and must be modeled as such. An example of such model is the Baecher model, which assumes that each fracture is elliptical, and is defined by its centroid location, diameter and orientation (Dershowitz and Einstein, 1988; Chiles and de Marsily, 1993). The coordinates of fracture centers are generated using a random number generator following Poisson's distribution. The Poisson's parameter λ represents the expectation of fracture quantity in the selected formation. This parameter is calculated by multiplying the observed fracture density by the length of the model cube. For example, if the fracture density detected from field data is specified as 2 fractures per cubic meter, and the model size is specified as $250 \times 1000 \times 100$ cubic meters, the Poisson's parameter would be calculated as $2 \times (250 \times 1000 \times 100)$ and equals to 50,000,000. This means that a total of 50 million fractures are expected to be located in the model scenario specified above.

The diameters of the ellipses are assumed to be independent of each other and follow a log-normal distribution (Wang and Ghassemi, 2011). To determine the fracture orientation for these studies, the Fisher von Mises parameter k is obtained by conducting statistic study of field gathered fracture orientation data. The cumulative distribution function of the Fisher von Mises distribution is generated as discrete random numbers U first and then these random numbers are then transferred into random angles by applying the inverse of the cumulative distribution function.

However, the definition of shale suggests that the formation is made up of thin laminar layers that is bound up by immense pressure at depth. The assumption can thus be made that the dominant natural fractures in shale may be described by sheeting fractures, or horizontal plate sections that can be opened by hydraulic fracturing. This conceptual model provides a large porosity that may or may not be connected prior to the hydraulic fracturing. They are however opened during the hydraulic fracturing process leading to a substantial increase in the formation's overall permeability.

For modeling purposes, the natural fractures in the formation are represented in a semi-explicit form. The term semi-explicit is used to denote the reduced dimensionality approach utilized for this process. The fracture volumes are not fully reproduced in the model, rather the fractures are represented by horizontal planar layers with variations in the size, location and orientation of the layers. In this approach, a 3D fracture is modeled as a 2D planar geometry– (See **Figure 3.7**) and the collapsed dimension is accounted for by introducing it into the modified Darcy's law equation which utilizes tangential gradients as earlier discussed.

The effects that different configurations of these natural fractures have on the production rate of gas in the formation is investigated and presented in the next chapter.
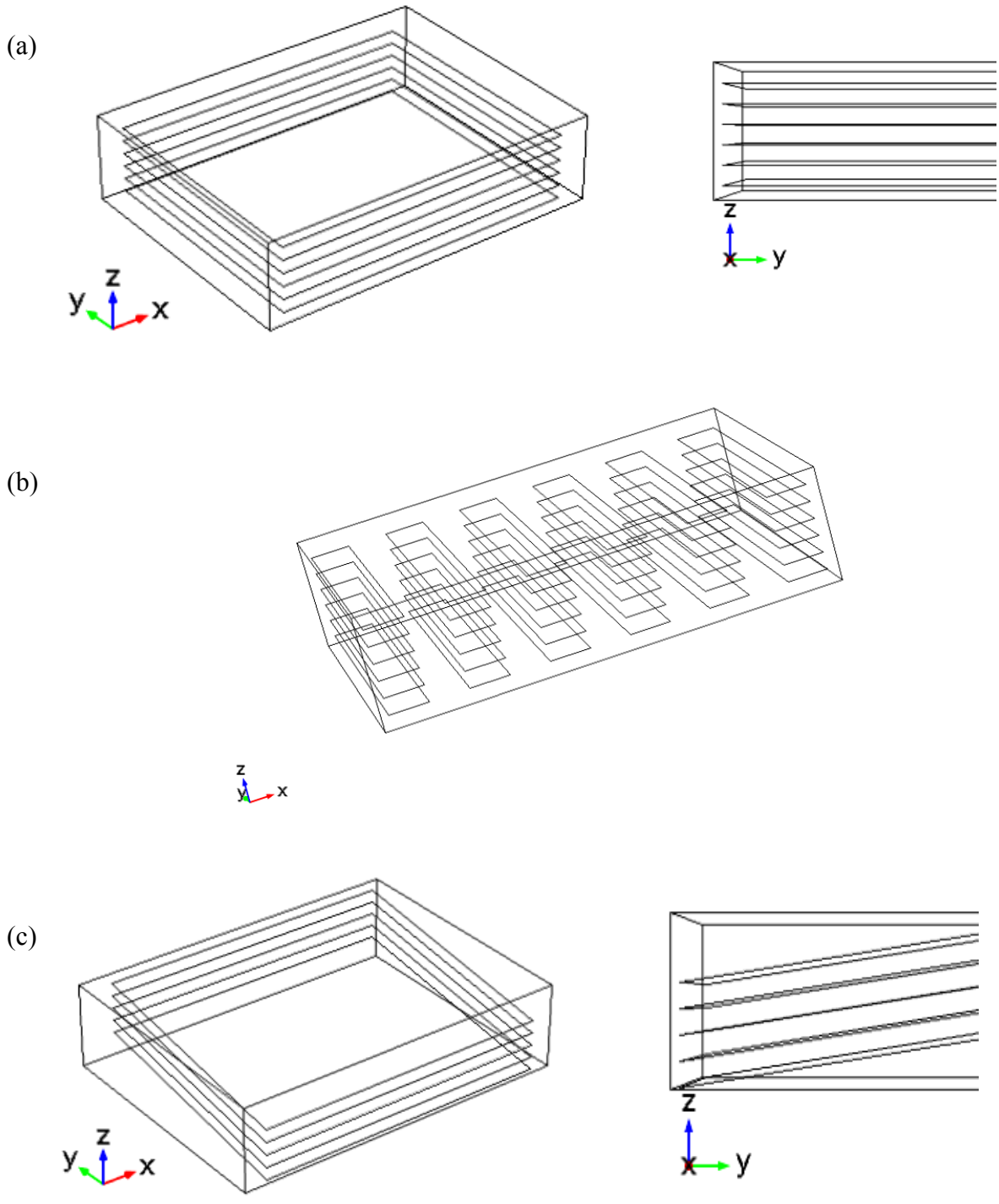
Figure 3.7   Multiple scenarios representing different configurations of natural fractures in the reservoir domain. (a) Natural fracture layers parallel to the horizontal axis (b) layers are separated by sections where facture sheets do not connect (c) natural fracture layers inclined at an angle to the horizontal

3.6.   Induced Fracture Representations

The tendency for induced hydraulic fracture to form asymmetrical patterns as they interact with natural fractures in the formation has been discussed in literature (Bennet et al., 2005; Dershowitz and Doe, 2011). According to Mohaghegh (2013), the coupling of hydraulic fractures and natural fracture networks, and their integration and interaction with the shale matrix still poses a significant challenge to the reservoir modelling of shale formations. This is a problem of significant interest to shale gas operators, regulators and the members of the communities who are interested in fully understanding the effects of hydraulic fracturing.

Monitoring activities carried out in shale exploration areas utilizing micro seismic studies have suggested that the fracture network generated differs from the bi-wing fracture model commonly used in literature, but appear to be more like a network of distributed fissures along a central line or a fractal (Urbancic et al., 2010). Fractal geometry has been reported to be a powerful tool for describing patterns in nature. The fractal pattern is one in which self-similarity is present between all its sub-parts. This characteristic of a fractal geometry makes it amenable for use in generating synthetic fracture networks whose size and spatial properties are constrained by the fractal dimension.

In this work, I have adopted the use of secondary fractures as a way of describing the asymmetrical distribution of fractures that arise as a result of the hydraulic fracturing process. For the purpose of this study, the hydraulic fracture itself is represented as a semi-explicit feature just like the natural fracture system. The post-fractured state of the formation which represents the stimulated reservoir volume/secondary fractures is however represented by the use of asymmetrical fractal patterns. This geometry is assumed to be a tree patterned network extending from the perforation at the wellbore. This approach has not been presented so far in literature, but

57

the study by Urbancic et al. (2010) supports these assumptions. The fractal pattern is approximated by the use of a modification of the Pythagoras tree. The Pythagoras tree is a plane fractal that is constructed from recursively generated squares that are fractional multiples of the original square and grows according to the specified number of iterations. For our use, an adaptation of the Pythagoras tree that makes use of lines instead of squares and allows for recursive generation of daughter branches with different orientations is employed. The study of the irregular fracture patterns generated, can provide useful insight into the effects of these non-ideal fracture geometries on the flow behavior.

Fractal Generation Algorithm

An assumption is made about the origination point of the hydraulic fractures. They are assumed to originate from the perforation sections present on the cased wellbore. The perforation points therefore serve as the location of the initiating fractal pattern. By utilizing the concept of self-similarity of fractals, the procedure for generating the network of secondary fractures from the initial fracture location and property is presented below:

Step 1:   Define the parameters specifying the first line

   Fracture location, Fracture length

Step 2:   Specify the number of daughter lines to generate at each iteration

   Number of branches

Step 3:   Specify the angle of orientation of daughter lines

   Inclination angles – ϕ and θ

Step 4:   Specify the number of times to generate daughter lines

Number of iterations

Step 5:   Generate daughter lines

Draw the initial line

At the end of the line, apply rotational and scaling transformations on line

Append generated line(s) to original line

Step 6:   Repeat step 5 for number of iterations

Step 7:   Plot generated line segments

A sample of the generated fractal geometry is presented in Figure 3.5. The output of this algorithm is a group of variables specifying the spatial coordinates of the starting and end points of each branch of the fracture network. A complete MATLAB implementation of the pseudo code specified above and implemented in our modeling is presented in Appendix B.
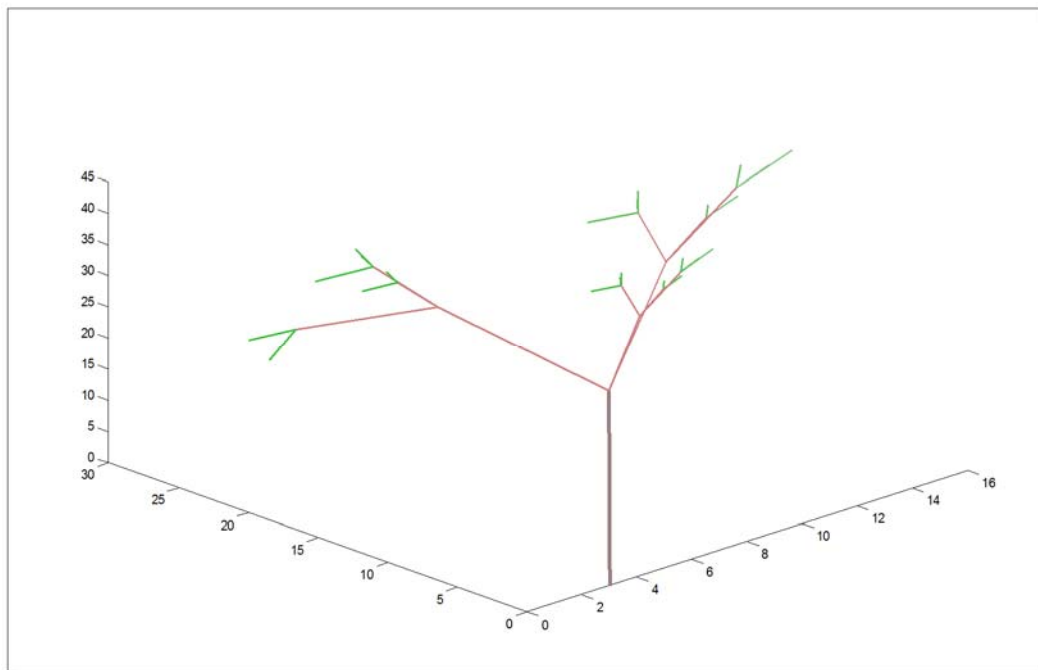
Figure 3.8   Sample fractal configuration generated using MATLAB.

59

3.7.   Geometric Upscaling of Fracture Properties

In situations where multiple and complex fractures exist over a large scale formation or in areas containing fractures with high length to width ratios e.g. secondary fractures generated in the previous section, the representation of individual fractures possessing low aspect ratios becomes computationally implausible. The continuum approach of obtaining an effective property value that is representative of the geology and preserves the geometrical controls of the parameters therefore presents the most effective mode of capturing the physics of the formation. To be able to represent the properties of the generated model of the formation as a non-homogenous anisotropic continuum however, a careful subdivision of the model volume into representative volume or grid sections over which the formation properties are reasonably conserved after an averaging process has taken place.

In the subsections that follow, the technique for upscaling the formation properties, - which involves a subdivision of the formation into subdomains, accounting of fracture features that are present in the individual subdomains by means of a clipping algorithm, the subsequent calculation of effective property values by an averaging approach, and the interpolation procedure for obtaining formation properties in the presence of uncertainty, is discussed.

3.7.1.   Subdomain Grid Discretization

Controls on the size of the subdomains to be used for the model simulation are based on the spacing between perforated sections, along the axis of the wellbore, with the grid allowing for 2 subdivisions between two perforated sections. The subdomain grids (It should be noted that these

differ from grids generated in the numerical solvers) are further subdivided logarithmically along the wellbore axis to allow for accurate representation of fracture segments. This subdivision is based on the assumption that all fractal segments originate from the perforations and therefore the largest formation heterogeneity is found in the formation volumes around the perforations. In **Figure 3.9**, a schematic of the subdivisions utilized is presented. A study of the effect of the number of subdivisions on generated permeability is studied and presented in our modeling results.
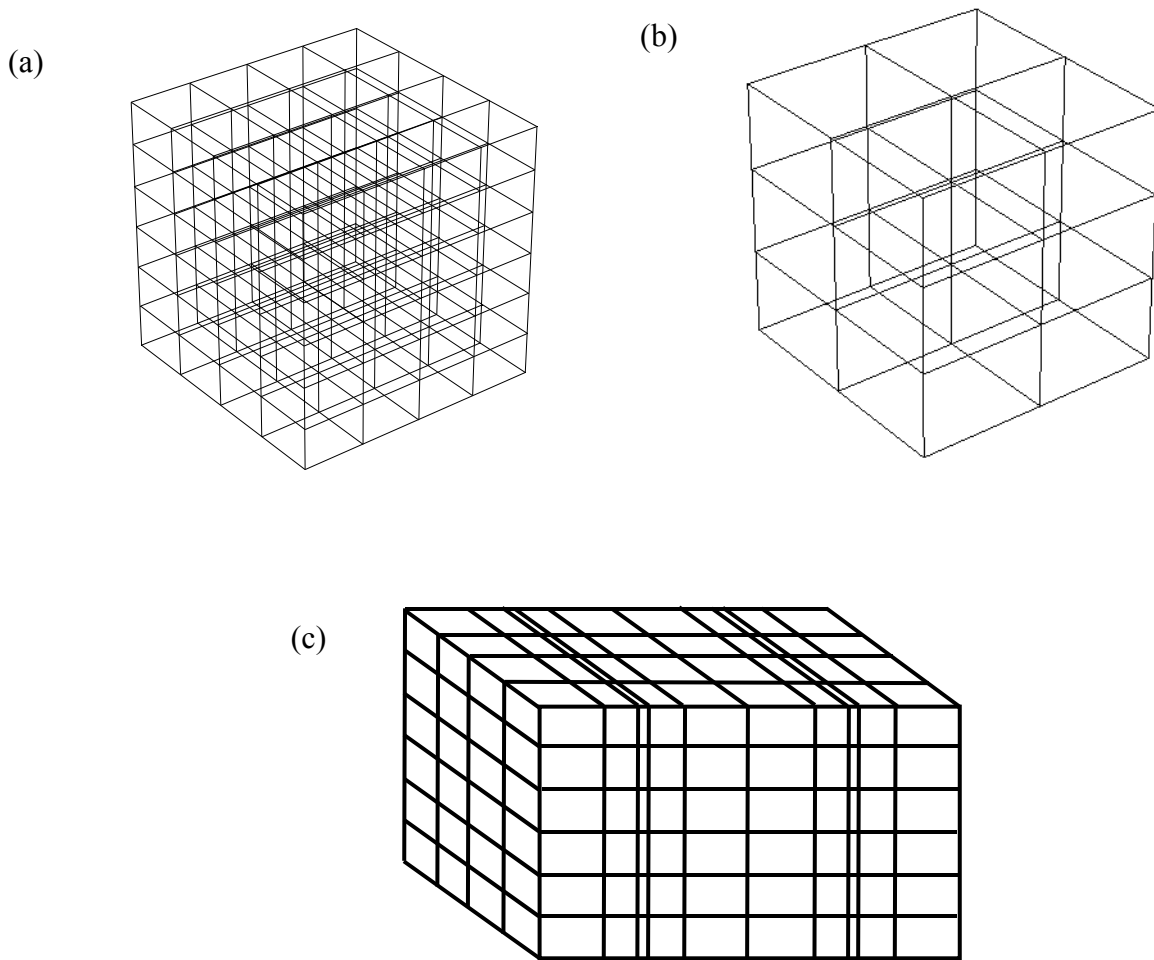
Figure 3.9   Subdomain grid discretization scenarios implemented in study model (a) Box representing formation with 12 subdomains (b) formation with 96 subdomains (c) Subdomain division structure showing logarithmic division along wellbore axis and even gridding structure in y and z-axes

The effective permeability of the fractured reservoir subdomain being studied has to take into account the initial permeability of the formation and the permeability of any fracture included in the subdomain. This effective value k_e can be computed from the equation:

$$k_e = \frac{vol_f}{vol} k_f + \frac{1 - vol_f}{vol} k_m$$

(3.26)

where vol is the volume occupied by the entire sub-region of interest.

And f and m represent the fracture and matrix sub-regions respectively.

3.7.2. Clipping of Fracture Segments

For upscaling purposes, the different segments of the generated hydraulic fracture network needs to be identified and associated with the appropriate subdomain. Carrying out this task requires the use of a clipping algorithm which takes as its input structure the co-ordinates of the generated fractures and outputs the co-ordinates of the fragments that are contained in each subdomain.

To perform a clipping operation involving objects in 3-D space, extraction of a portion of the geometry object being clipped by means of a volume, is carried out. A typical 3-D clipping algorithm involves three steps:

i.   Check to see if the line segment lies completely within the clipping volume

ii.   If not, check if line lies completely outside clipping volume

iii.   If not, compute intersection points with clipping planes and retain information for segment that lies within clipping volume.

Notable algorithms that implement this procedure include the Cohen-Sutherland line clipping algorithm and the Liang-Barsky line clipping algorithm (Liang and Barsky, 1984; Foley et al., 1990; Pandey and Jain, 2013). The Cohen-Sutherland algorithm becomes inefficient for complex problems as it requires that 27 exclusive volumes be defined and different memory allocations be made for each volume in order to determine the interactions of the line with the complete 3D space.

This modeling work makes use of a more efficient clipping algorithm proposed by Kodituwakku et al. (2012). Their algorithm, which employs the use of a series of constants generated from an algebraic manipulation of the equation of a line, reduces the memory allocation and number of calculations required to generate the co-ordinates of a clipped line segment. The algorithm is presented below. A full mathematical derivation of the algorithm is presented in Appendix B.

Clipping Algorithm

Step 1:   Determine the number of lines to be processed by the clipping algorithm.

Number of lines = nl

Step 2:   Specify the extents of the bounding box i.e. define the subdomain coordinates

Lower boundaries (Xmin, Ymin, Zmin); Upper boundaries (Xmax, Ymax, Zmax)

Step 3:   Specify co-ordinates of end points of each of the **_n_** fracture line segments

Lower boundaries (X_1, Y_1, Z_1); Upper boundaries(X_2, Y_2, Z_2)

Step 4:   Starting with one line, compute the values of constants required for obtaining intersection of line with planes using the line equation.

Step 5:   For each end point of the line (X_i, Y_i, Z_i), where $i = 1$ and 2, calculate the intersection point with the 6 planes of the bounding box

Step 6:   Save the co-ordinates for the newly calculated end points of line segments

Step 7:   Repeat steps 4 to 6 for the number of line segments specified in Step 1.

Step 8:   Repeat steps 1 to 7 for the number of subdomains in the domain.

The result obtained from implementing this algorithm is a data-structure containing the co-ordinates of the bounding points of each subdomain and the co-ordinates of the fracture segments associated with each subdomain. Values from this data structure form the basis for the calculation of a permeability tensor (described below), a parameter required in the solution of the governing equations when utilizing an implicit/continuum approach for representing fracture properties i.e. upscaling the discrete fracture properties to a continuum grid.

3.7.3. Calculation of Fracture Permeability Tensor

Permeability in shale formations is often anisotropic, and oftentimes horizontal permeability is higher than vertical permeability as a result of the arrangement of the grain structures in the different directions. The value for the fracture permeability k_f obtained from the equation (3.21) is the permeability value obtained along the direction of the fluid flow and cannot be used directly for the flow solution as it doesn't adequately describe the anisotropic nature of permeability. There is therefore the need to translate k_f into a tensor that can also be referred to as the upscaled fracture permeability k_{ups} which captures the values of the permeability with respect to the new subdomain co-ordinates. In the equations that follow, a mathematical development of the permeability tensor is presented.

Consider the 2D planar fracture depicted by **Figure 3.10**
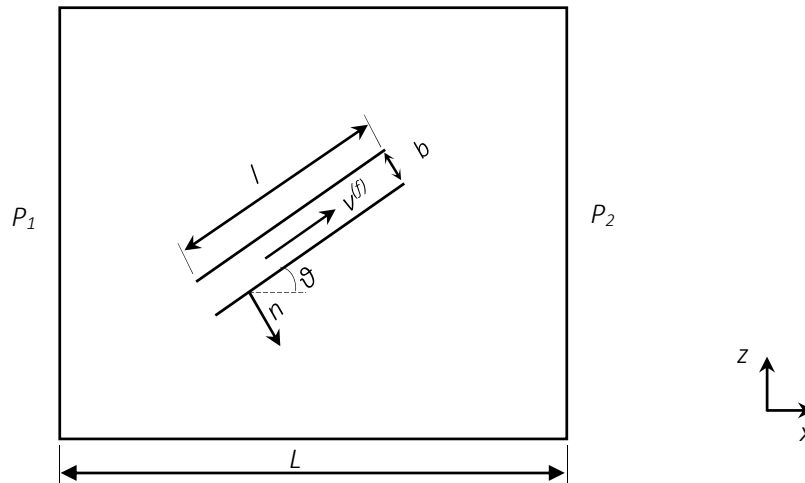
Figure 3.10   Schematic of a planar fracture in a 2-dimensional domain

The hydraulic gradient responsible for flow in this domain is given by

$$J = \frac{P_1 - P_2}{L}$$

      in the x-direction.   (3.27)

This term $'J'$ is referred to as the field gradient (Snow, 1969)

To determine the flow along the fracture however, the tangential component of the field vector along the fracture ($\nabla_T p$) can be related to the field gradient. For ease of solution development, this term is denoted as $J^{(f)}$ and its relationship to J is specified by

$$J^{(f)} = J - (n \cdot J)n$$

                                              (3.28)

$$J_i{}^{(f)} = (\partial_{ij} - n_i n_j)J$$

                                              (3.29)

where ∂_{ij} is the kronecker delta

        i.e. $\partial_{ij} = \begin{cases} 0 & if\ i \neq j \\ 1 & if\ i = j \end{cases}$

                                                (3.30)

and n_i and J_i are components of the normal vector **n** and the **J** projected to the orthogonal axes.

The flow in a fracture has been characterized by idealizing it as laminar flow between parallel plates with an aperture **b**, the velocity of which can be obtained from the cubic law as:

$$v_i^{(f)} = -\frac{\rho}{12}\frac{g}{\mu}b^2 J_i^{(f)}$$

(3.31)

Substituting for $J_i^{(f)}$

$$v_i^{(f)} = -\frac{\rho}{12}\frac{g}{\mu}b^2\left(\partial_{ij} - n_i n_j\right)J$$

(3.32)

The average velocity in the 2D domain is obtained by integration

$$\bar{v}_i^{(f)} = \frac{1}{vol}\int_{V^{(f)}} v_i^{(f)}\, dV^{(f)}$$

(3.33)

$dV^{(f)}$ = volume of a fracture

vol = volume of the domain

Therefore in a scenario with more than one fracture, the total volume of fractures is given as

$$\overline{dV}^{(f)} = \sum_{k=1}^{N} dV_k^{(f)}$$

(3.34)

$$\bar{v}_i = \frac{1}{vol}\sum_{k=1}^{N} v_{i_k}^{(f)}\, dV_k^{(f)}$$

(3.35)

67

Substituting for $v_i{}^{(f)}$ from equation (3.32) in equation (3.35) gives

$$\overline{v}_i = -\frac{1}{vol} \sum_{k=1}^{N} \frac{\rho}{12} \frac{g}{\mu} b_k^2 (\partial_{ij} - n_i n_j) J \, dV_k^{(f)}$$

(3.36)

If the velocity value from equation (3.36) is compared to Darcy's law for flow in the domain- which is given in equation (3.37) below,

$$\overline{v}_i = -\frac{\rho g}{\mu} k_{ij} J_i$$

(3.37)

we obtain the a term for the permeability of the fracture k_{ij}. This term is presented below.

$$k_{ij}{}^{(f)} = \frac{1}{12.vol} \sum_{k=1}^{N} b_k^2 (\partial_{ij} - n_i n_j). \, dV_k^{(f)}$$

(3.38)

Oda, in (1985) developed an approach for the calculation of continuum properties from discrete fractures. The approach which was based on the assumption that continuum properties could be generated directly from the fracture geometry led to the concept of an empirical fracture permeability tensor P_{ij}, the value of which can be calculated by adding the permeabilities of the individual fracture weighted by their volume. This tensor is specified by the equation:

68

$$P_{ij} = \frac{1}{vol}\sum_{k=1}^{N} b_k^2 . n_i n_j . dV_k^{(f)}$$

(3.39)

so that

$$k_{i_j}{}^{(f)} = \frac{1}{12}\left(P_{kk}\partial_{ij} - P_{ij}\right)$$

(3.40)

where P_{kk} is the sum of the diagonal elements.

Equation 3.38 and 3.39 although derived using a 2-D example, can be shown to be applicable even in a 3D reservoir domain with an angle θ to the horizontal and displaced by an angle ϕ in the x-y plane, as shown in **Figure 3.11**.
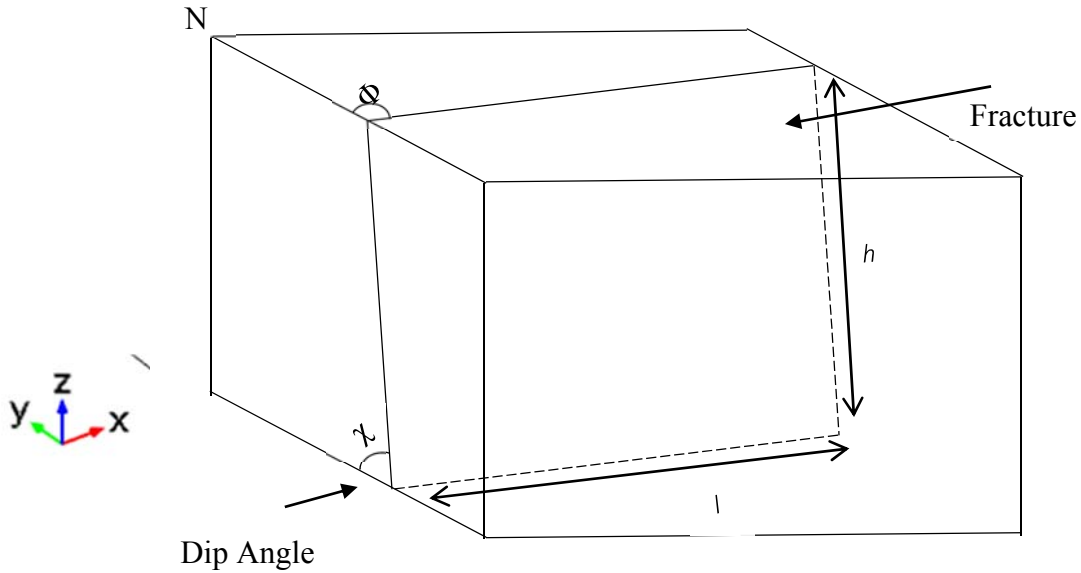
Figure 3.11   Schematic of a planar fracture in a 3-dimensional domain

69

To obtain the permeability tensor for the shown fracture of volume lbh, the values of the components of the normal vector n_i, n_j and n_k , also known as the direction cosines, are developed for the 3D scenario. These values are:

$$n_i = \sin \chi \cos \emptyset$$

$$n_j = \sin \chi \sin \emptyset$$

$$n_k = \cos \chi$$

Thus:

$$n_{11} = \sin^2 \chi \cos^2 \emptyset \; ; \qquad n_{12} = \sin^2 \chi \sin\emptyset \cos\emptyset \; ; \qquad n_{13} = \sin\chi \cos\theta \cos\emptyset$$

$$n_{21} = \sin^2 \chi \sin \emptyset \cos\emptyset \; ; \qquad n_{22} = \sin^2 \chi \sin^2 \emptyset \; ; \qquad n_{23} = \sin\chi \sin\emptyset \cos\emptyset$$

$$n_{31} = \sin\chi \cos\theta \cos\emptyset \; ; \qquad n_{32} = \sin\chi \sin\emptyset \cos\emptyset \; ; \qquad n_{33} = \cos^2\chi$$

For the case of an horizontal fracture with aperture $b = 1$, i.e. χ and $\emptyset = 0$

$$n_{11} = 0 \; ; \qquad n_{12} = 0 ; \qquad n_{13} = 0$$

$$n_{21} = 0 \; ; \qquad n_{22} = 0 ; \qquad n_{23} = 0$$

$$n_{31} = 0 \; ; \qquad n_{32} = 0 ; \qquad n_{33} = 1$$

Substituting for term in equation (3.40),

$$P_{ij} = \frac{1}{vol} \begin{bmatrix} 0 & 0 & 0 \\ 0 & 0 & 0 \\ 0 & 0 & 1 \end{bmatrix} . lbh$$

therefore $\qquad P_{kk} = lbh/vol;$ $\qquad$ and

$$k_{ups}{}^{(f)} = k_{ij}{}^{(f)} = \frac{lbh}{vol} \begin{bmatrix} 1 & 0 & 0 \\ 0 & 0 & 0 \\ 0 & 0 & 0 \end{bmatrix}$$

This value specifies the upscaled fracture permeability, and lies along the horizontal axis.

The effective upscaled permeability value in the subdomain is then reformulated from equation (3.26) with substitutions made for the fracture permeability

$$\boldsymbol{k_{ups}} = \frac{vol_f}{vol} \boldsymbol{k_{ups}}^{(f)} + \frac{1 - vol_f}{vol} \boldsymbol{k_m}$$

$$(3.41)$$

3.7.4. Kriging of Permeability values

The result of upscaling is a series of subdomains that fill the computational domain each with a distinct permeability tensor. There will therefore be discontinuities in the tensor values at the boundary of these subdomains. This section describes the approach taken to smooth the tensor field over the computational domain of the finite element calculations. In numerical computation using grid systems, the values of the domain property is assigned either as a face-centered value or a block centered value. For this work, the value of the calculated effective permeability values is assigned to sections of the domain using the block centered approach, and the geostatistical interpolation technique of kriging is then used to interpolate for the data values at points in the formation where the data values are not explicitly calculated. The advantage of the kriging

technique over any other deterministic interpolation scheme is that it yields a best estimate of the value at the unknown locations based on a least square fit.

The kriging technique assumes that the first statistical moment of the property being considered is inhomogeneous, such that $\bar{k} = \bar{k}(x)$ and that the second moment is homogenous, i.e. the covariance is not a function of the spatial co-ordinate but of the distance r between the two points - $Cov = Cov(r)$. The estimation of the property value k at the unknown point can then be obtained using correlations utilizing a semivariogram and by solving the equation:

$$k^*(x) = \bar{k}(x) + \sum_{i=1}^{n(x)} \lambda_i(x)[k(x_i) - \bar{k}(x_i)]$$

(3.41)

where x_i is the sampled point ;

the asterisk * subscript indicates an estimated value;

$\bar{k}(x)$ refers to the mean of the property value in the subdomain and the weights λ_i, need to be determined and may be selected differently at different locations within the subdomain.

The choice of weights λ_i is dependent on the degree of statistical homogeneity that can be attached to the studied field. In this study, the permeability values can be formulated as a function of space i.e. values within a certain radius to each other are strongly correlated than values that are present at farther distances. The effect of three different weight expressions- which are functions of distance - on the permeability of the modeled domain is conducted and the expression that closely matched values obtained in a validation study is then adopted. The estimated values are

obtained using a 3ft grid discretization. The mathematical algorithm implemented to generate the

kriged data values is presented in Appendix C.

3.8.   Reservoir Simulation Code

Mathematical models usually possess the greatest potential to provide the much needed

information about otherwise recondite relationships present in nature. These models can either be

analytical or numerical. Numerical models have an advantage over analytical models in terms of

the range of problems that they can adequately represent. Over time, differential and integral

numerical methods for solving the material balance equations describing mass flow and transport

in fractured porous media have been employed. For the spatial derivatives, integral methods have

enjoyed more widespread use than the differential approach of the finite difference method, partly

because they are amenable to irregular domain geometries. Integral methods used in fracture flow

modeling include the finite-element method and the boundary-element method (Diodato, 1994).

The finite element method (FEM) is based on the idea that by dividing a domain into

smaller subsections or finite elements, and solving a simpler form of the governing physical

equations on the smaller domain, an approximation of the solution to the entire domain can be

obtained using a piece-wise continuous function. This method has developed into an important

tool for the simulation of subsurface systems. Perhaps, its most attractive feature is its ability to

handle complex geometries and boundaries with relative ease even in three-dimensions (Le Roux

et al., 1998; Franca and Hwang, 2002). The formation is modeled using the subsurface flow

module of COMSOL Multiphysics 4.4 – a finite element software package, which in addition to

73

its capabilities to handle coupled physics problems, also offers a graphic user interface (GUI) for the visualization of simulation results.

The flow in the domain was specified using the Darcy's law module of COMSOL which utilizes equation (3.17) as described in the governing equation section. Flow through the hydraulic and natural fractures (laminated planar layers) is modeled by the assignment of upscaled property values generated from the MATLAB fractal generation code in combination with COMSOL's semi-explicit fracture flow boundary condition. The fracture flow delivers the capability of generating the fracture as a boundary within the modeled geometry which eliminates the need for extensive and excessive meshing requirements of having a different domain and leads to a faster and improved solution of the physics.

The interface uses the tangential version of Darcy's law. It increases the computational efficiency of the simulation as it makes use of a reduced dimensionality for the fracture domain, i.e. a 3D fully explicit fracture is modeled as a 2D planar geometry. The collapsed dimension is accounted for in a re-formulated equation for flow which makes use of tangential derivatives to the pressure gradient to solve for pressure distribution within the fracture.

$$q_f = -\frac{k_f}{\mu} d_f (\nabla_T p)$$

(3.42)

where q_f is the volume flow rate per unit length in the fracture, k_f is the fracture's permeability, μ is the fluid dynamic viscosity, d_f is the thickness of the fracture, ∇_T denotes the gradient operator restricted to the fracture's tangential plane and p is the pressure.

3.9. Initial and Boundary Condition Specification

A set of initial and boundary conditions is required to solve a transient simulation i.e. a complete set of variables over which the solution of the equation in each grid block is carried out.

3.9.1. Initial Conditions

An initial condition of constant pressure is specified everywhere in the numerical domain for time $t = 0$. The free time stepping algorithm is specified in the solver with an initial time step of 0.0001 days in order to resolve the strong transients that might be introduced into the system as a result of the jump in boundary condition at the wellbore relative to the initial pressure of the reservoir domain and to address the issue of non-converging time steps.

3.9.2. Boundary condition – External reservoir boundaries

A no flow condition is specified at the top and bottom of the formation for purposes of model validation. In cases where the effect of an overlying domain is to be studied, the boundary of the shale formation in contact with that boundary is modeled by assuming continuity of flow between the two layers. Symmetry boundary conditions are specified along the other faces of the domain being modeled.

3.9.3. Boundary condition - Wellbore

The boundary condition specified at the wellbore is that of constant pressure. The area of the perforated section of the wellbore exposed to the reservoir is also specified.

3.9.4. Boundary condition – Fault intersections

A pressure boundary condition is specified at the boundary sections representing the intersection of a fault with external boundary. The specified pressure at the boundary is obtained from transient pressure distribution results of a simulation study utilizing no-flow boundary conditions along the overlying boundary face. The results obtained along the fault section is then sent in as the boundary condition for a new simulation study.

3.10. Flux Estimation

The flux of gas through the system presents a way by which the model can be validated for accuracy and history matching can be conducted on the study model. Estimates of the gas flux into the wellbore will be obtained by integrating the velocity across the area of the open perforation sections. Hence

$$q_{wellbore} = \int_{Aperf} dl.\, \mathbf{U} * \mathbf{n}$$

(3.43)

Where   *Aperf* is as previously defined and

dl.U is the magnitude of the velocity at the wellbore

and *n* is the normal vector at the wellbore.

For obtaining accurate estimations of the flux through the system, a constraint can be specified on the Dirichlet boundary condition at the boundary through which the flux is being calculated – in this case the wellbore. The constraint specification gives more accurate results than direct evaluations in situations where a non-uniform source e.g. the amount of gas released from desorption with time, makes the solution in the domain non-linear. An optimization algorithm, which makes use of the concept of constraints –referred to as Lagrange multipliers is built in to the software to enable this. The concept of the Lagrange multipliers introduces an additional degree of flexibility in the specification of the length of the wellbore radius, and dealing with the meshing complexities that may arise as a result of small edge elements, and is implemented in this study for validation of production rates simulated at the wellbore.

CHAPTER 4

RESULTS AND DISCUSSION

4.1   Introduction

The objectives of this research work as stated in chapter 1 are to:

- Utilize COMSOL to predict migration patterns of shale gas in fractured media

- Investigate the range of conditions that favor the direction of fluid flux towards the wellbore.

In this chapter, the results of studies associated with these objectives are studied by estimating what the effect of fracture network patterns are on flow in simulated geometry and by making use of an appropriate multi-physics boundary condition to estimate and model possible gas flux out of the system. These results are obtained by making use of the model built in chapter 3, and are presented in the sections that follow. For a model to be accepted as being representative of the system it describes, its outputs need to be verified either by assessing them with analytical results or comparing them to previously published solutions describing the same systems.

4.2   Validation of semi-explicit fracture representation using COMSOL

The applicability of the conceptual model and governing equations presented in the previous chapter is now demonstrated by means of simulation of flow scenarios likely to be encountered in a hydraulically fractured shale formation. The objective of the first case study is to demonstrate how well COMSOL models flow in the ultra-low permeability shale formation, and how the model performs as a tool for prediction of migration patterns of shale gas in fractured media by implementing a semi-explicit representation of hydraulic fractures. The model only

considers the effect of hydraulic fractures on the production in the formation as a base case scenario. The model is formulated around values obtained from one production stage and the production stage is assumed to be made up of 5 perforation clusters spaced 80ft apart. The perforation clusters are hypothesized as planar hydraulic fractures.

The domain consists of a 2000 ft. long, 300 ft. thick portion of a producing shale formation extending 2000 ft. in the transverse direction and completed using cased perforations. The hydraulic fractures are modeled using the reduced dimensionality formulation described in the previous chapter and the effects of adsorption are accounted for. The input data employed for this simulation case study was based on average reservoir data from the Barnett Shale and was obtained from the system modeled by Yu et al. (2014). This data is presented in **Table 4.1.**

Table 4.1   **Fracture and Reservoir Parameters utilized for study**

Parameter	Value	Units
Reservoir Properties		
Initial Reservoir pressure	3800	psi
Model dimensions (L x W x H)	2000 x 2000 x 300	ft
Perforated stages	1 stage with 5 perf.	clusters
Perforation spacing	80	ft
Matrix permeability	1.0×10^{-4}	mD
Porosity of the matrix	5	%
Rock density	2580	kg/m^3
Langmuir pressure	650	psi
Langmuir volume	96	ft^3/ton
Temperature	180	^{0}F

Table 4.1.   Fracture and Reservoir Parameters utilized for study (cont'd)

Parameter	Value	Units
Well-bore Properties		
Well-bore pressure	1000	psi
Well-bore radius	0.25	ft
Hydraulic Fracture Properties		
Hydraulic fracture porosity	100	%
Hydraulic fracture half-length	500	ft
Hydraulic fracture height	300	ft
Hydraulic fracture permeability	5.0×10^3	mD
Number of fractures	5	
Fracture spacing	80	ft
Fracture Aperture	0.02	ft
Fluid Properties		
Density	0.716	kg/m^3
Gas Constant	8.314	kJ/(kmol*K)
Molar mass	16	g/mol
Fluid compressibility	2.5×10^{-4}	psi^{-1}

A schematic of the modeled domain is presented in **Figure 4.1**. In this figure, the reservoir is located at a depth of 7000 ft in the subsurface and only half of the domain is modeled on the basis of symmetry about the xz- plane at y = 0 ft. A symmetry boundary condition cannot be assumed about the xy-plane as the formation pressure can vary linearly with depth. A no flow boundary is specified at all other external boundaries of the formation and a well-bore pressure held constant at 1000psi.
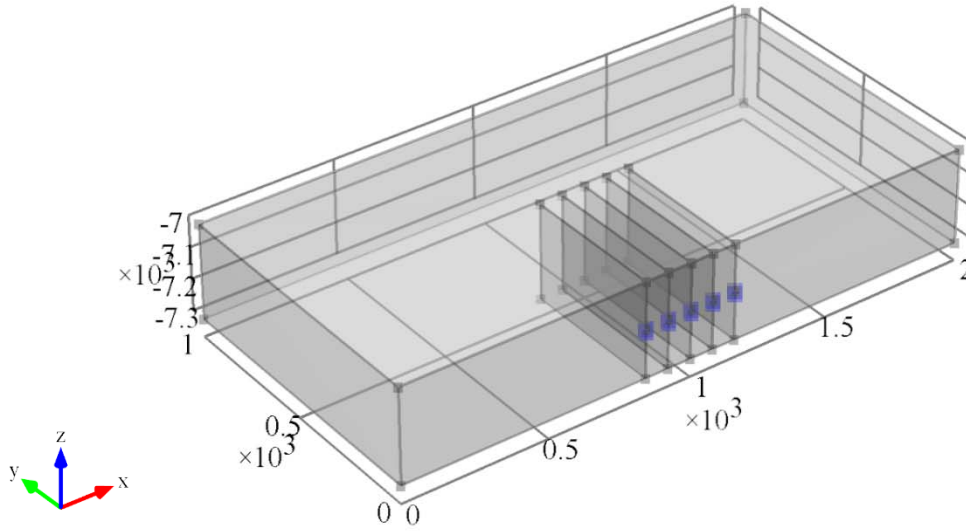
Figure 4.1   3D view of planar hydraulic fractures located in a modeled domain symmetrical about the xz-plane. The blue points represents the well-bore perforation points through which gas flow out of the system is captured.

By utilizing the concept of symmetry, the production rate forecast for the whole domain is obtained by multiplying the simulated rates by a factor of two. This reduces the number of grid elements required for the finite element study and correspondingly reduces the associated execution time. Although we are trying to simulate production from a fracture stage, a larger extent of the reservoir is modeled so that the flow in the formation is not controlled by the boundary.

4.2.1. Finite Element Mesh Selection

In simulations that make use of finite element methods, the finite element mesh serves a dual purpose:

i. To serve as a framework for the representation of the solution of the physics being solved for and

ii. To discretize the finite element domain into smaller grid blocks over which the set of equations describing the solution to the governing equations can be written.

The minimum element size is chosen as half of the smallest feature in the domain, that is, the well-bore radius, with a maximum growth rate of 1.25. The maximum finite element size was specified as one-third of the reservoir height. For this scenario, the software generates a high quality mesh consisting of 58, 172 tetrahedral elements incorporating refinements around the fractures as shown in **Figure 4.2**.

The mesh quality usually gives a good indication of the accuracy of a simulation based on the solution of partial differential equations. In COMSOL, a size quality of each element is used as a measure of the mesh quality. For a tetrahedron, the quality measure is evaluated by the formula

$$mesh\_q = \frac{72\sqrt{V}}{(h_1^2 + h_2^2 + h_3^2 + h_4^2 + h_5^2 + h_6^2)^{3/2}}$$

Where V denotes the volume of the element and h' s the length of the element edges. For an optimal tetrahedron, the value of $mesh\_q$ becomes 1, else its value is less than 1. It is usually desirable to have a mesh with a minimum element quality of 0.1 or above.

It is also important to perform a mesh refinement study in order to ensure that the computational results obtained from a numerical modeling procedure are free of any numerical

effects that might be associated with the discretization of the system during the translation of the physical equations to the form being computed by the numerical solver. The results of our mesh refinement studies are presented in Appendix D.
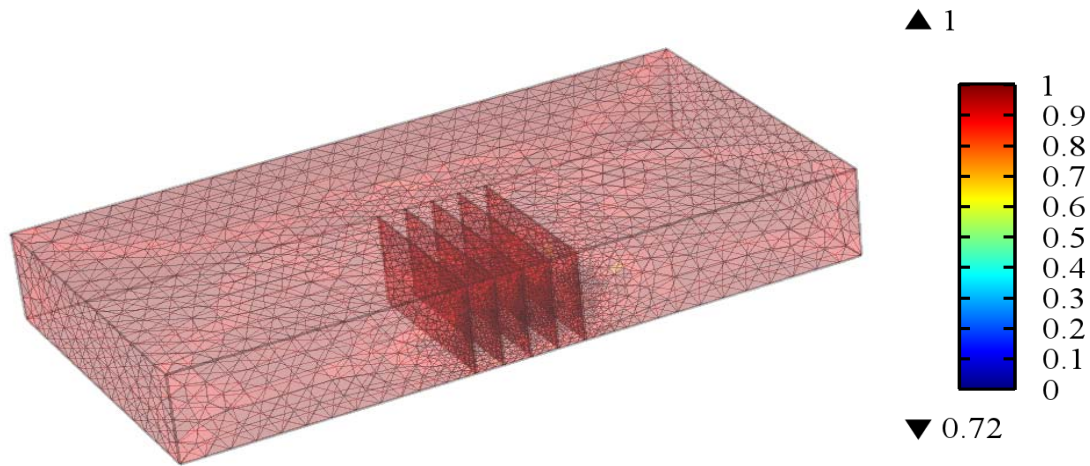
Figure 4.2   3D surface map showing the quality of the tetrahedral mesh elements utilized in the simulation

4.2.2. Initial Conditions and Solver Settings

Although pressures in the subsurface varies linearly with depth, pressure in shale gas formations typically exceed the hydrostatic pressure component. The pressure distribution across the whole formation is therefore specified only as a function of the overpressure in the shale. The model is initialized with a homogenous pressure distribution of 3800psi in the model domain. The Backward Differentiation Formula (BDF) is selected as the time stepping algorithm in the solver with an initial time step of 0.0001 days. The low value of the initial time step is selected in order to resolve the strong transients that might be introduced into the system as a result of the jump in

boundary condition at the wellbore relative to the initial pressure of the reservoir domain. The study was conducted for a simulation period of 30 years.

Figure 4.3 presents the cumulative production comparative plots, indicative of a good match between the results obtained by making use of the conceptual model and data values (See Appendix E) obtained using a fully explicit hydraulic fracture representation using CMG reservoir simulator by Yu et al. (2014).
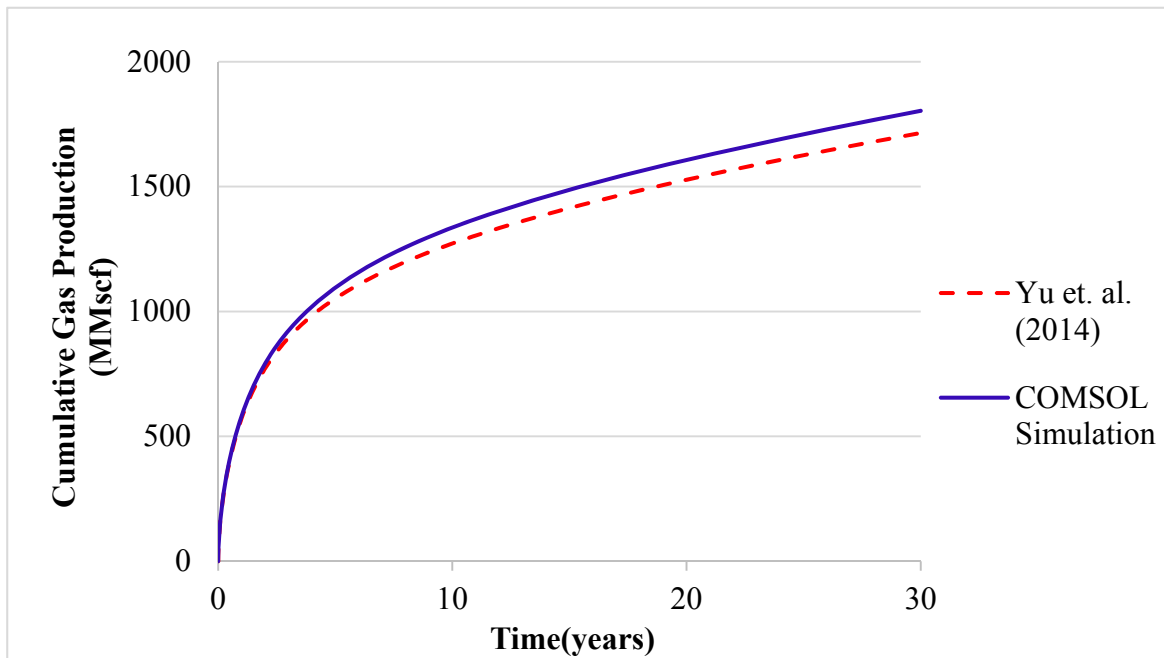
Figure 4.3   Comparison of cumulative production values obtained from a COMSOL Multiphysics simulation -utilizing a reduced dimensionality formulation for hydraulic fracture modeling, and reported data obtained using a fully explicit hydraulic fracture representation using CMG reservoir simulator by Yu et al. (2014).

The pressure profile in the domain at different simulation times is presented below.

(a)

Pressure (psi)

(b)

(c)
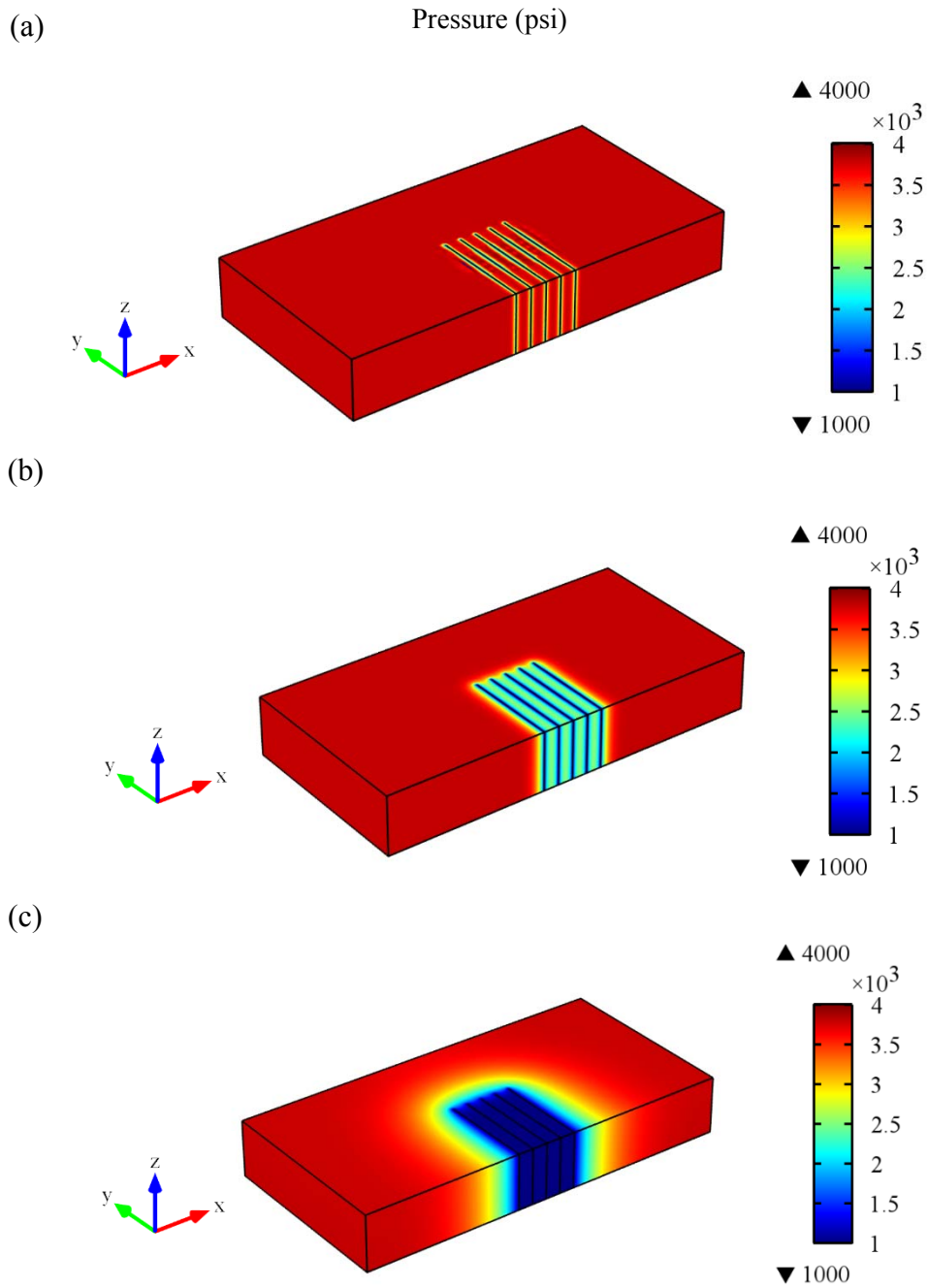
Figure 4.4   Surface map showing propagation of pressure front in the simulated domain at (a) 1 month, (b) 1 year and (c) 30 years respectively.

In **Figure 4.4(a)** above, it can be observed that the pattern of pressure dissipation is linear around the fractures after a study period of one month, suggesting that the high permeability zones of the hydraulic fractures allow transmission of the reduced pressure at the well-bore to the surrounding formation. After a 1 year simulation period however, interference effects can be observed in the stimulated zone. This pattern continues till the 4th year of the study (See **Figure 4.5**) after which the pressure front extends beyond the stimulated zone into the rest of the formation in an elliptical pattern as can be seen in **Figure 4.4(c)**.
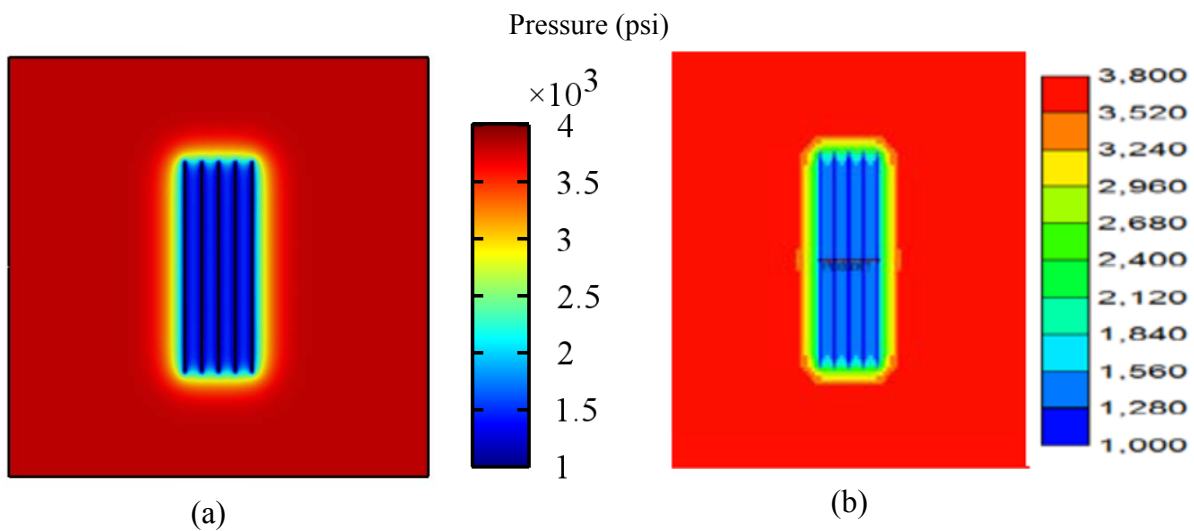
Figure 4.5   Compound linear pressure dissipation pattern in the simulated domain after 4 years of production from (a) COMSOL simulation (b) Yu et al (2014) study.

Pressure transient analysis in reservoir formations is utilized to characterize the different flow regimes in the formation with time. However, an advantage of studying the fractured domain using the COMSOL Multiphysics software package is the ability to visualize the velocity evolution i.e. the migration patterns of the fluid in the simulated domain in addition to observing the pressure dissipation. In **Figure 4.6**, transient fluid movement patterns around the fractured region in the formation is presented.
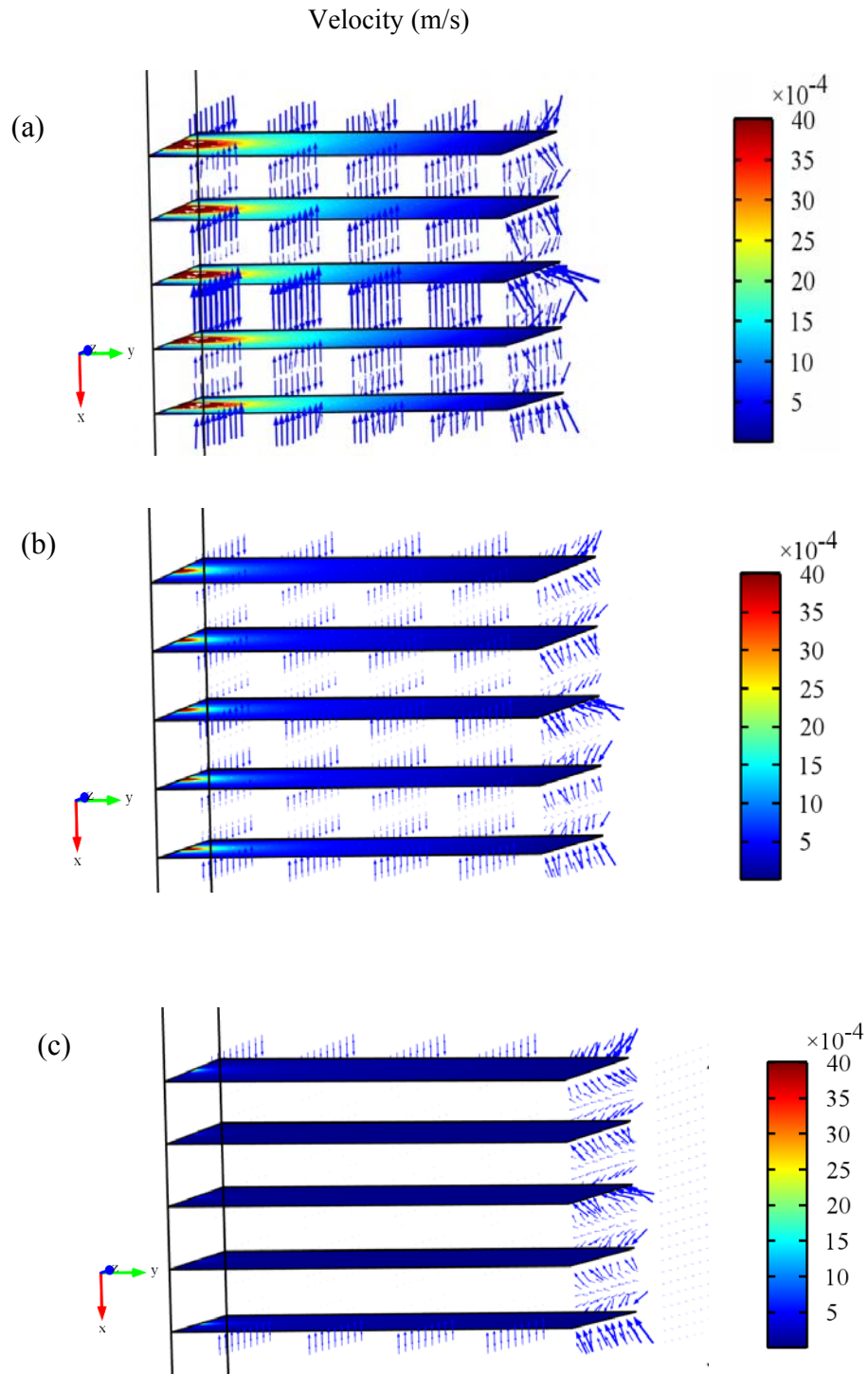
Figure 4.6   Fluid flow directions in the hydraulically fractured region consisting of 5 fractures after a simulation period of (a) 1 month, (b) 1 year and (c) 10 years respectively. The surface plots show the magnitude of velocity in the fractures while the arrow lengths are indicative of the velocities in the formation.

Whereas characterization of flow regimes in shale formations completed using multiple fractures and horizontal wells have been approximated mainly by the use of pressure maps and analytical plots (Freeman et al., 2013, van Kruysdijk & Dullaert, 1989), the visualization presented in **Figure 4.6** simplifies and enhances the process of characterization of these transient flow regimes.

The arrow plots presented in **Figure 4.6** correspond to the flow regimes in the formation with time. After the first month of production, the fluid flows in in the hydraulic fractures at a rate of about 0.004m/s at areas closer to the wellbore, while the values observed at the fracture edges farthest from the well-bore is about 0.0001m/s. Flow is observed to be directed towards each of the fractures in the fractured area. The length of the arrows are indicative of the magnitude of velocity and the arrow heads indicate the direction of fluid movement. These values have been multiplied by a scale factor of 3E9 in the three cases for visualization. The magnitudes of the velocity are observed to be smaller in the region around the hydraulic fractures after the one year period (**Figure 4.6b)** and a reduced velocity is also observed in the fractures – from the surface plot. This suggests a diminished production capacity in the stimulated zone and can be attributed to an increased resistance to mass transfer in the fractured zone.

In **Figure 4.6c**, it is observed that no velocity arrows are present in the fractured zone and flow into the fractured area comes mainly from the surrounding formation that fracture interference has occurred. Fracture interference occurs when the pressure head at an adjacent fracture is significantly lowered as a result of production from a nearby fracture. As a result, both fractures would produce less than they normally would in the absence of the other fracture. This effect can further be demonstrated by examining the production rates from the individual fractures at different time periods as shown in **Figure 4.7**.
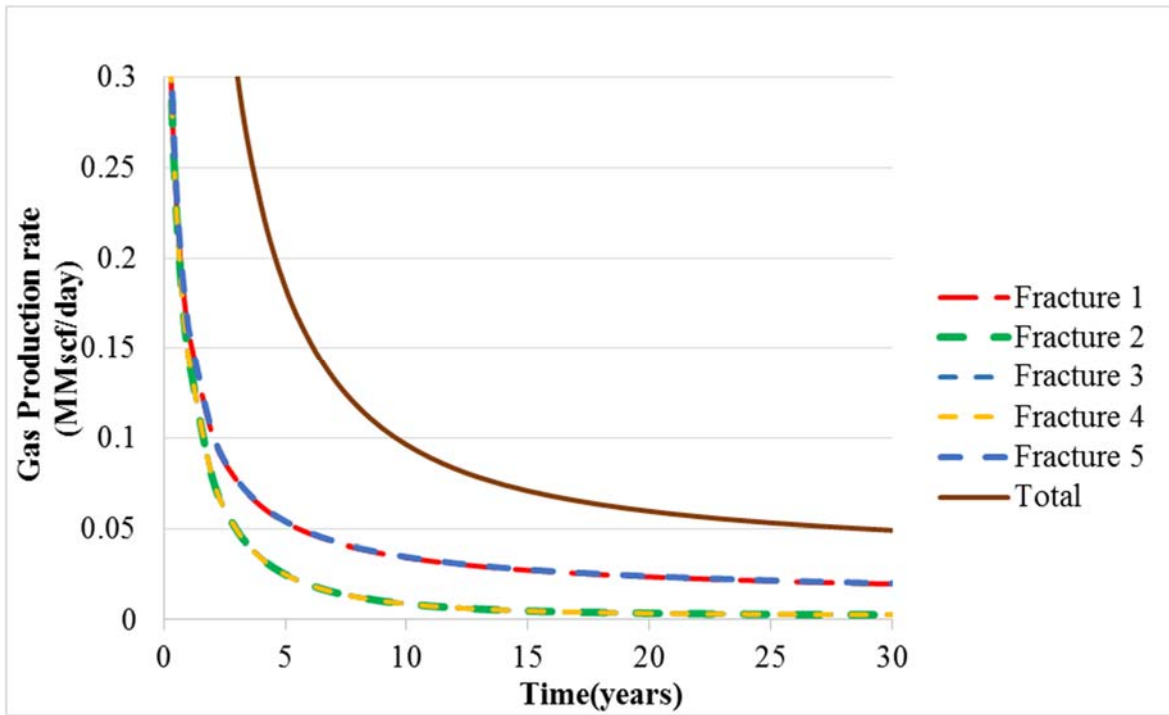
Figure 4.7   Gas production rate showing contributions from individual fractures over a 30 year simulation period.

Initially, all the fractures are producing at the same rate and contribute equally to the total production from the formation, however after a 3-4 year period, we observe a difference in the production rates from the external fractures, denoted by Fracture 1 and Fracture 5 from what is observed in Fractures 2, 3 and 4, the internal fractures. By the end of the 30 year simulation period, gas flow through the external fractures makes up 82% of the total production further suggesting that depletion of gas has occurred in the fractured zone and gas movement is now predominantly from the unstimulated zone of the formation.

The results of this test case show that the semi-explicit representation of the fractures can be employed for the simulation of flow in a hydraulically fractured shale formation, and gives results that have a good match to model results obtained using a fully explicit hydraulic fracture representation. This technique reduces the computational requirements associated with numerical modeling using fully explicit models. In addition, the software offers a tool for better visualization of the flow regimes in the formation, and a better understanding of gas movement patterns in shale.

4.3   Validation of developed upscaling technique

The validity of the semi-explicit approach for fracture representation has been demonstrated by the scenarios presented above. However, in situations where complex fractures – such as the secondary fractures observed in the vicinity of areas containing fractures with high length to width ratios, the semi-explicit representation of individual fractures possessing low aspect ratios becomes computationally implausible, and continuum models present the most effective mode of capturing the physics of the formation.

This study aims to demonstrate the ability of a novel algorithm for the generation and modeling of complex fracture geometries. The upscaling technique is used to calculate the modified values of the formation permeability required for the solution of the flow equations, when the presence of fractal patterns results in a meshing challenge for the computational software. The validity of the upscaling approach, which was discussed in section 3.7 is investigated. An important aspect of the upscaling approach is the choice of the subdomain grids utilized for the procedure, and so the effect of fine scale and coarse scale subdomain selection was evaluated. The model is formulated around values obtained from one production stage and the production stage

90

is assumed to be made up of one planar hydraulic fracture located in the middle of the formation. The domain consists of a 2000 ft. long, 300 ft. thick portion of a producing shale formation extending 2000 ft. in the transverse direction similar to the base case scenario. All other model parameters are the same as for the base case scenario.

First, the planar fracture to be upscaled is generated using the MATLAB fracture generating program and subsequently processed using a clipping and upscaling subroutine. The data points obtained from upscaling program represent discrete points which are spatially distributed in the domain and require a smoothing procedure before it can be suitable for use in COMSOL. This smoothing procedure is carried out using the kriging subroutine. The kriging weights utilized is $1/D^2$, where D is the distance between computed data pairs. A listing of the programs used for this study is presented in Appendix F. The final output from the MATLAB program is a text file containing coordinates of the centroids of the subdomain, along with upscaled permeability and porosity values.

These values are imported into the simulation software using a linear interpolation function. For points not present within the boundaries of the imported geometry, a constant permeability value was specified for extrapolation. This value is equivalent to the permeability of the matrix. In the results that follow, the effects that the gridding scheme, either logarithmic or regular, and the different subdomain sizes, that is, the number of subdomains (N) through which the system is upscaled, have on the distributed permeability data obtained from the upscaling algorithm is presented.
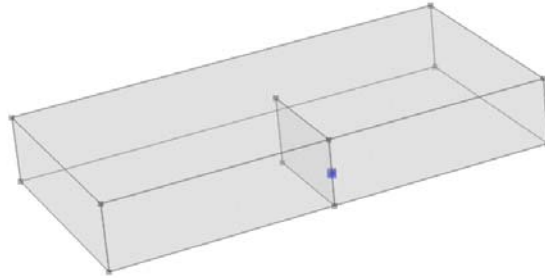
Figure 4.8   Geometry representing model domain to be upscaled.

Permeability (mD)

(a)   N = 50, **r** = 8

(b)   N = 150, **r** = 8

(c)   N = 290, **r** = 8
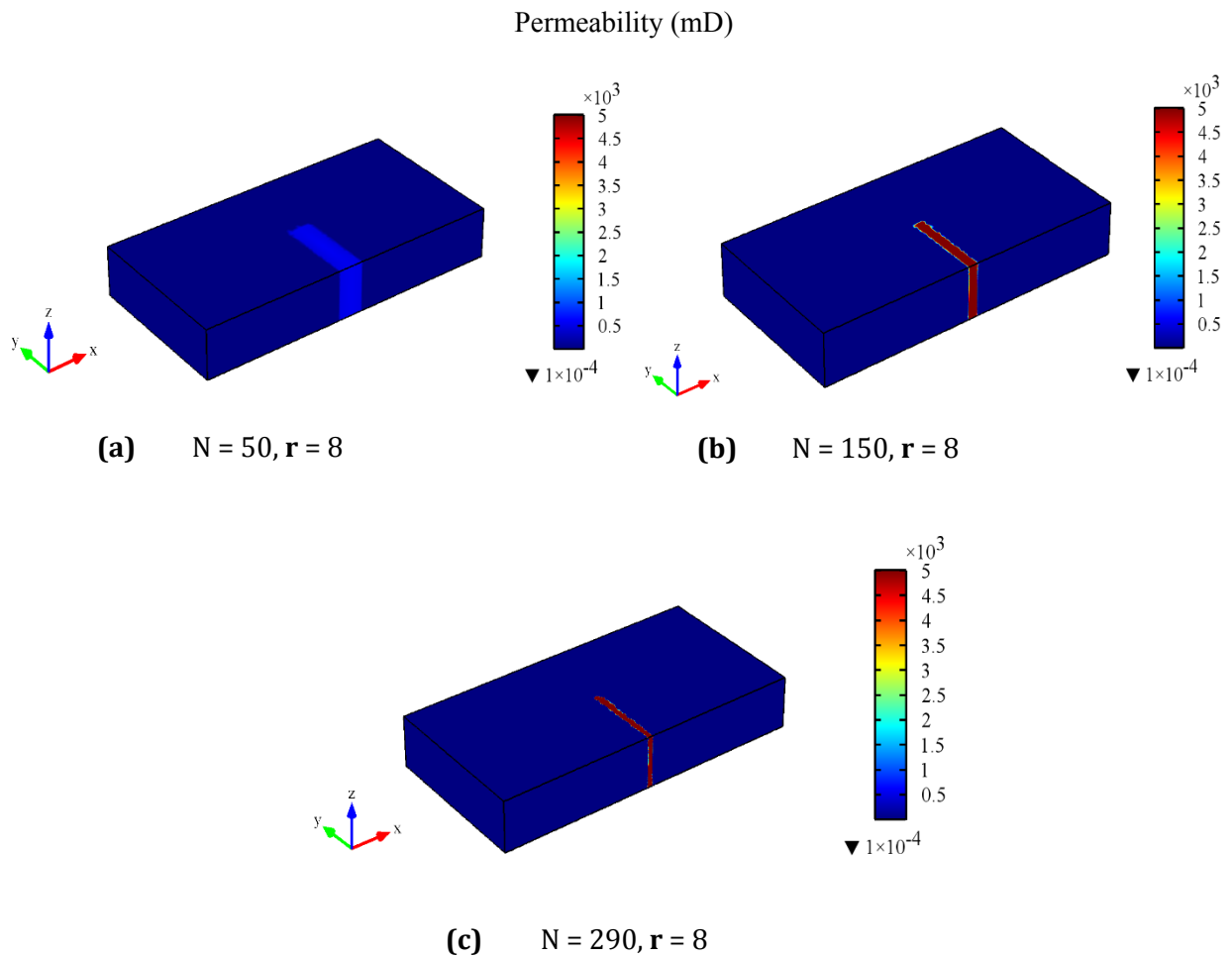
Figure 4.9   Y-directed permeability distributions (Kyy) from kriging data with N subdomains and r neighbors (points used for interpolation) using a logarithmic gridding scheme along the axis of the wellbore (x-axis).

Permeability (mD)

(a)   N = 50, **r** = 3

(b)   N = 50, **r** = 8

(c)   N = 150, **r** = 3

(d)   N = 150, **r** = 8

(e)   N = 290, **r** = 3

(f)   N = 290, **r** = 8
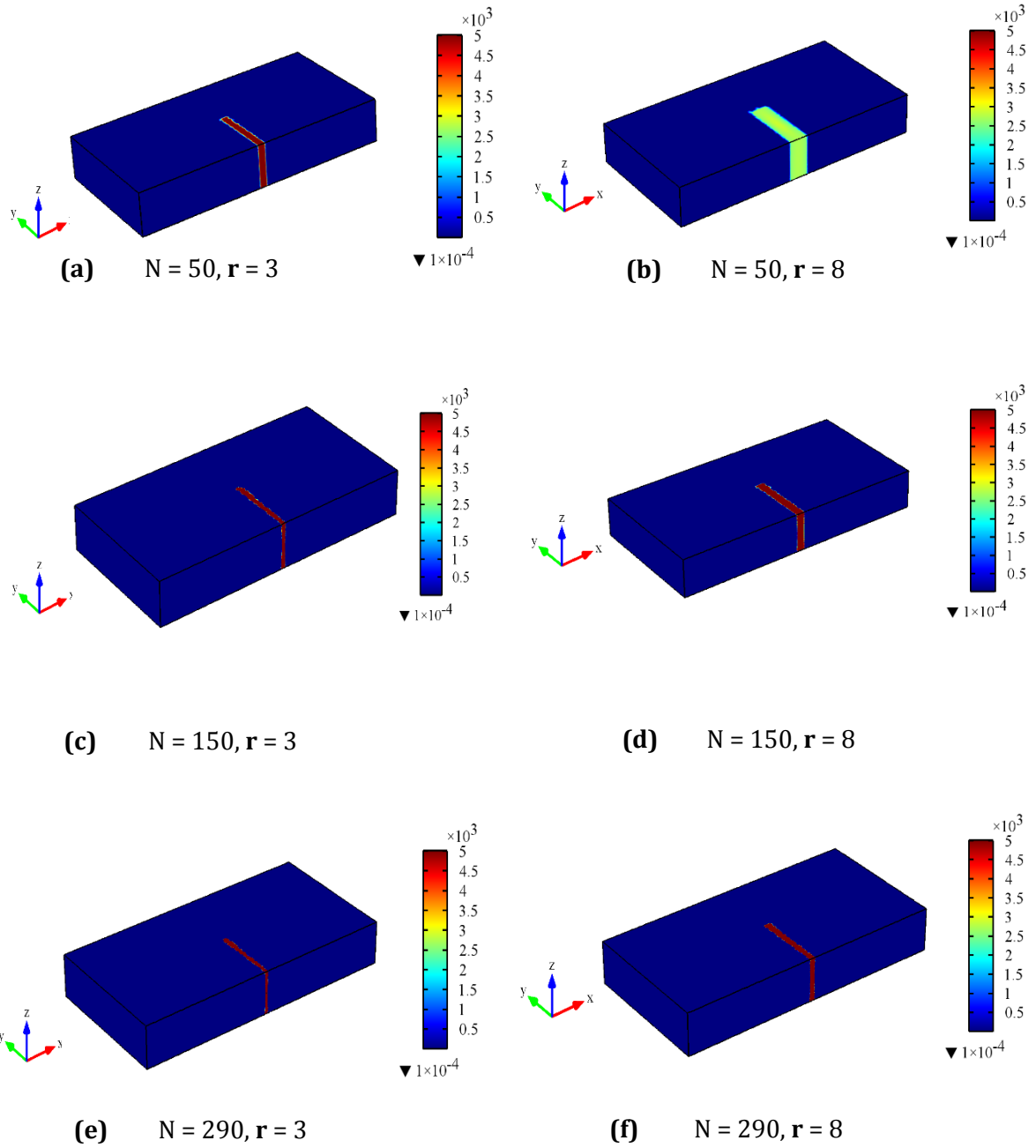
Figure 4.10   Y-directed permeability distributions (**K**$_{yy}$) from kriging data with **N** subdomains and **r** neighbors (points used for interpolation) using a regular gridding scheme.

Figures **4.9** and **4.10** show the upscaled y-directed permeability distributions (Kyy) obtained from the kriging data. The permeability values remain constant in the x-direction, as fracture lies in the yz-plane. It is observed that an increase in the number of subdomains (**N**) decreases the apparent penetration of the permeability values to the neighboring grid cells. Also, a similar effect is observed by reducing the number of neighbors (**r**) implemented in the kriging interpolation for both gridding techniques.

The logarithmic grid utilizes a grid size Δx of 38ft, 7.8ft and 3.8 ft for the largest grids along the wellbore direction, in the coarse, intermediate and fine grids (grids corresponding to N = 50, 150 and 290) respectively. In all cases, a 0.5ft grid size is implemented around the fractures. For the regular gridding system, the grid is evenly distributed at 19.2ft, 6.4ft and 3.8 ft intervals also corresponding to N values of 50, 150 and 290 respectively. An analysis of the steady state production data obtained from the upscaled system using the different subdomain scenarios is presented in the table below.

Table 4.2   **Steady-state Flux Simulation Results**

Number of subdomains (N)	*Flux (MMcf/day)*		*Logarithmic Grid*
	Regular Grid		
	r= 8	*r= 3*	*r= 8*
N = 50	0.01036	0.00982	0.01003
N = 150	0.00983	0.00961	0.00943
N = 290	0.00964	0.00943	0.00905

The values in **Table 4.2** when compared with a reference value of 0.00872 MMcf/day obtained by solving the model system using the semi-explicit approach suggests that the flux values converge to the reference solution at higher subdomain values. A convergence criteria was specified by specifying a relative error < 0.05. These results indicate that the upscaling technique is useful in the approximation of the permeability a domain containing fractures.

Next, results that demonstrate the ability of the code to handle multiple and complex fracture geometries is presented. Illustrations of some of the complex geometries that were tested with the upscaling methodology are presented in **Figure 4.11** below.
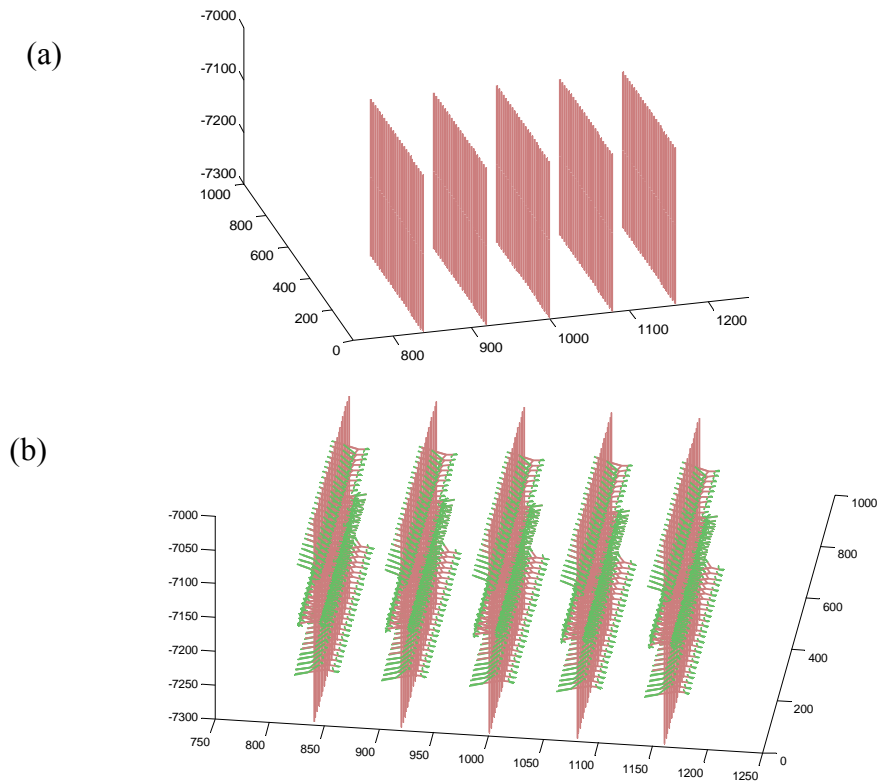
Figure 4.11   Fracture configurations generated by MATLAB for use in testing how well code handles complex geometry. (a) Scenario with multiple planar fractures and (b) Scenario with complex fracture pattern representing induced secondary fractures.

The configuration generated in **Figure 4.11(b)** incorporates 'tree' patterned fractures originating from the planar hydraulic fracture structure. This configuration becomes too complex to be modeled using a semi-explicit formulation. However as discussed earlier, the upscaling approach allows the permeability of the fractured system to be represented as a non-homogenous anisotropic continuum domain shown in **Figure 4.12**. This permeability distribution can be utilized in the analysis of flow and transport in complex formations. Perhaps the most important utility of this representation is that we can visualize the changes in the permeability over the domain as a result of the complex fracture system. In **Figure 4.13**, the x-directed permeability values for the geometry with and without complex fracturing is presented.

Permeability (mD)

(a)

(b)
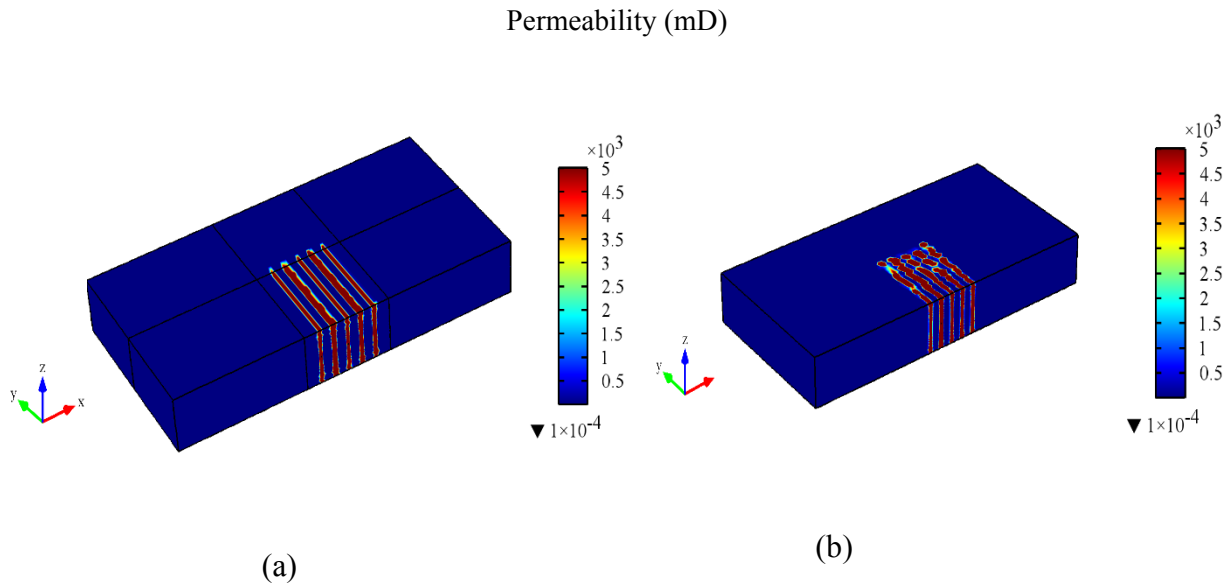
Figure 4.12   Y-directed permeability distributions (Kyy) from kriging data with N=75 subdomains and r =3 neighbors (a) Scenario with multiple planar fractures and (b) Scenario with complex fracture pattern representing induced secondary fractures.
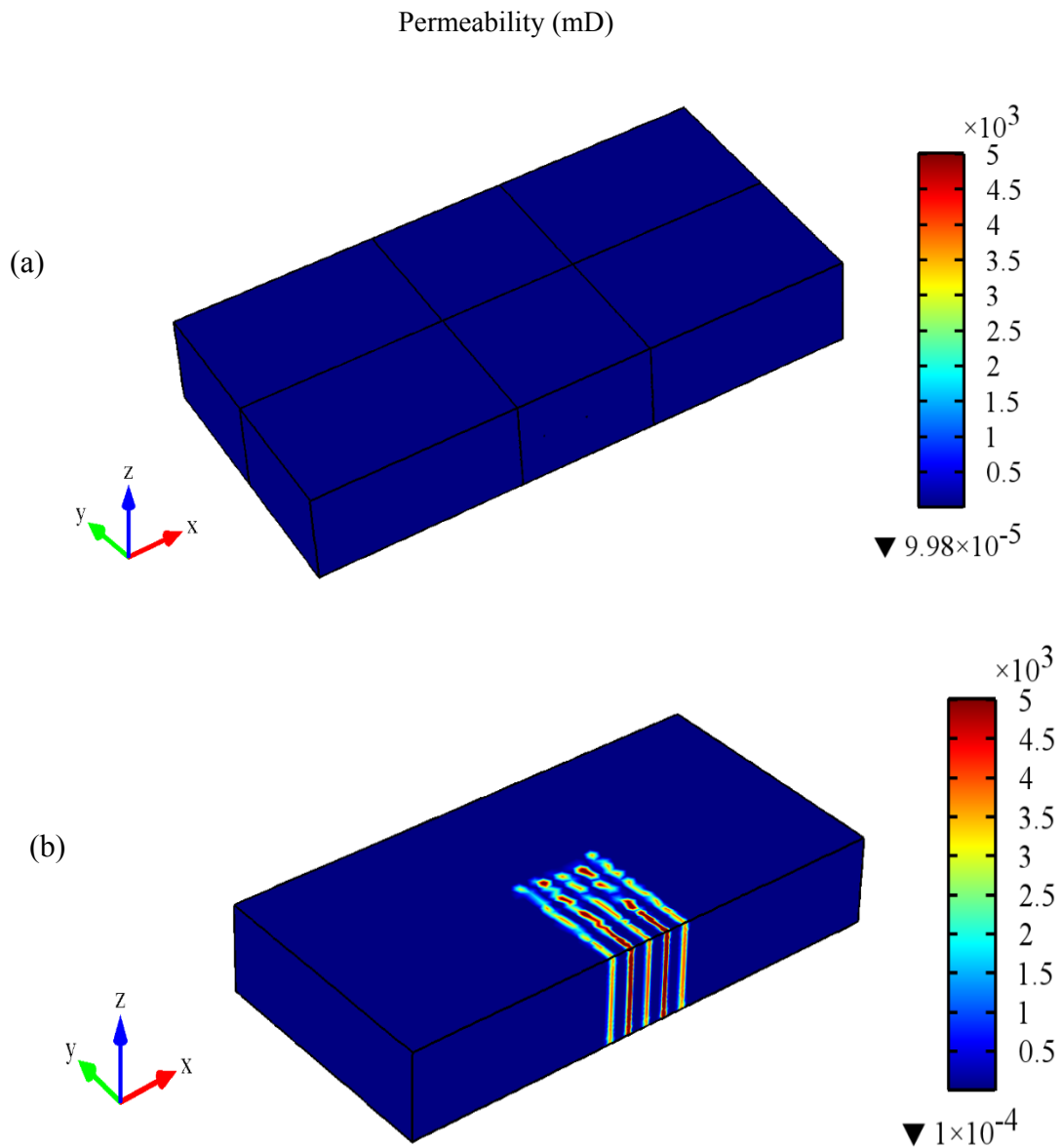
Permeability (mD)

Figure 4.13 x-directed permeability distributions (Kxx) from upscaled data in (a) Scenario with multiple planar fractures and (b) Scenario with complex fracture pattern representing induced secondary fractures, reflecting the higher x-directed permeability zones in the complex fractured scenario.

Higher values of the x-directed permeability value is observed in the complex fractured scenario as compared to the planar model, as the planar fractures in the yz-plane have no effect on

K_{xx}. The flow behavior arising from this type of scenario has not been presented in literature so far, as most conceptual models utilize the assumption of the bi-wing fracture geometry for hydraulic fractures. To validate the upscaling process therefore, the generated permeability distributions for the multi-planar fracture system presented in **Figures 4.12(a)** and **4.13(a)** are utilized in a transient study, and the performance of the non-homogenous porous medium approximation created by the upscaling process is compared to results from the semi-explicit representation of the planar fractures. This comparison is presented in **Figure 4. 14.**
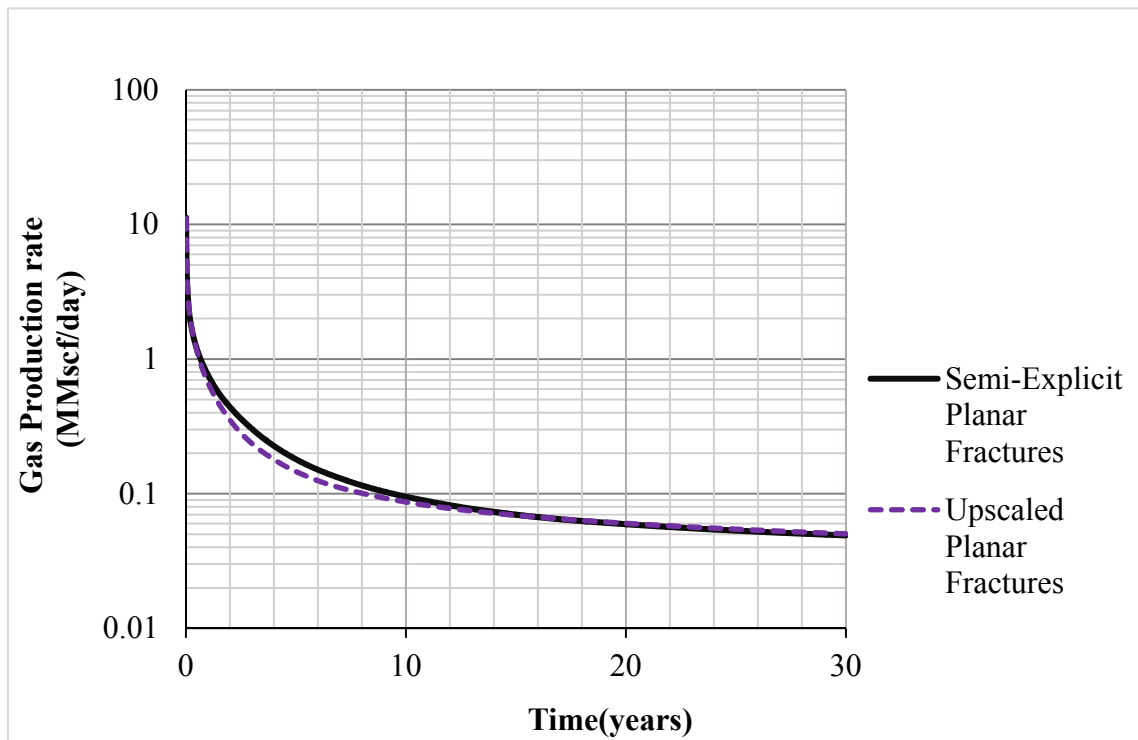
Figure 4.14   Comparison of daily production rate obtained from the upscaled formation containing multiple planar fractures to values obtained using a semi-explicit fracture representation.

It can be observed from **Figure 4.14** that gas production rates for a 30 year transient study utilizing the upscaling technique closely matches the production rates observed from the semi-explicit technique. The applicability of the upscaling methodology for the representation of single and multiple planar fracture geometries and its usefulness in the analysis of production from shale formations has been demonstrated by the results presented above. An investigation of the effect of the permeability distribution obtained for the complex case on flow in the modeled domain is presented in section 4.4.2.

4.4   Effect of fracture networks on flow

A comprehensive study of flow in fractured shale should include geometry elements describing the distinct fracture systems that are observable in a producing shale gas formation (see Section 2.4) in order to obtain a conceptual model that is most representative of the formation. The distinct features to be studied are:

a. The hydraulic fractures – which are already accounted for in the base case simulation;

b. Natural fractures - taken in this context to mean the existing lines of weakness in the formation parallel to bedding planes, and

c. Secondary fractures – induced smaller fractures that form a "cloud" around the planar hydraulic fractures

In the next set of simulations, we intend to account for each of these features and observe the effects that these have on gas production and flow patterns in the formation. These simulations are also intended to test the hypothesis that modeling of all the features is required for accurate modeling of gas migration in stimulated shale formations.

4.4.1. Model incorporating natural fractures

The base case simulation presented in section 4.2 takes into account the presence of hydraulic fractures in the formation. This next test is intended to assess the impact of the presence of natural fractures and their interaction with hydraulic fractures, on gas production and fluid flow in shale. As described in section 3.5, natural fractures in the model can be represented by semi-explicit layers parallel to the bedding plane. These layers may become connected as a result of hydraulic fracturing. The principal extent of the natural fractures is assumed to be bounded by the production stage, in order to minimize interference effects that may occur if the natural fracture extends into an adjacent production stage. Therefore, a width of 450 ft – the average length of a production stage- is assumed for simulation purposes. A porosity value of 0.25 is specified in the fracture in order to account for the fact not all parts of the bedding plane is fully open to flow. Other simulation parameters are obtained from the base case scenario in **Table 4.1** in addition to properties of the natural fractures, which are presented in **Table 4.3**.

Table 4.3   Natural Fracture Properties

Parameter	Value	Units
Natural fracture porosity	25	%
Natural fracture half-length	500	ft
Natural fracture width	450	ft
Natural fracture permeability	1.0×10^2	mD
Number of fractures	2	
Natural fracture spacing	100	ft
Natural fracture Aperture	0.02	ft

The newly conceptualized domain is as shown in **Figure 4.15**.The simulation was carried out for a study period of 30 years, using a finite element mesh consisting of 69, 816 tetrahedral elements incorporating refinements.
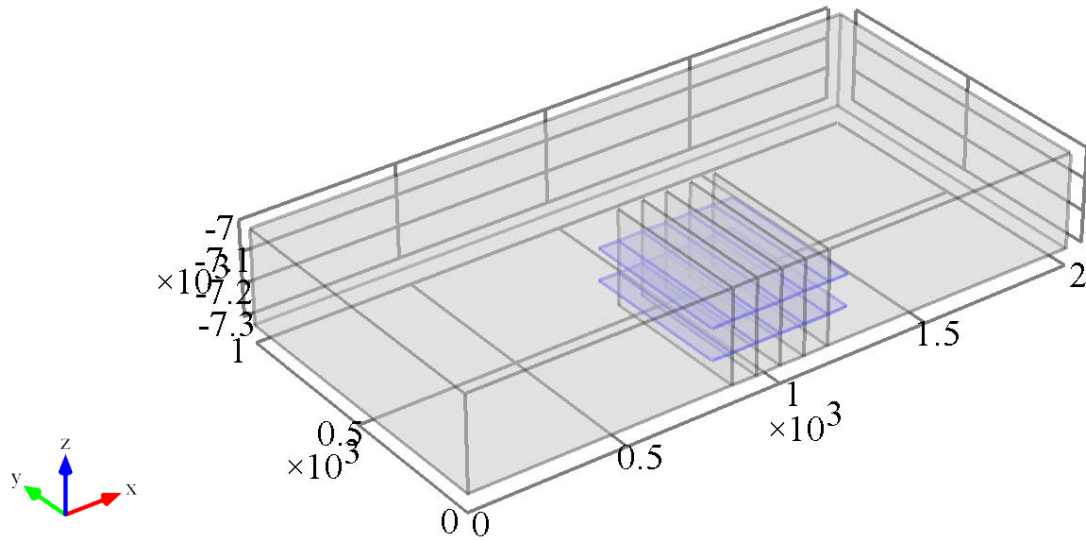
Figure 4.15   3D view of modeled domain with highlighted section showing the simulated planar natural fractures as light blue horizontal planes.

Surface maps of changing pressure with time are presented in **Figure 4.16**. The pressure dissipation pattern is observed to be similar to the pattern observed in the formation in the absence of natural fractures. Observation of the velocity patterns in the fractured region (see **Figure 4.17**) show that in addition to flow directed towards the hydraulic fractures, flow is also directed towards the planes of the natural fractures at early times (t<1year), while at late times there appears to be no observable difference in the flow patterns. This observation is supported by further analysis of the late time flow regime using gas production rate plots **(Figure 4.18a** and **4.18b)**
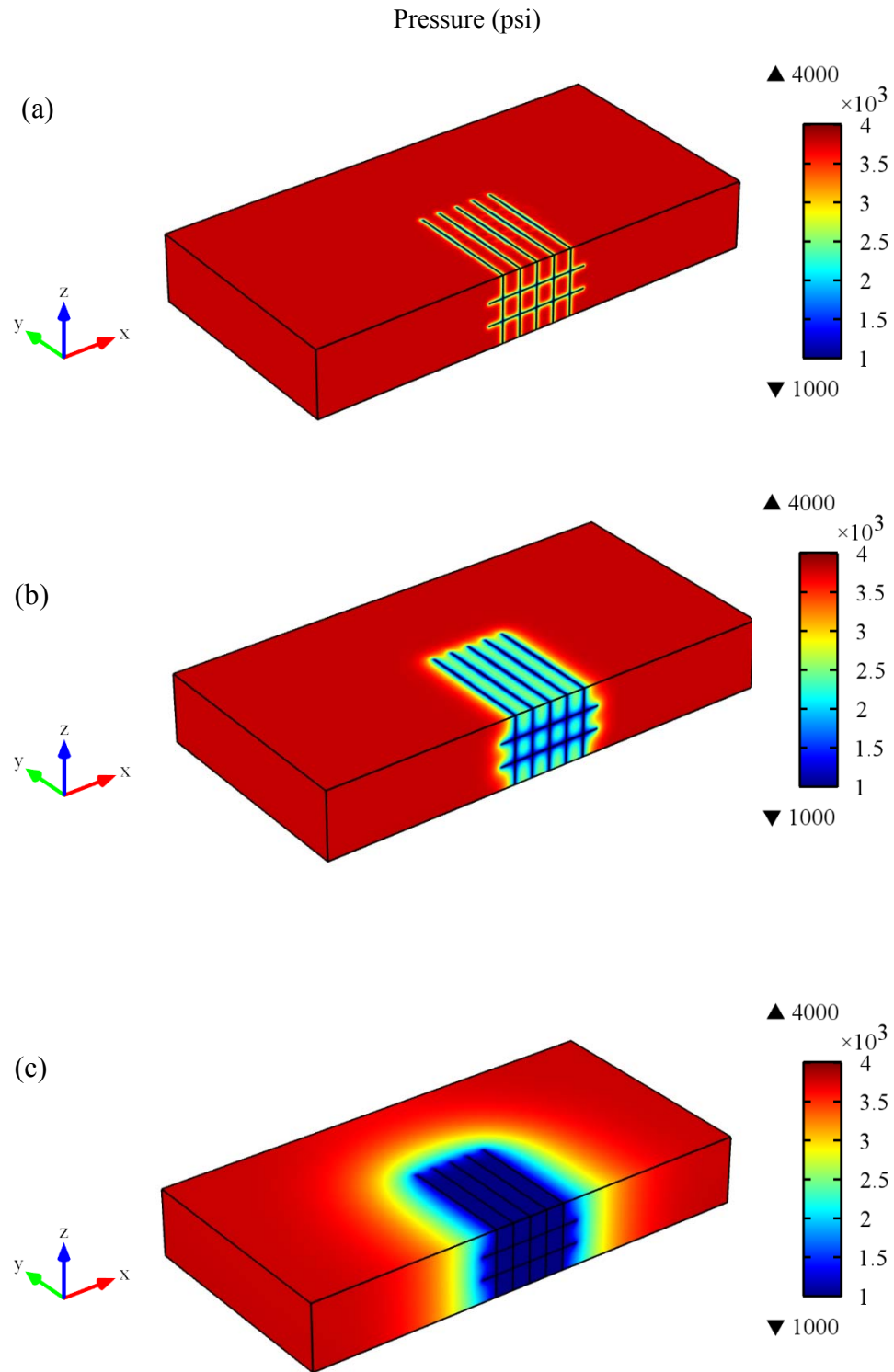
Figure 4.16   Surface map showing propagation of pressure front in the simulated domain with natural fractures at (a) 1 month, (b) 1 year and (c) 30 years respectively.
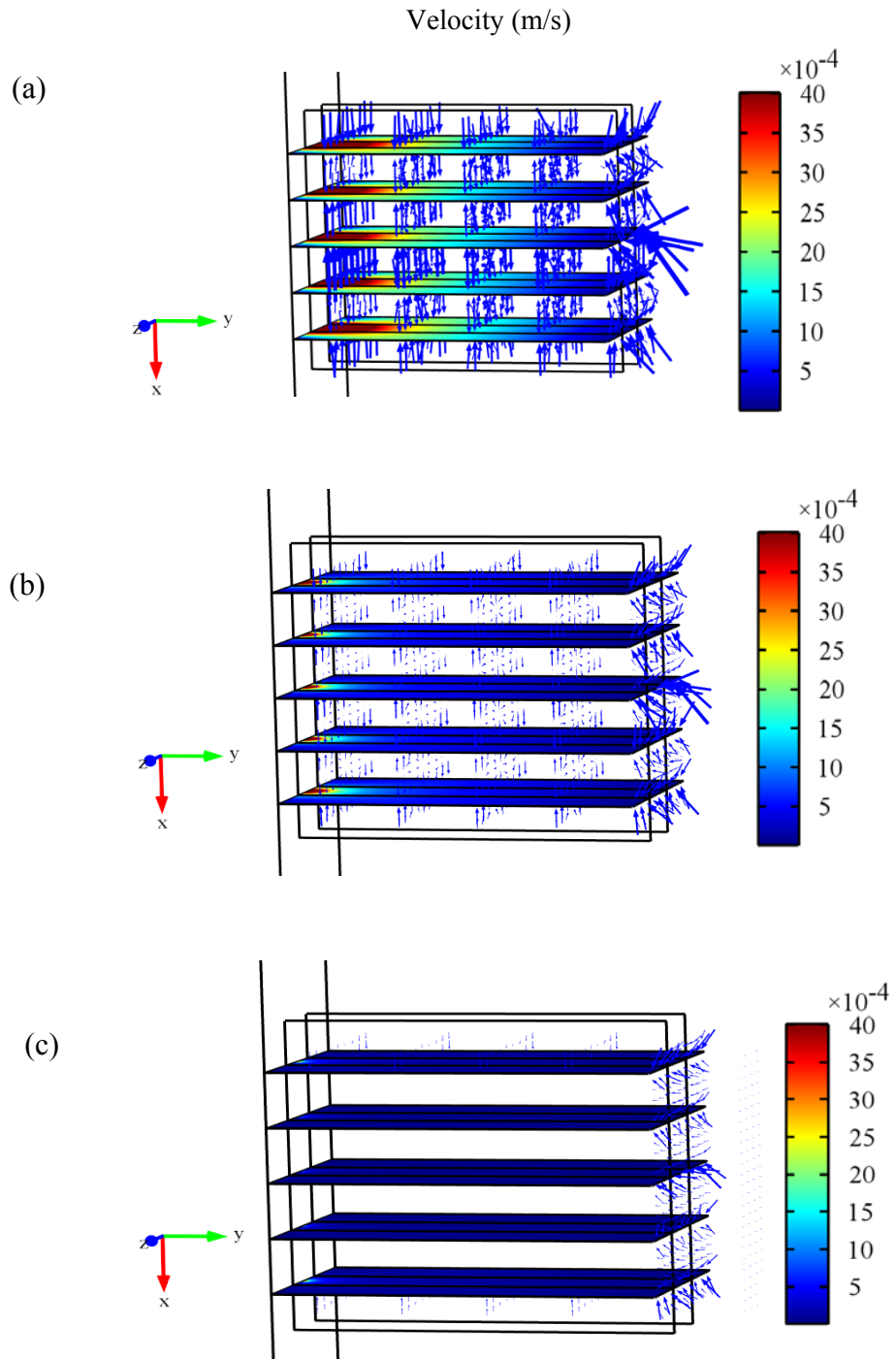
Figure 4.17   Fluid flow directions in the modeled domain consisting of both natural and hydraulic fractures after a simulation period of (a) 1 month, (b) 1 year and (c) 10 years respectively. The surface plots show the magnitude of velocity in the fractures while the arrow lengths are indicative of the velocities in the formation.
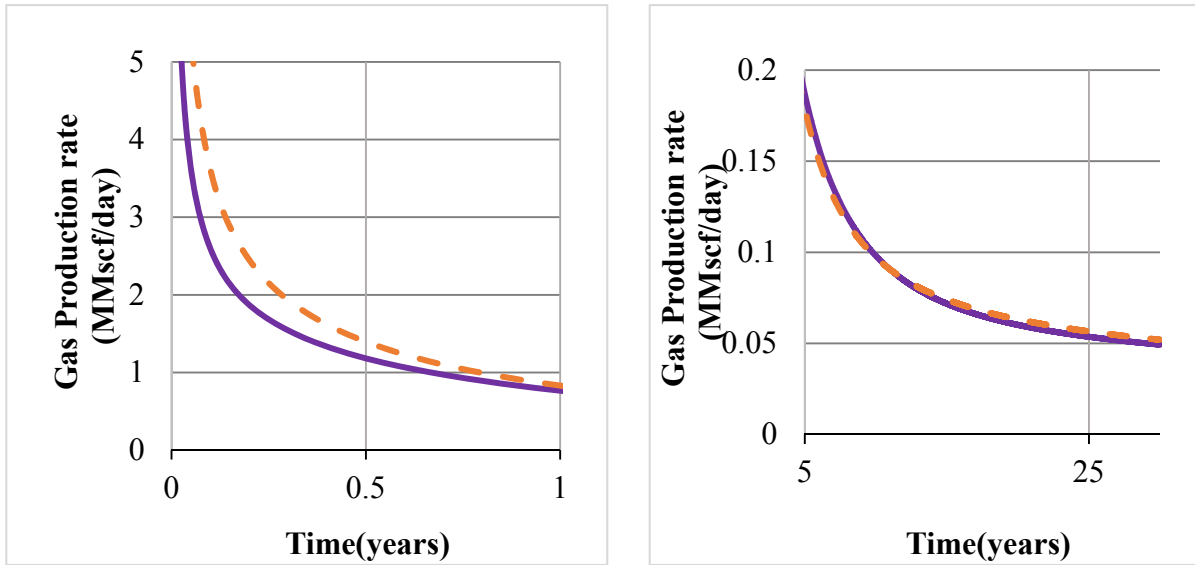
Figure 4.18 Comparison of (a) early time gas production rates (b) late time gas production rates and (c) cumulative production values in a domain containing natural fractures to a domain without natural fractures.

However, a comparison of the gas cumulative production values reveals a 10% increase in gas production from the domain with natural fractures (See **Figure 4.18c)** at the end of the simulation time period. By performing a careful analysis on the daily production rate data, it is observed that the difference in the production values is primarily the result of higher production rates at the early simulation times (t<1 year).

From the above results, it can be deduced that presence of natural fractures provides an additional stimulation surface area through which gas can be produced from the formation, and therefore leads to an increase in the production rate into the well-bore. These results show the need for an accounting of the presence of natural fractures in the formation for accurate simulation of a shale gas formation. A sensitivity analysis of the production rate as a function of size of stimulated area, other natural fracture parameters is presented in section 4.6, in order to ascertain the impacts of natural fractures on production from the wellbore.

4.4.2. Model incorporating secondary hydraulic fractures

In the next test, the effect of accounting for the secondary fractures is tested. All simulation parameters remain the same as for the base case scenario. The complex fractures are generated in MATLAB. The codes implemented for the generation of this case study is presented in Appendix F. The permeability of the secondary fractures are calculated using the formula from equation 3. Like the hydraulic fractures, the value of the secondary fracture aperture is taken as 0.02 ft. The fractal is allowed to have three daughter branches and extends in the horizontal direction away from the planar representation of the hydraulic fractures. The schematic representation of the modeled geometry is presented in **Figure 4.19**
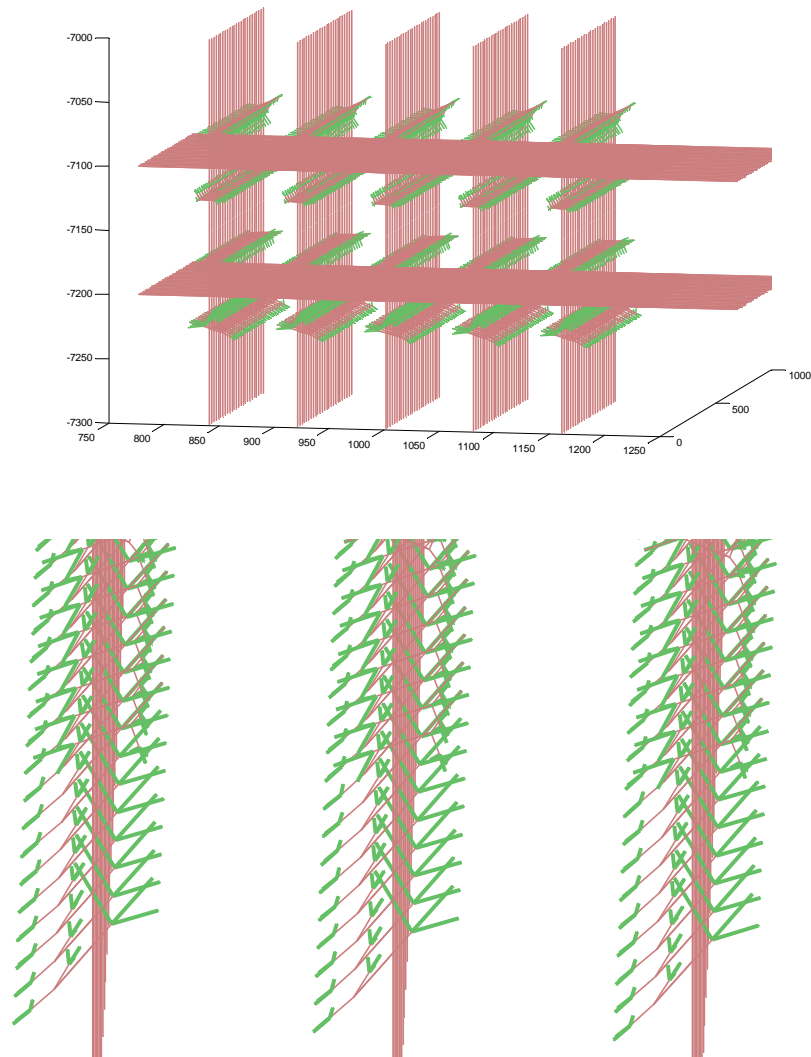
Figure 4.19 MATLAB configuration of fractured network incorporating hydraulic, natural fractures and complex secondary fractures (b) close-up view of fracture network showing 'tree' like secondary fracture structure.

The pressure dissipation patterns in the formation are presented after a simulation time period of 1 month, 1 year and 30 years respectively.
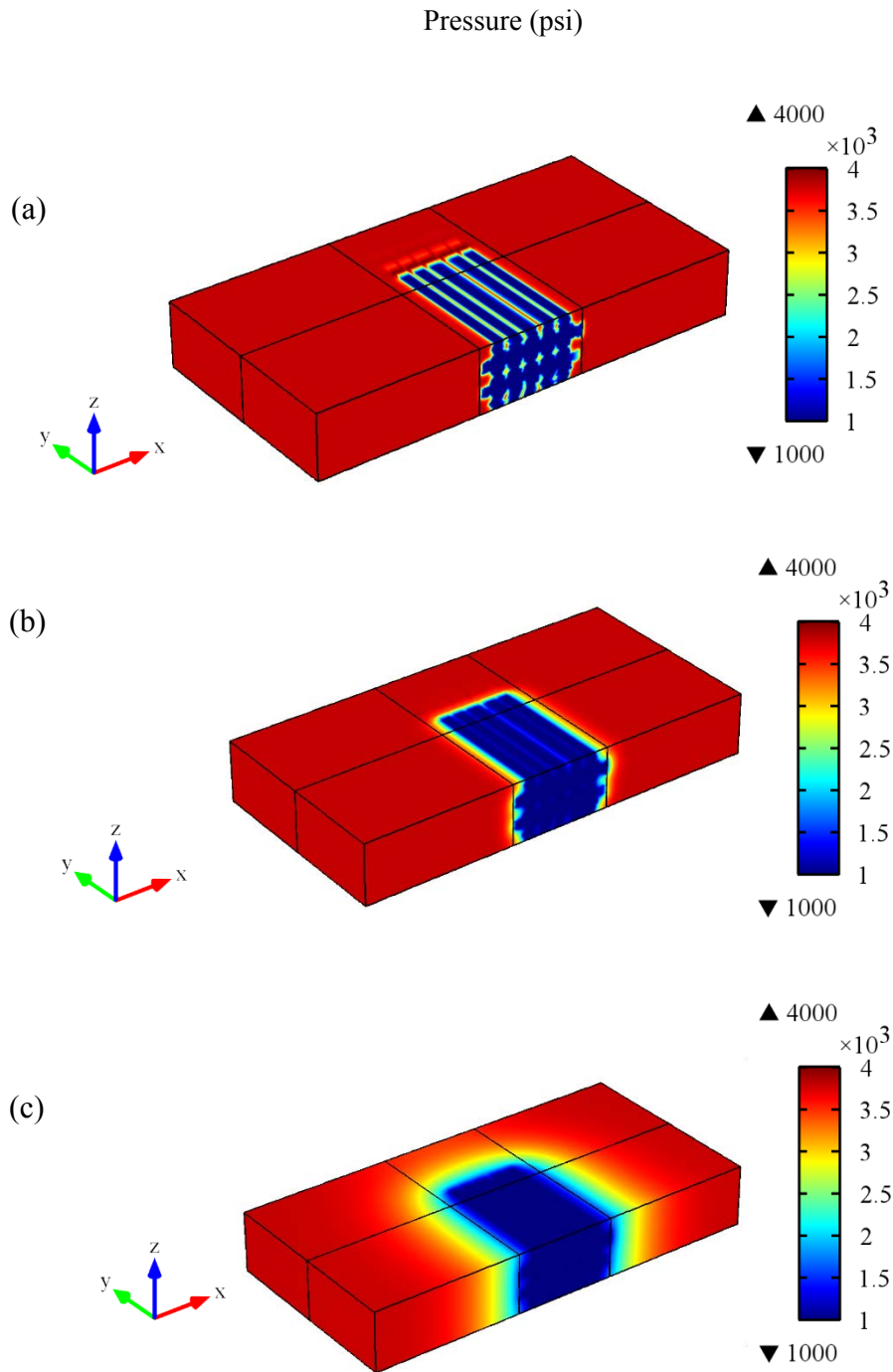
Pressure (psi)

Figure 4.20   Surface map showing propagation of pressure front in the simulated complex fractured domain at (a) 1 month, (b) 1 year and (c) 30 years respectively

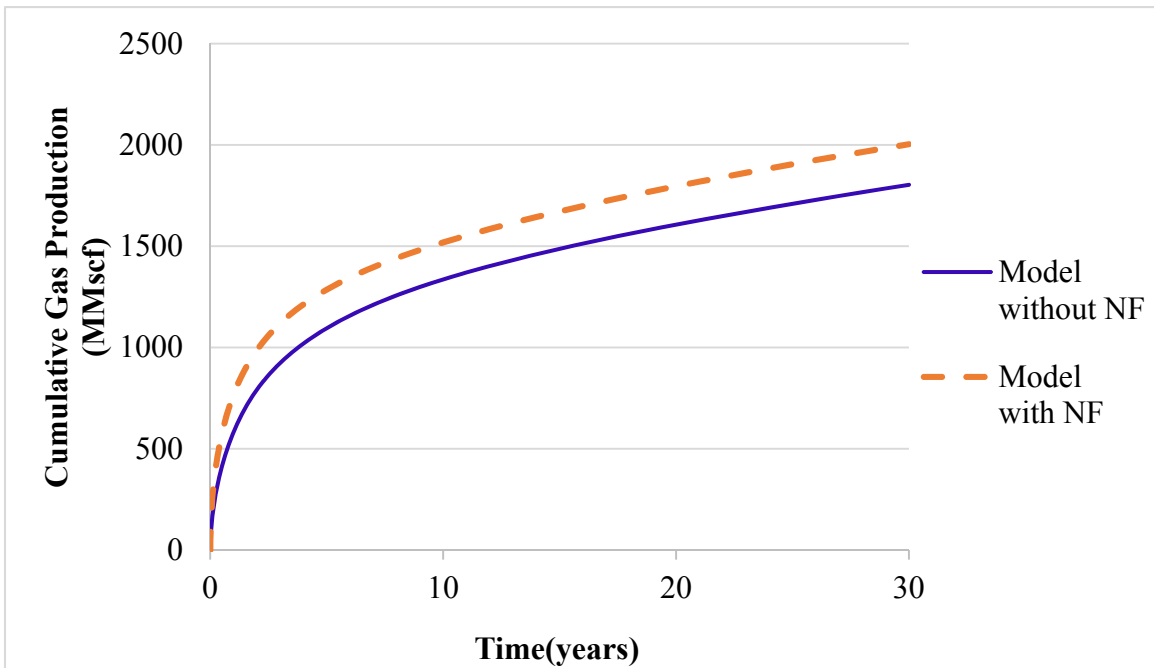In **Figure 4.21**, a comparison of the cumulative production data from the system containing upscaled complex fractures and a system utilizing the upscaled planar fractures alone is presented.
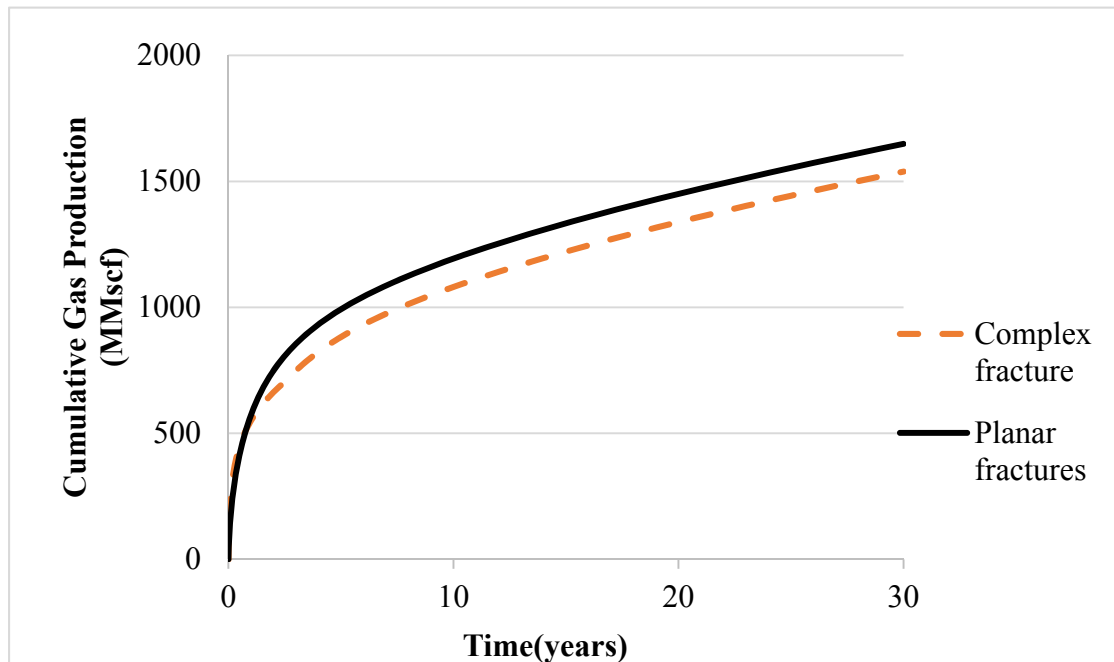
Figure 4.21 Comparison of cumulative production values in a domain containing planar hydraulic fractures to the simulated complex fractured domain.

At the end of the 30 year simulation period, the simulation model, higher production values are observed for the solution utilizing the planar fracture geometry. This can also be attributed to the effect of fracture interference in the stimulated zone. Thus **Figure 4.21** suggests that optimistic production values might be obtained when utilizing simple systems for the representation of fractures in shale gas systems, as interference effects that may arise as a result of the system complexity will be unaccounted for.

4.5   Effect of fault through model Boundary

In the studies considered so far, the producing formation is considered to be a closed system, with its only outlets existing through the perforations located at the wellbore. However, during hydraulic fracturing, there can be re-activation of closed/sealed faults presented at the formation boundary, which in turn leads to a change in the conceptualization of the boundary conditions. This study seeks to assess if movement of gas away from the shale layer is possible in the presence of a fault in the formation, i.e., if hydraulic fracturing of the shale formation can potentially lead to contamination of overlying aquifers. The simulation case to be tested is based on the hydraulically fractured formation with natural bedding planes and pre-existing fault shown in **Figure 4.22** below:
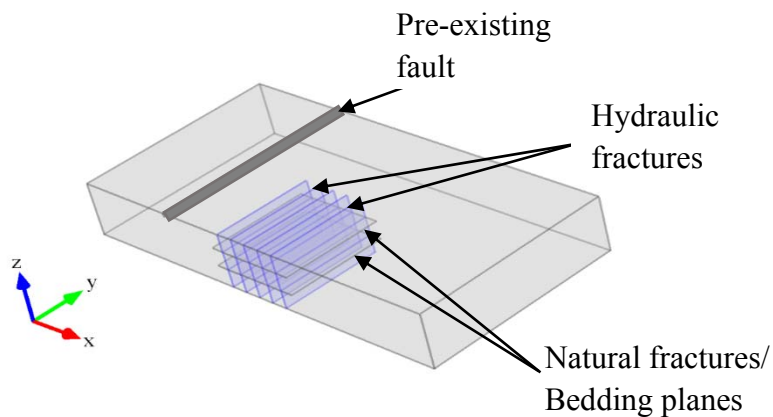
Figure 4.22   Model geometry showing pre-existing fault in the formation boundary

The simulations are conducted using the no- flux boundary conditions as a base case. Conceptual models that simulate the production of gas from shale formations assume that the reservoir is a closed system. In reality however, the shale formation is connected to other formations and a continuity boundary condition represents the appropriate physics at the point of intersection of the different formations. In the case where a fault serves as the link between the shale formation and an outside formation, continuity is enforced at the fracture edge by incorporating the pressure changes associated with time obtained from the base case scenario. **Table 4.4** presents the properties of the fault utilized in addition to the previously given parameters from the naturally fractured case study. The fault is located along the yz-plane and its conductive properties are assumed to be the same as that of the natural fractures.

Table 4.4   Fault Properties

Parameter	Value	Units
Fault porosity	25	%
Fault width	1000	ft
Boundary where fault is located	Top Boundary	
Depth of fault into formation	20	ft
Distance of fault from model centroid	500	ft
Fault permeability	1.0×10^2	mD

A description of the pattern of fluid movement into the plane in the formation that contains the fault (i.e yz-plane at x=500ft) during different simulation time periods is presented in **Figures 4.23**. Increased flow activity is observed into the vicinity of the fault over the course of the simulation. An estimate of flux over the fault formation is calculated and the results presented in Figure **4.24.**

110
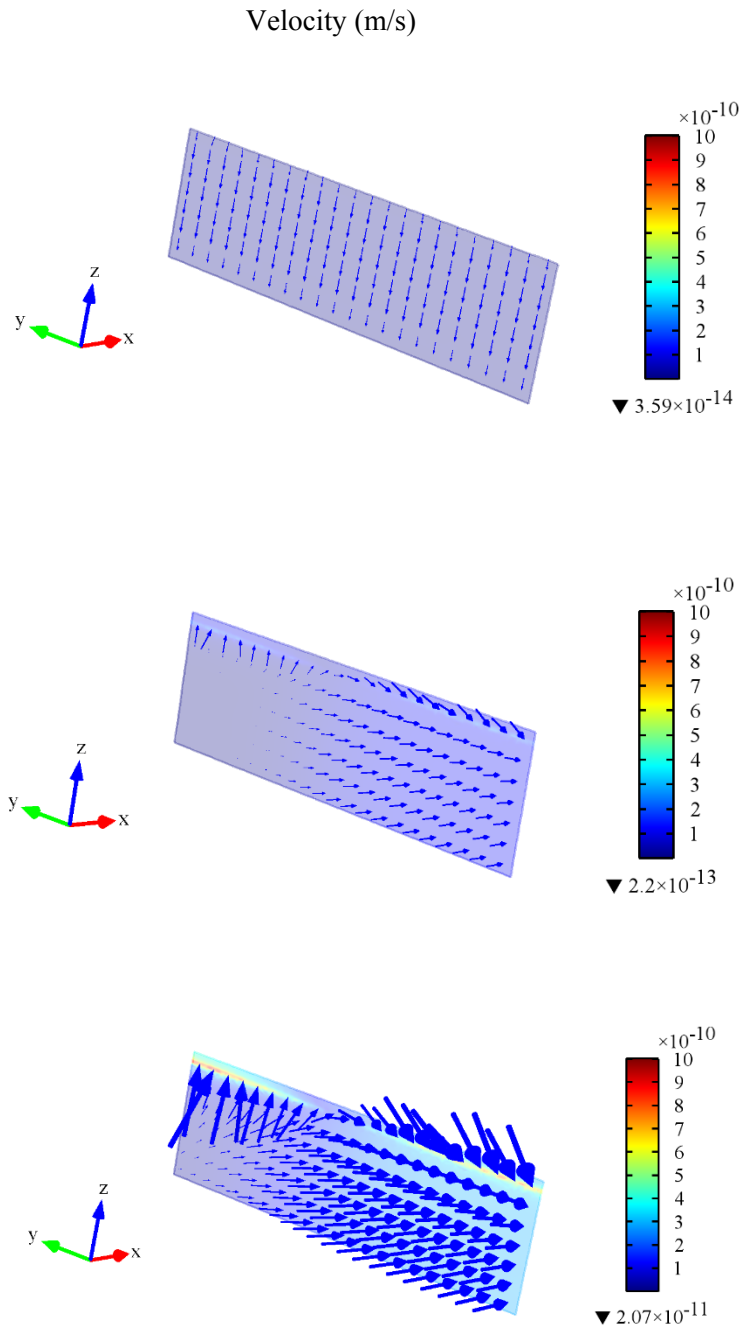
Velocity (m/s)

Figure 4.23   Fluid flow directions into the fault plane- x=500ft at (a) 1 month, (b) 1 year and (c) 10 years respectively. The surface plots show the magnitude of velocity in the fractures while the arrow lengths are indicative of the velocities in the formation.
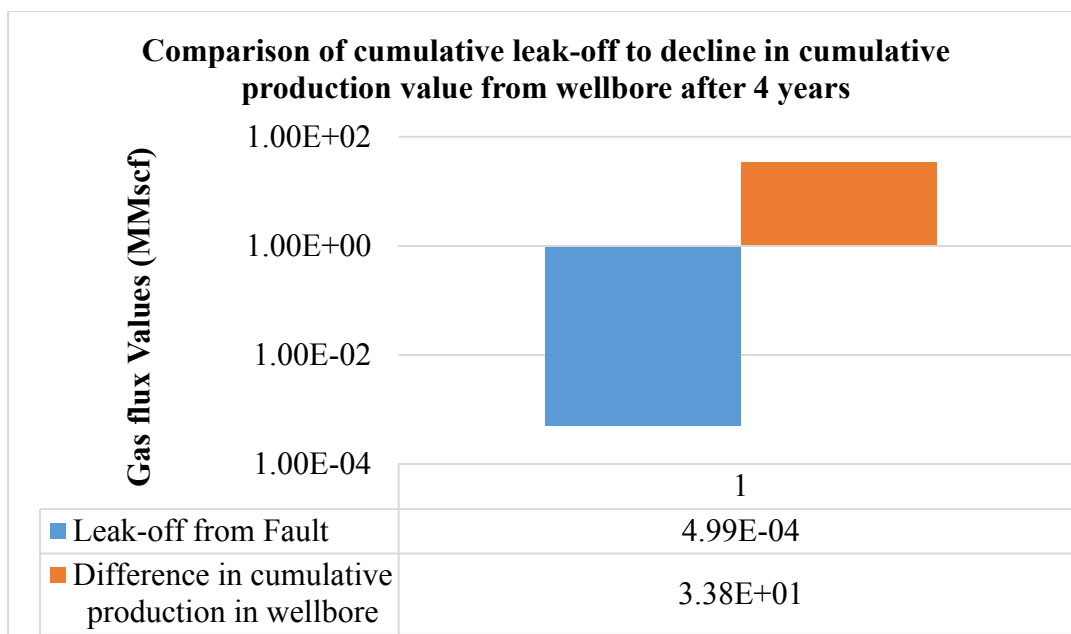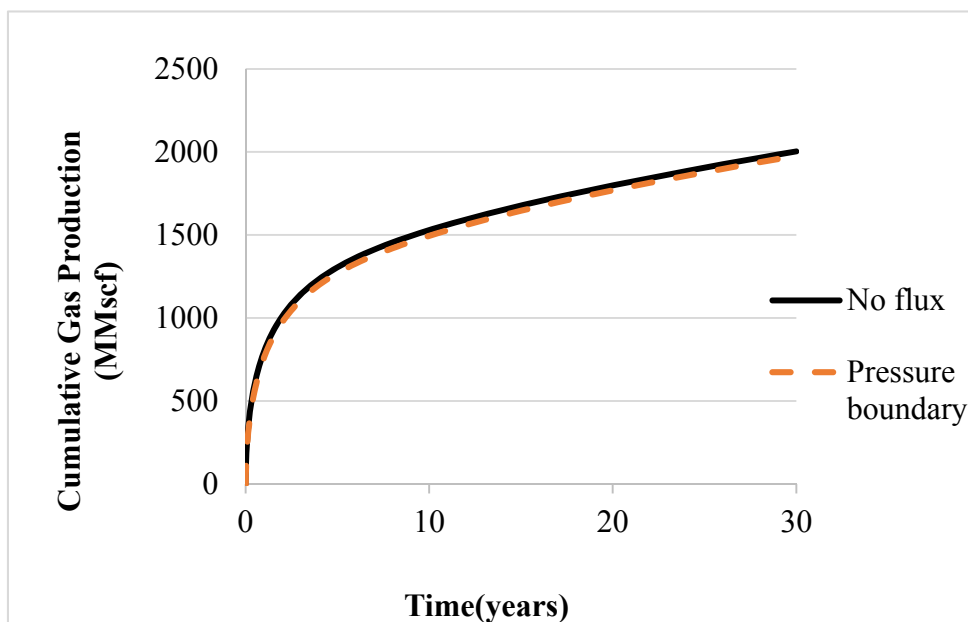
Figure 4.24 (a) Cumulative production values in the simulated model, utilizing a no flux boundary condition and a pressure boundary condition respectively at the fault boundary. **(b)** Comparison of cumulative leak off from fault boundary to decline in wellbore production after a 4 year period

From **Figure 4.24(a)**, we observe that the boundary condition seems to have no apparent effect on the cumulative production values of gas produced from the wellbore for the model simulated. Also in **Figure 4.24(b)**, an estimate of the gas flux through the fault boundary is compared to the calculated difference in the wellbore recovery rate from the closed boundary simulation case. While the leak-off value at the fault boundary after a 4 year simulation period is relatively low (500 ft^3 – 0.0004%) compared to the production from the wellbore, it represents a significant amount of gas that has the potential of moving into other regions in the subsurface. To ascertain that this leak-off stream does not travel into overlying formations and become a contaminant source in gas production areas, a sensitivity analysis of the flux leaving the computational domain through the fault to the fault parameters is carried out.

4.6   Sensitivity Analysis of Model Parameters

In the next set of simulations, an estimate of the sensitivity of the model results to the fracture, fault and formation parameters is evaluated. These tests are required in order to provide insight into the impacts of uncertainties on shale gas production values, as well as the possible leak off values from the fault at the boundary. For each parameter of interest, the base case value and the range of variations that are considered are presented in **Table 4.5** below. The simulated model geometry is as described in section 4.5 above.

Table 4.5   Parameter Values used for Sensitivity Analysis

Parameter	Value	Range
Formation Properties		
Well-bore pressure (psi)	1000	500 - 1500
Formation permeability (mD)	1e-4	1e2 – 1e-6
Fracture Properties		
Hydraulic fracture half-length (ft)	500	357 - 833
Hydraulic fracture permeability (mD)	5.0×10^3	500, 5000, 50000
Hydraulic fracture orientation to wellbore (degrees)	90	30, 60, 90
Number of fractures	5	3-7
Fracture spacing (ft)	80	60 - 100
Fracture Aperture (ft)	0.02	0.02, 0.2, 2
Natural fracture permeability (mD)	1e2	1e-2, 1, 1e2
Number of natural fracture bedding planes	2	2,4,6
Fault Properties		
Fault orientation to horizontal (degrees)	90	30, 60, 90
Depth of fault into shale formation (ft)	20	20, 40, 60

4.6.1. Sensitivity to Formation Properties

The results of the sensitivity study of the impacts of the wellbore pressure and the formation

permeability are presented in **Figure 4.24** and **Figures 4.25** respectively. We observe that for a

50% change in the wellbore pressure, a corresponding 17% change in the cumulative production

value at the wellbore is observed. Also, comparing the leak-off values from the fault boundary for

the three cases show that flux out of the fault boundary increases with increased operating pressure at the wellbore.
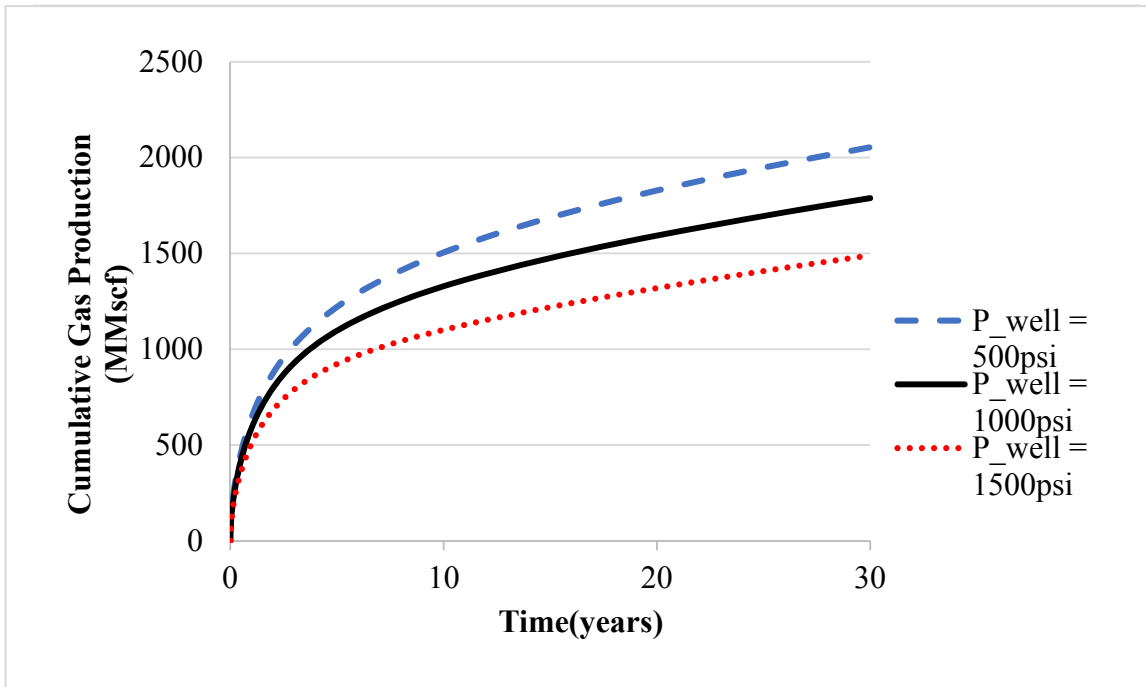
Figure 4.25 **(a)** Cumulative production values for simulation at different wellbore pressures
(b) Cumulative leak off from fault boundary after a 30 year period

While a reverse correlation is noted for the relationship between the cumulative production and wellbore pressure, a direct relationship is observed between the matrix permeability and the

amount of gas produced in the formation. Increased matrix permeability values lead to a corresponding increase in the amount of gas recovered at the wellbore. A decrease of 17.6% is observed in the cumulative production for a 50% decrease in the formation permeability and a 13% increase is associated with a 50% increase in the formation permeability.
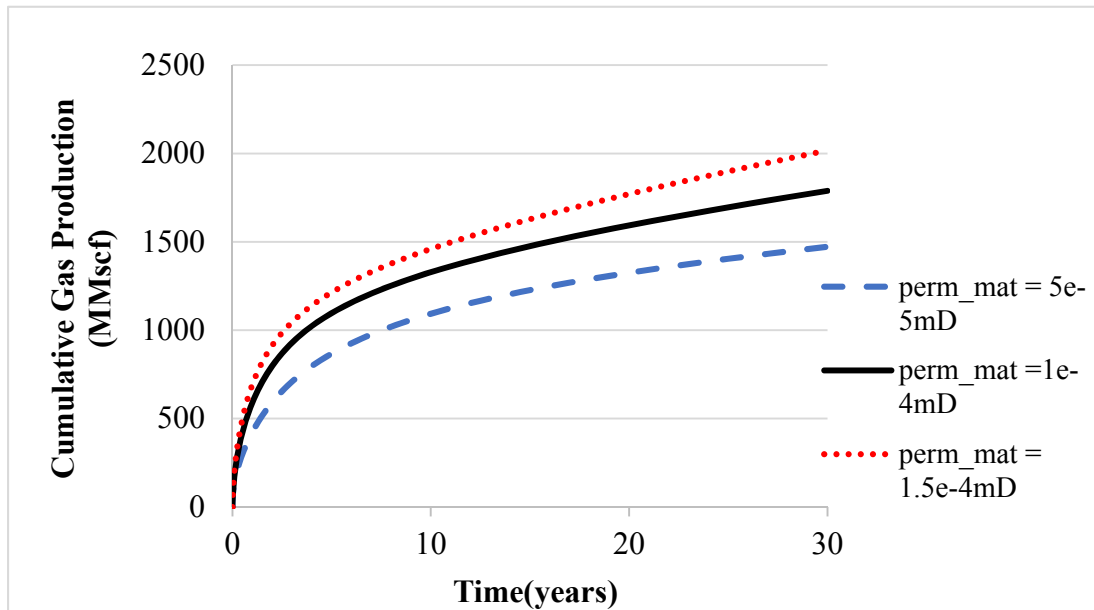
Figure 4.26 **(a)** Cumulative production values for simulation at different formation permeabilities.

The leak-off dependence on matrix parameters is as observed for the parametric study for wellbore pressure. A higher production rate at the wellbore is indicative of lower leak off and vice versa. In **Figure 4.26(b),** the cumulative leak off value from the fault boundary after a 30 year period is presented.
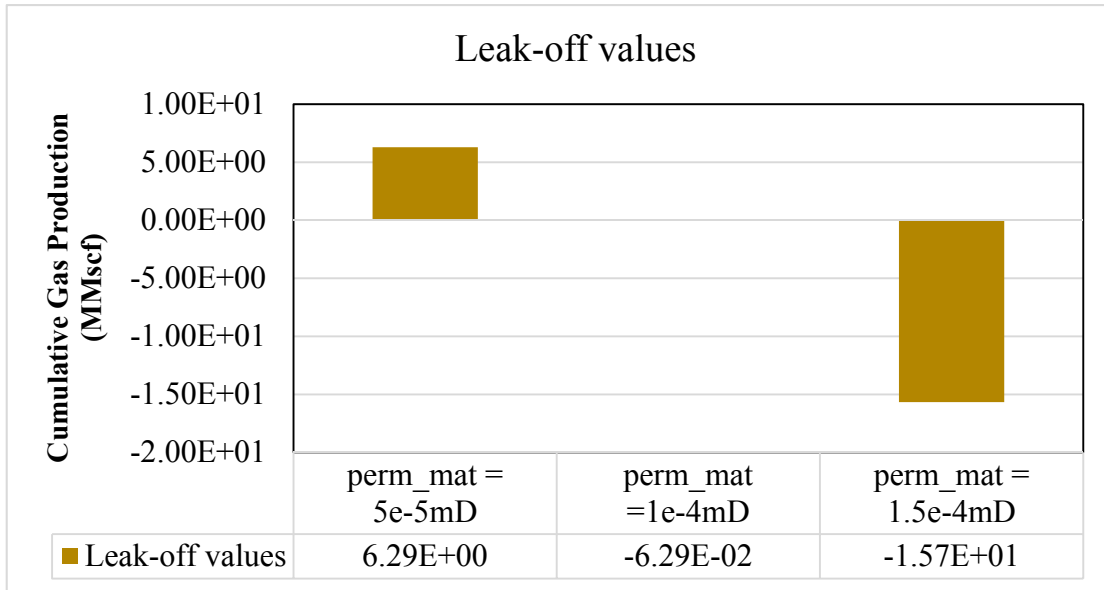
Figure 4.26 **(b)** Cumulative leak off from fault boundary after a 30 year period at different formation permeabilities

4.6.2. Sensitivity to Fracture Properties

A comparison of the model response to change in the hydraulic fracture parameters is presented. In **Figure 4.27**, the sensitivity of the system to the change in hydraulic fracture permeability is presented. It is observed that changing the fracture aperture by a factor of 100 only effects a 2% change on the cumulative production values from the formation.
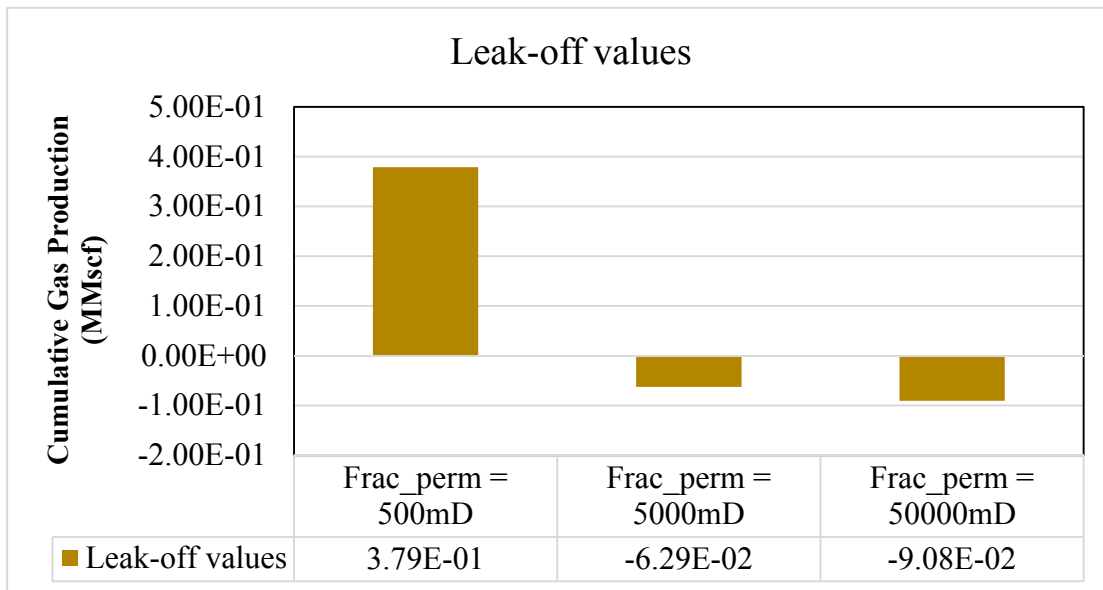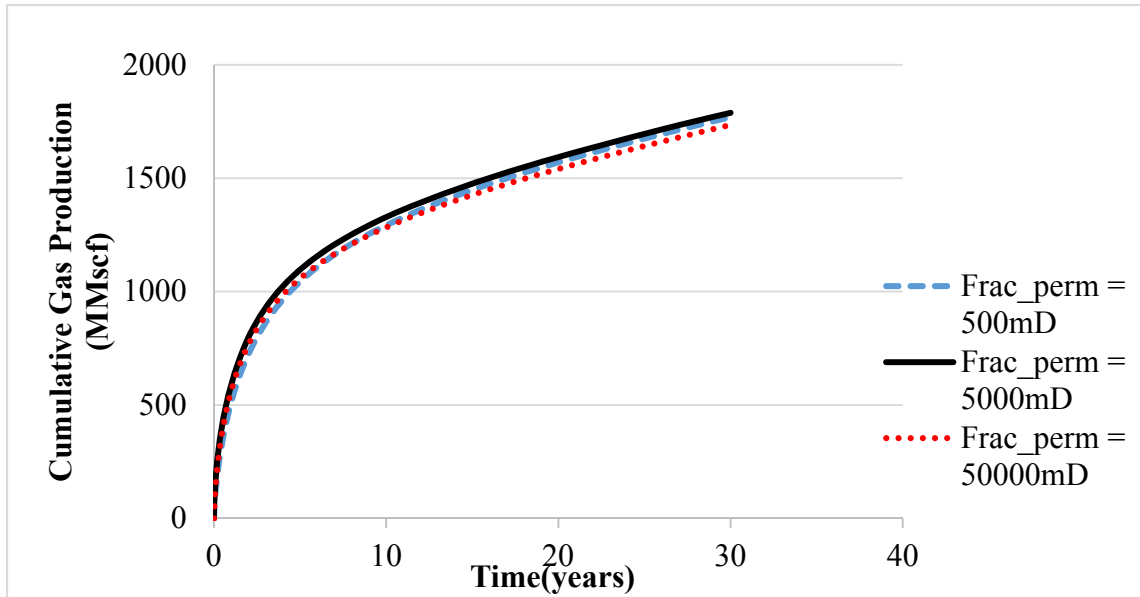
Figure 4.27   **(a)** Cumulative production from simulation study using different fracture permeabilities. (b) Cumulative leak off from fault boundary after a 30 year production period.

Figure 4.28 presents the response of the model to changes in fracture spacing. At the end

of the 30 year study period, an analysis of cumulative production values show that a 25% increase

118

in the size of the fracture spacing leads to a 13% increase in the cumulative production values, while a similar decrease leads to a 14% decrease in the total well recovery for the modeled system.

	Frac_Spac = 60ft	Frac_Spac = 80ft	Frac_Spac = 100ft
Leak-off values	4.25E+00	-6.29E-02	-5.95E+00
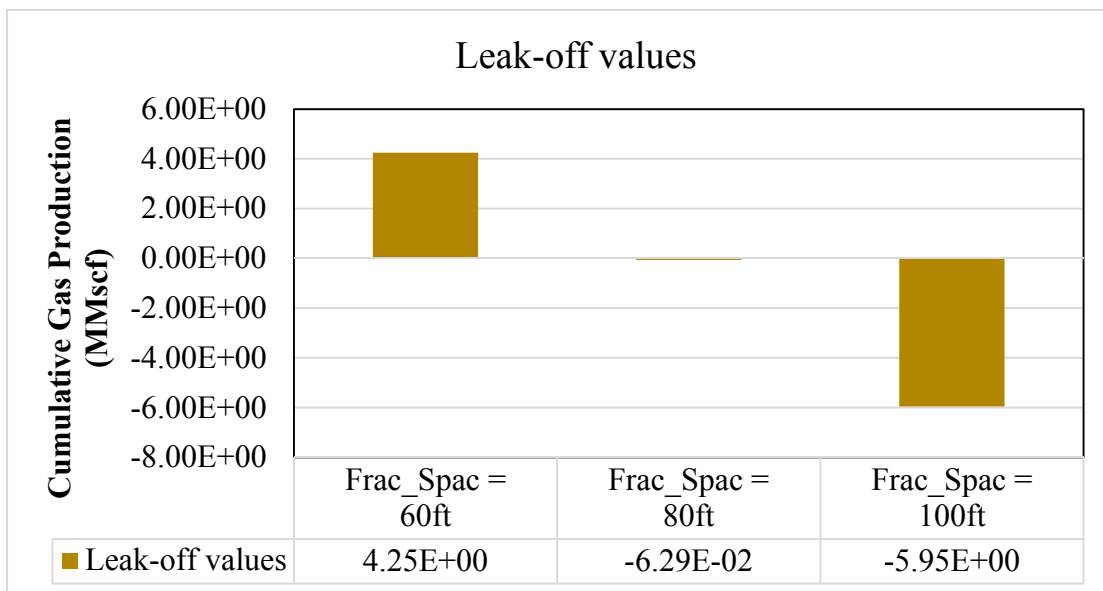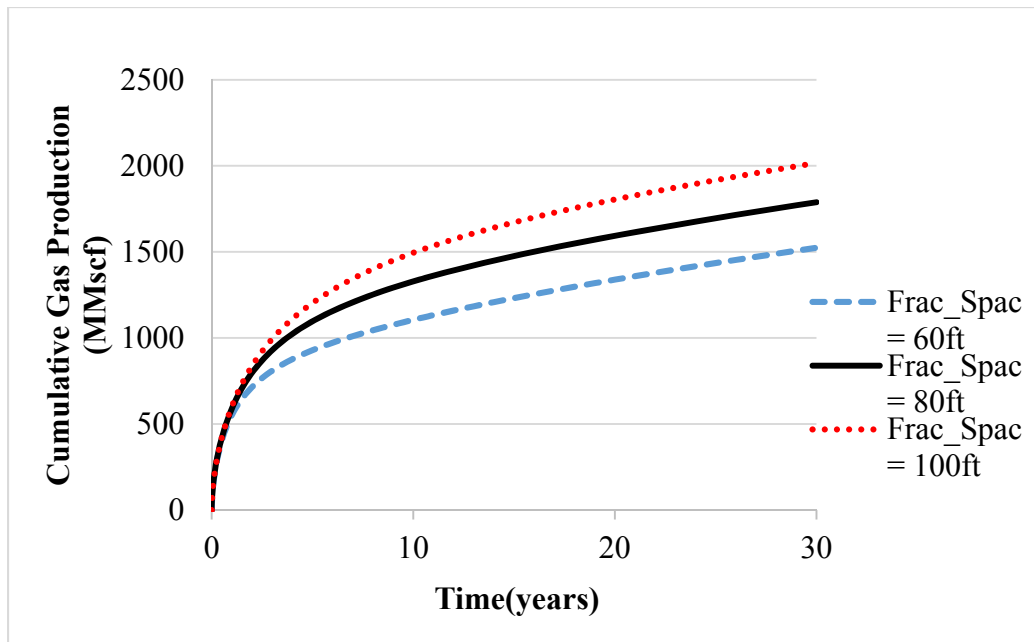
Figure 4.28   (a) Cumulative production from simulation study using different fracture spacing.
(b) Cumulative leak off from fault boundary after a 30 year production period.

This decreased production in the wellbore at lower fracture spacing values can be attributed to the effect of interference in the stimulated zone. Also a decrease in the leak off value is observed with increasing fracture spacing.

A study of the effect of inclination of hydraulic fracture to the wellbore is presented in **Figure 4.29**. By comparing the cumulative production values from the parametric study to that of the base case scenario (i.e., HF_Rot = 90), a 7% decrease in total production value was observed for the 60 degrees inclination angle case, and a 27% decrease observed for the case with the 30 degrees inclination angle. These results imply that fracture orientation relative to the wellbore is an important parameter required for accurate forecasting of production from fractured formations.

Values of leak-off can also be observed to increase with increasing acuteness of the angle between
the wellbore and the fractures.
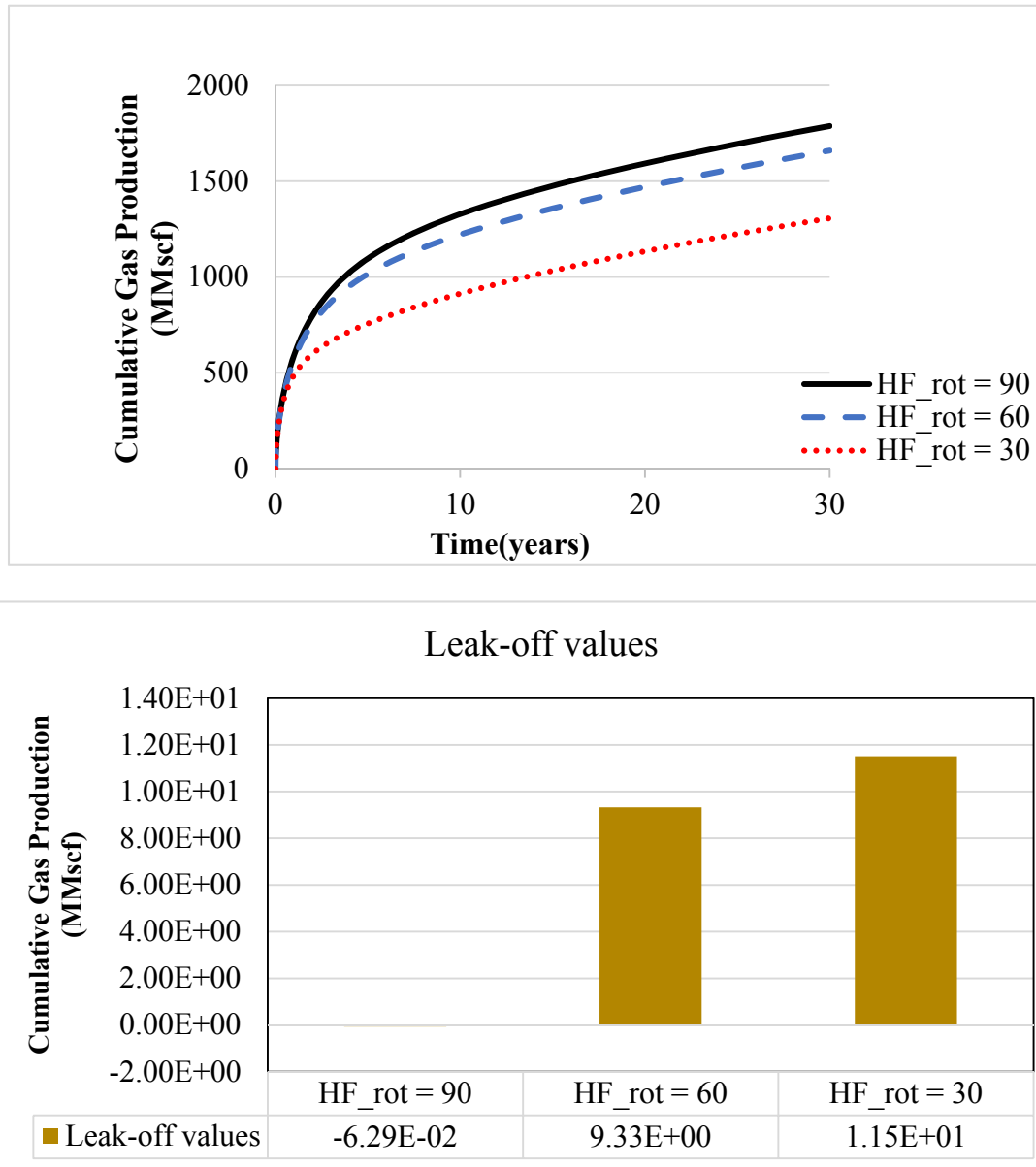
Figure 4.29   (a) Cumulative production from simulation study using different fracture
orientations to the wellbore (b) Cumulative leak off from fault boundary after a 30
year production period.

Figures 4.30 and 4.31 present the response of the model to changes in fracture length and fracture aperture respectively. It is observed that an increase in fracture length directly increases the cumulative production over the simulation period, while the results observed from utilizing a 100-fold increase in the aperture size does not significantly affect the recovery at the wellbore.
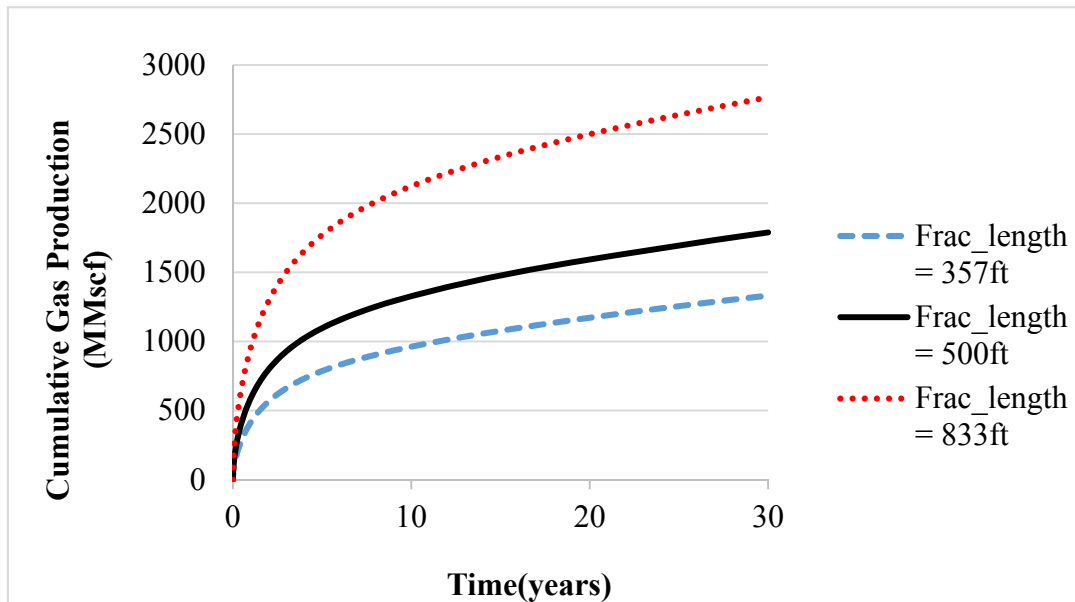
Figure 4.30   Cumulative production from simulation study using different fracture lengths.
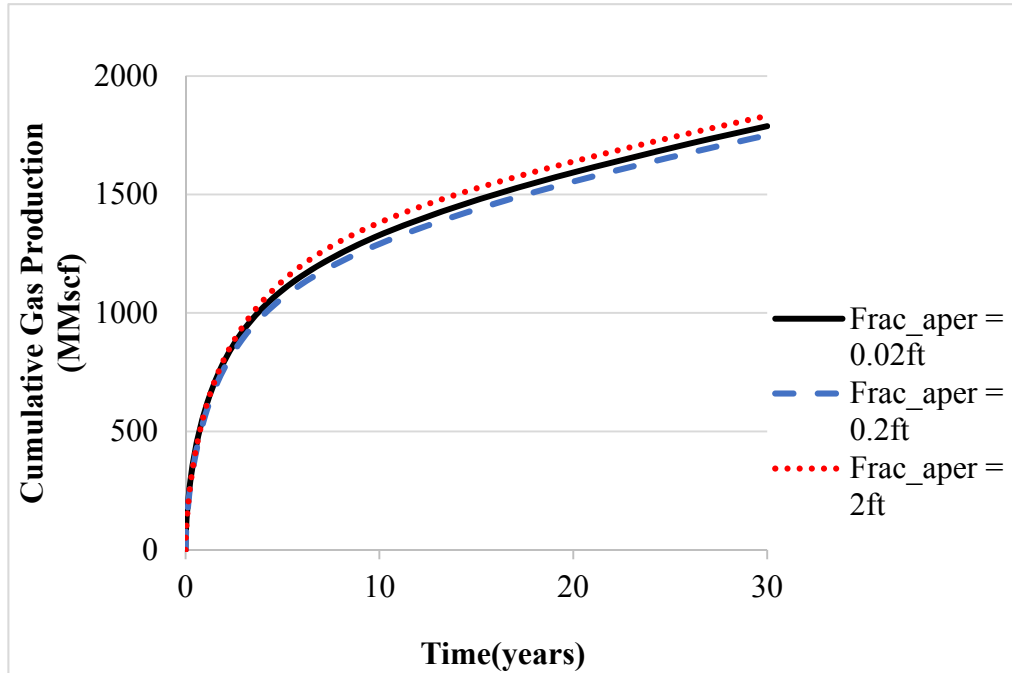
Figure 4.31   Cumulative production from simulation study using different fracture apertures

In Section 4.4. 1, the effect of natural fractures on production values from the wellbore was discussed. In **Figures 4.32** and **4.33**, the effects of the number of bedding plane layers and the permeability of the natural fracture are evaluated.

From **Figure 4.32**, a 12% increase in total production at the wellbore can be observed at the end of the simulation period as a result of the introduction of two natural fractures into the formation. Adding two more natural fractures led to a further 7% increase in cumulative production. However when six natural fractures are present in the formation, the effect of the increased surface area no longer affects the cumulative production, suggesting impacts of flow regime interference. In contrast, for **Figure 4.33,** an increase in the permeability of the natural fractures did not have any effect on the cumulative production at the end of the simulation period.
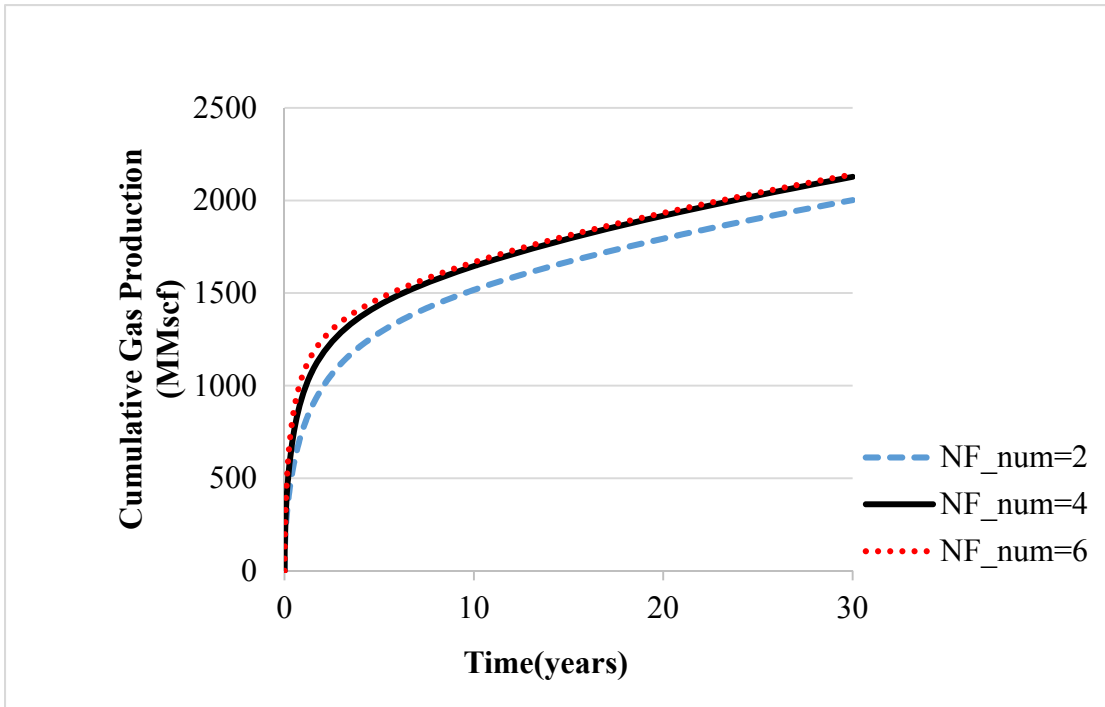
Figure 4.32   Cumulative production from simulation study using different number of natural fractures.
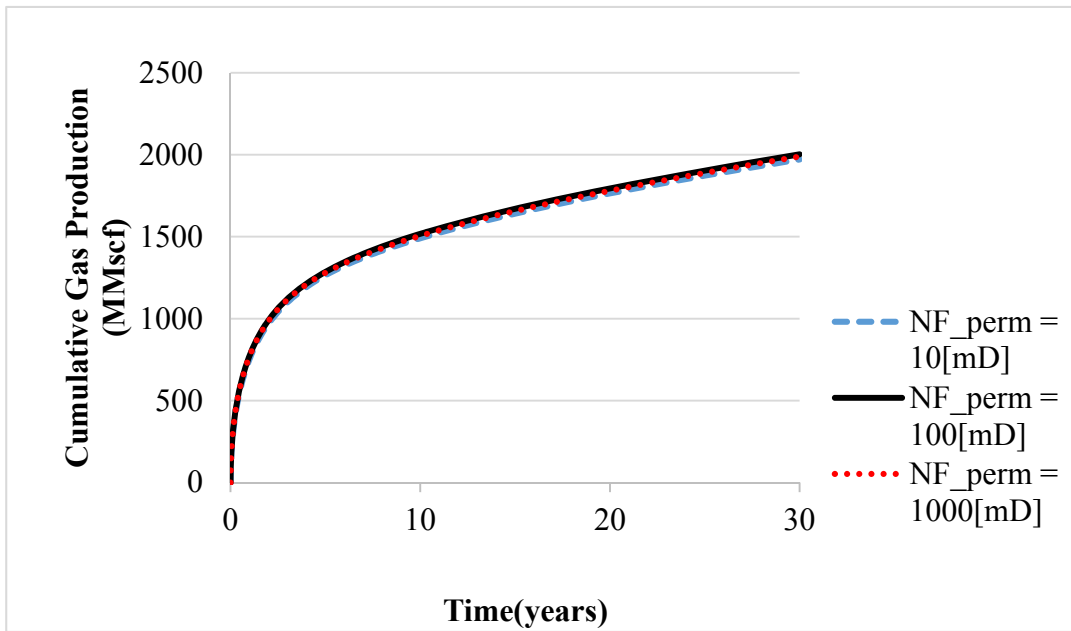
Figure 4.33   Cumulative production from simulation study using different natural fracture permeabilities.

4.6.3. Sensitivity to Fault Properties

An evaluation of the model response to changes in the parameters of the fault is presented. In **Figures 4.34**, the sensitivity of the system to the change in fault orientation is presented. While it can be observed that the fault orientation does not affect the wellbore production, the amount of fluid that moves across the fault boundary is dependent on the fault orientation. There is increased movement into the plane of the fault at lower angles of inclination to the horizontal as shown in **Figure 4.34(b).**
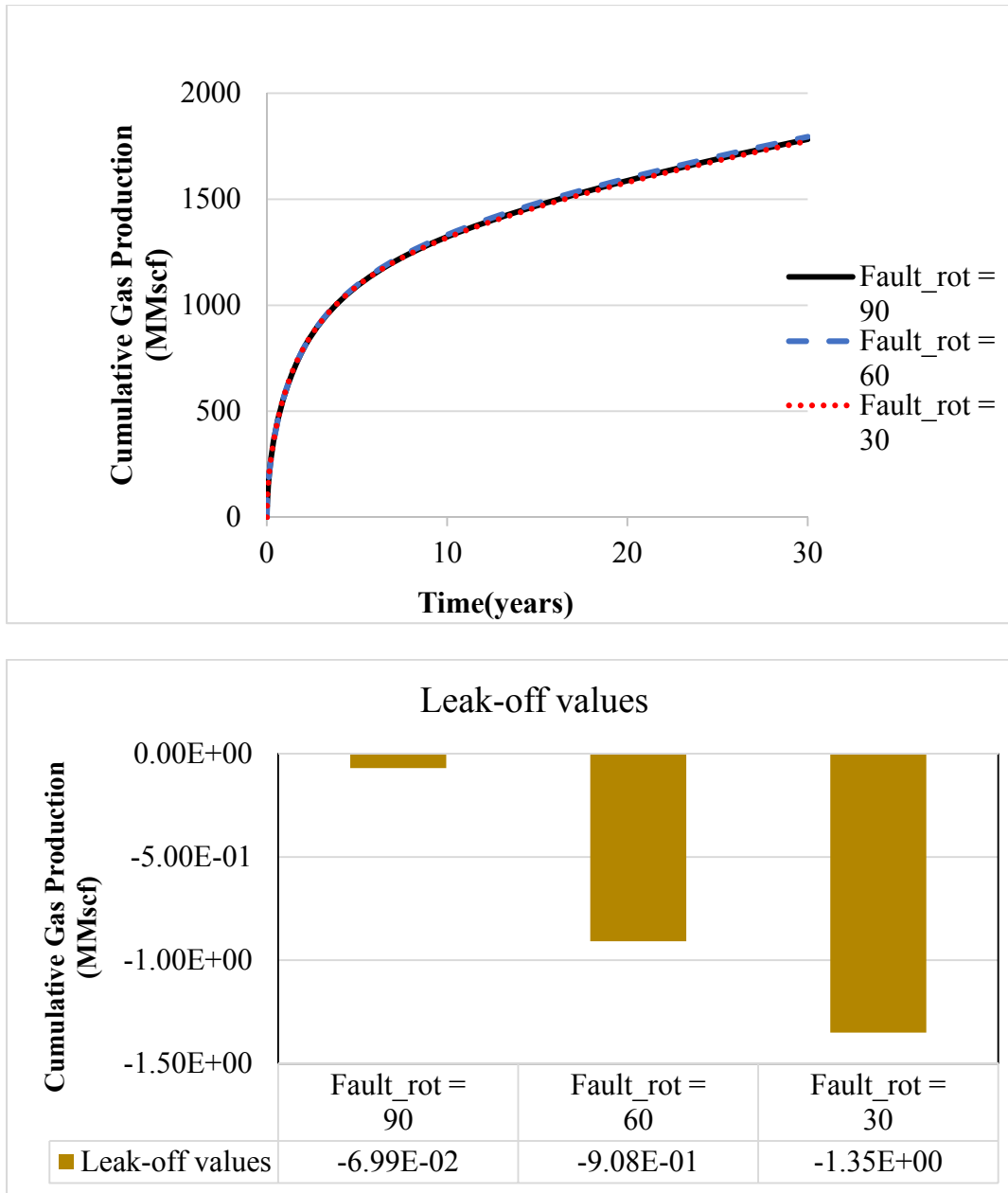
Figure 4.34 (a) Cumulative production from simulation study using different fault orientations. (b) Cumulative leak off from fault boundary after a 30 year production period.

Figure 4.35 presents the response of the model to changes in the depth of the fault in the formation. The observed response is similar to the model response to fault orientations.
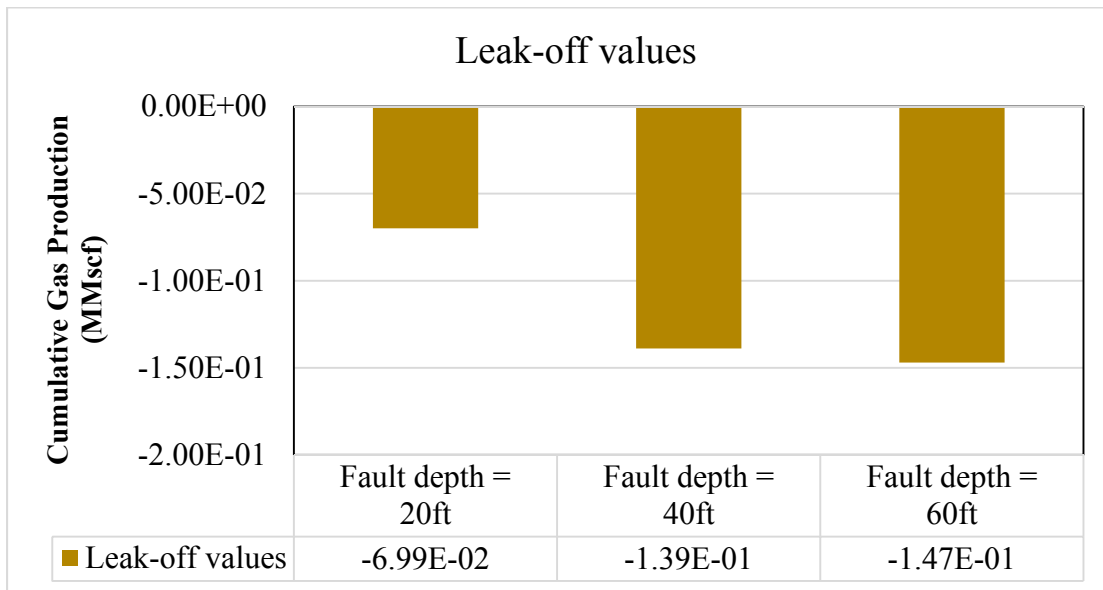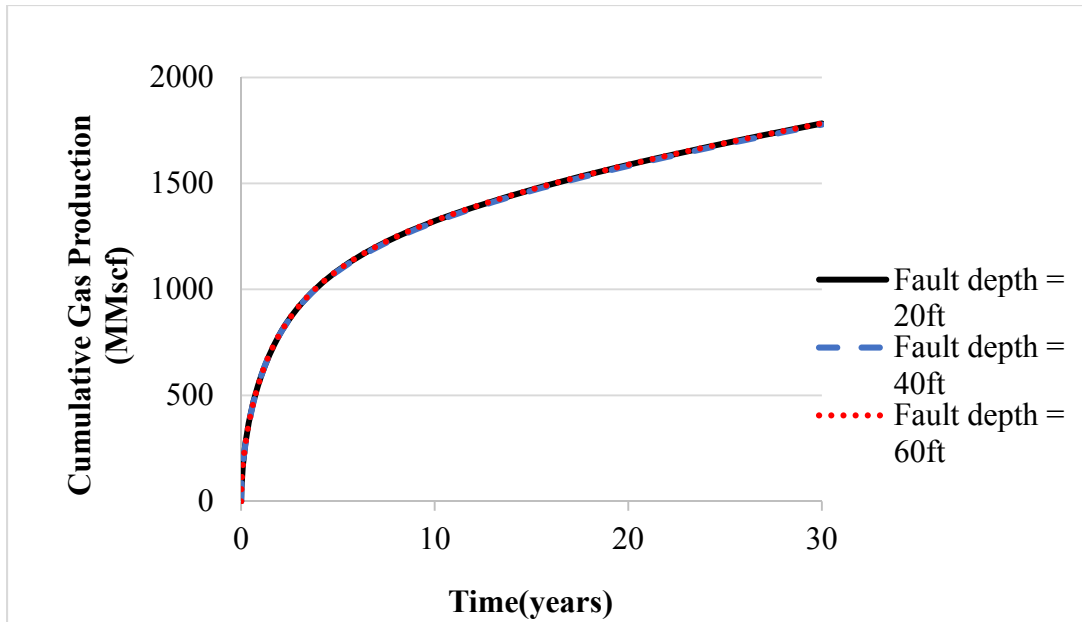
Figure 4.35   (a) Cumulative production from simulation study using different fault depths
(b) Cumulative leak off from fault boundary after a 30 year production period.

For all range of parameters studied, the response of the leak-off at the fault boundary was most sensitive to the orientation of the fractures to the wellbore, while production in the wellbore was most sensitive to the change in the length of the hydraulic fractures.

CHAPTER 5

CONCLUSIONS AND RECOMMENDATIONS

5.1   Conclusions

Migration patterns of gas present in fractured shale formations is addressed in this work, based on two conceptual models. While current approaches to modeling of fractured domains require a fully explicit representation of the fracture in order to obtain accurate description of the dynamics of fluid movement in hydraulically fractured formations, this work develops and makes use of two new conceptual models that bypass the need for explicit fracture grids. The semi-explicit conceptual model that is adopted in this work, makes use of a reduced dimensionality formulation to represent the hydraulic fractures and natural fractures present in the formation. This conceptual model enables faster simulation times and less computational requirements for situations in which the fracture can be hypothesized using the bi-wing description. The model results are validated by comparing against results obtained using a commercial fully explicit simulator.

The other noteworthy contribution of this research work to shale gas model development and an understanding of fractured shale formations, is its ability to handle complex fracture geometries. The use of asymmetrical fractal patterns to represent the secondary fractures around the hydraulically fractured region- has to my knowledge - so far not been implemented in literature. At best, currently available simulation models make use of the concept of a stimulated reservoir volume (SRV) where assignment of a bulk homogenous parameter to the area containing the complex fractures has been used.   In this work, a test of our developed algorithm for the representation of complex fracture networks as a non-homogenous porous medium, while still

128

preserving the conductive characteristics of the system is carried out by comparing it with the previously validated semi-explicit conceptual model.

At the end of the modeling study, the following conclusions were reached:

i. There is need for an accounting of the distinct fracture systems that are present in a fractured formation for accurate prediction of production values and flow patterns arising in the formation.

ii. The semi-explicit model representation of planar fractures is able to provide accurate results when used to simulate planar hydraulic fractures. By reducing the dimensionality of the fracture domain, the approach reduces the computational requirements associated with the fully explicit modeling of shale formations.

iii. Modeling of complex fracture networks is possible using the developed upscaling algorithm. The accuracy of the simulated results from these technique is however dependent on the number of subdomains that are used to resolve the model domain.

iv. The logarithmically spaced subdomain gridding technique enables a better preservation of fracture characteristics and gives well resolved property values compared to the regular gridding technique.

v. Stimulated reservoir volume overlap, which in our case occurs by capturing the physics of flow through the induced fracture networks surrounding the hydraulic fractures can lead to reduced production in fracture systems over time, particularly as the effects of fracture interference become pronounced in the system.

vi. Visualization of flow patterns in the fractured formation by use of arrow plots representing information about the velocity of fluids in the formation offers more information than the pressure transient analysis or even production rate analysis techniques available in literature.

The range of physical conditions that favor the direction of fluid flux towards the wellbore is also addressed. From the observed simulation results, it can be concluded that:

i. The natural fractures simulated in the formation enhance gas production rates from the wellbore at early times (t<1 year). After this period, the production rate becomes equivalent to the scenario without natural fractures.

ii. For most of the studied parameters, physical conditions that lead to an enhancement in the gas production rates from the formation, reduce the flux rates observed at the fault boundary and thereby decrease the probability of fluid escape into the overlying formation.

iii. Optimum gas flux can be obtained from the production stage by the use of long lateral fractures and ensuring that the fractures are placed orthogonal to the wellbore at a fracture spacing that limits the effect of interference in the stimulated zone.

5.2   Recommendations

This work attempts to represent the physical subsurface system as realistically as possible, however due to the uncertainties associated with obtaining accurate subsurface data, it is imperative to mention that the accuracy of the model does not necessarily mean that the physical

representation is correct, it just means that the model can produce accurate solutions for the parameters that have been specified. With this in mind, the following recommendations are made for the purpose of advancing knowledge associated with shale flow modeling efforts:

i. Reservoir characterization studies should be carried out, in order to enable the compilation of validation data for the complex geometry of the induced fractures around the wellbore, as it can be observed that these geometries have a significant impact on production performance.

ii. The visualization utility of the reservoir simulation code employed, enhances the understanding of the movement in the fractured formation and should be incorporated into other standard fractured shale gas reservoir simulators.

iii. The inherent non-linearities associated with flow in a distributed permeability system, represent a challenge to the validation of the solutions obtained using the upscaling technique. An attempt to resolve this issue, by making use of swept meshing techniques is explored in this work. However, there is still need for further study into meshing techniques that will enable model convergence in these systems.

iv. The model has been developed based on the assumption of the gas being present as a single phase in the shale formation. In reality however, shale formations usually possess water and in some cases, fracturing fluids. A model that extends the multi-phase interaction in the formation will therefore be beneficial to the shale model development industry and the oil and gas production industry at large.

v.   The effect of geomechanics on the permeability of the fractures also needs to be considered in subsequent studies, in order to get a better characterization of the change in fracture properties with time and stress systems in the subsurface.

REFERENCES

Abass, H. H., S. Hedayati, and D. L. Meadows, 1996, Nonplanar Fracture Propagation from a Horizontal Wellbore: Experimental Study: SPE-24823-PA, doi:10.2118/24823-PA.

ALL Consulting, 2012, The Modern Practices of Hydraulic Fracturing: A Focus on Canadian Resources, Petroleum Technology Alliance Canada & Science and Community Environmental Knowledge Fund.

Almulhim, A., 2014, Fluid Flow Modeling in Multi-Stage Hydraulic Fracturing Patterns for Production Optimization in Shale Reservoirs, Master's Thesis: Colorado School of Mines, 107 p.

Anderson, D. M., M. Nobakht, S. Moghadam, and L. Mattar, 2010, Analysis of Production Data from Fractured Shale Gas Wells, *in* SPE-131787-MS, SPE: Society of Petroleum Engineers, doi:10.2118/131787-MS.

Andersson, J., and B. Dverstorp, 1987, Conditional Simulations of Fluid Flow in Three-Dimensional Networks of Discrete Fractures: Water Resources Research, v. 23, no. 10, p. 1876–1886, doi:10.1029/WR023i010p01876.

Arthur, J. D., B. Bohm, and M. Layne, 2008, Hydraulic Fracturing Considerations for Natural Gas Wells of the Marcellus Shale, *in* Groundwater Protection Council Annual Forum. Cincinnati.

Barenblatt, G. I., I. P. Zheltov, and I. N. Kochina, 1960, Basic Concepts in the Theory of Seepage of Homogeneous Liquids in Fissured Rocks [Strata]: Journal of Applied Mathematics and Mechanics, v. 24, no. 5, p. 1286–1303.

Bennet, L. et al., 2005, The Source for Hydraulic Fracture Characterization: Oilfield Review, no. 1, p. 42–57.

Carter, B. J., J. Desroches, A. R. Ingraffea, and P. A. Wawrzynek, 2000, Simulating fully 3D hydraulic fracturing: Modeling in geomechanics, p. 525–557.

Chen, Z., G. Huan, and Y. Ma, 2006, 12. Flows in Fractured Porous Media, *in* Computational Methods for Multiphase Flows in Porous Media: Society for Industrial and Applied Mathematics, Computational Science & Engineering, p. 433–443.

Center for Engineered Fracturing of Rock(CEFoR), 2012, The three classical models of hydraulic fractures: KGD (plane strain), PKN and radial. Mechanics of Hydraulic Fractures:, http://www.cefor.umn.edu/mechanics-of-hydraulic-fractures/accessed 04/13/2015

Chianelli, R. R., X. C. Kretschmer, and S. A. Holditch, 2011, Petroleum and Natural Gas, *in* Fundamentals of Materials for Energy and Environmental Sustainability: Cambridge University Press.

Chiles, J. P., and G. de Marsily, 1993, Stochastic Models of Fracture Systems and Their Use in Flow and Transport Modeling, *in* Flow and Contaminant Transport in Fractured Rock: Academic Press, p. 169–231.

Cipolla, C., E. Lolon, J. Erdle, and B. Rubin, 2009, Reservoir Modeling in Shale-Gas Reservoirs, *in* Proceedings of the SPE Eastern Regional Meeting, Charleston, West Virginia: Society of Petroleum Engineers, p. 19.

Clark, C., A. Burnham, C. Harto, and R. Horner, 2012, Hydraulic Fracturing and Shale Gas Production: Technology, Impacts, and Policy: Argonne National Laboratory.

Cornell, D., and D. L. Katz, 1953, Flow of Gases through Consolidated Porous Media: Industrial & Engineering Chemistry, v. 45, no. 10, p. 2145–2152, doi:10.1021/ie50526a021.

Curtis, J. B., 2002, Fractured Shale-Gas Systems: AAPG bulletin, v. 86, no. 11, p. 1921–1938.

Dershowitz, W., and T. W. Doe, 2011, Modeling Complexities of Natural Fracturing Key in Gas Shales: The American Oil and Gas Reporter, v. Hydraulic Fracturing Technology.

Dershowitz, W. S., and H. H. Einstein, 1988, Characterizing Rock Joint Geometry with Joint System Models: Rock Mechanics and Rock Engineering, v. 21, no. 1, p. 21–51, doi:10.1007/BF01019674.

Dershowitz, W. S., P. R. La Pointe, and T. W. Doe, 2004, Advances in Discrete Fracture Network Modeling, *in* Proceedings of the US EPA/NGWA Fractured Rock Conference, Portland: p. 882–894.

Ding, D., Y.-S. Wu, N. Farah, C. Wang, and B. Bourbiaux, 2014, Numerical Simulation of Low Permeability Unconventional Gas Reservoirs, *in* Proceedings of the SPE/EAGE European Unconventional Conference, Vienna, Austria: Society of Petroleum Engineers, p. 30.

Diodato, D. M., 1994, A Compendium of Fracture Flow models: Work sponsored by US Department of Defense, United States Army, Europe, Combat Maneuver Training Center, Hohenfels, Germany.

Dong, G., 2010, Modeling Performance of Horizontal Wells with Multiple Fractures in Tight Gas Reservoirs: Texas A&M University.

Dong, C. Y., and C. J. de Pater, 2001, Numerical Implementation of Displacement Discontinuity Method and its Application in Hydraulic Fracturing: Computer Methods in Applied Mechanics and Engineering, v. 191, no. 8–10, p. 745–760, doi:10.1016/S0045-7825(01)00273-0.

Fisher, M. K., J. R. Heinze, C. D. Harris, B. M. Davidson, C. A. Wright, and K. P. Dunn, 2004, Optimizing Horizontal Completion Techniques in the Barnett Shale Using Microseismic Fracture Mapping, *in* SPE-90051-MS, SPE: Society of Petroleum Engineers, doi:10.2118/90051-MS.

Fisher, M. K., C. A. Wright, B. M. Davidson, A. K. Goodwin, E. O. Fielder, W. S. Buckler, and N. P. Steinsberger, 2002, Integrating Fracture Mapping Technologies to Optimize Stimulations in the Barnett Shale, *in* SPE-77441-MS, SPE: Society of Petroleum Engineers, doi:10.2118/77441-MS.

Foley, J. D., A. van Dam, S. K. Feiner, and J. F. Hughes, 1990, Computer Graphics: Principles and Practice: USA, Addison-Wesley Publishing Company, The Systems Programming Series, 1174 p.

Fox, A., P. Snelling, J. McKenna, C. Neale, C. Neuhaus, and J. Miskimmins, 2013, Geomechanical Principles for Unconventional Reservoirs: Microseismic, Inc.

Franca, L. P., and F.-N. Hwang, 2002, Refining the Submesh Strategy in the Two-level Finite Element Method: Application to the Advection–Diffusion Equation: International Journal for Numerical Methods in Fluids, v. 39, no. 2, p. 161–187, doi:10.1002/fld.219.

Frantz, J. H., and V. Jochen, 2005, Shale Gas: Schlumberger.

Freeman, T. T., R. J. Chalaturnyk, and I. I. Bogdanov, 2008, Fully Coupled Thermo-Hydro-Mechanical Modeling by COMSOL Multiphysics, with Applications in Reservoir Geomechanical Characterization, *in* Excerpt from the Proceeding of the COMSOL Conference.

Gale, J. F. W., R. M. Reed, and J. Holder, 2007, Natural Fractures in the Barnett Shale and their Importance for Hydraulic Fracture Treatments: AAPG Bulletin, v. 91, no. 4, p. 603–622, doi:10.1306/11010606061.

Gascoyne, M., and D. . Wuschke, 1997, Gas Migration through Water-Saturated, Fractured Rock: Results of a Gas Injection Test: Journal of Hydrology, v. 196, no. 1-4, p. 76–98.

Geertsma, J., and F. De Klerk, 1969, A Rapid Method of Predicting Width and Extent of Hydraulically Induced Fractures: SPE-2458-PA, doi:10.2118/2458-PA.

Gorocu, S., 2010, Optimization of the Design of Transverse Hydraulic Fractures in Horizontal Wells Placed in Dual Porosity Tight Gas Reservoirs, Master's Thesis: University Park, State College, PA, The Pennsylvania State University, 112 p.

Hardy, B., C. Corgnale, R. Chahine, M.-A. Richard, S. Garrison, D. Tamburello, D. Cossement, and D. Anton, 2012, Modeling of Adsorbent Based Hydrogen Storage Systems: International Journal of Hydrogen Energy, v. 37, no. 7, p. 5691–5705, doi:10.1016/j.ijhydene.2011.12.125.

Harpel, J., L. Barker, J. Fontenot, C. Carroll, S. Thomson, and K. Olson, 2012, Case History of the Fayetteville Shale Completions, *in* Proceedings of the SPE Hydraulic Fracturing Technology Conference, The Woodlands, Texas: Society of Petroleum Engineers.

Hossain, M. M., and M. K. Rahman, 2008, Numerical Simulation of Complex Fracture Growth during Tight Reservoir Stimulation by Hydraulic Fracturing: Journal of Petroleum Science and Engineering, v. 60, no. 2, p. 86–104, doi:10.1016/j.petrol.2007.05.007.

Al-Hussainy, R., H. J. Ramey, and P. B. Crawford, 1966, The Flow of Real Gases throgh Porous Media: Journal of Petroleum Technology, no. SPE 1248A, p. 624–636.

Huyakorn, P. S., B. H. Lester, and C. R. Faust, 1983, Finite element techniques for modeling groundwater flow in fractured aquifers: Water Resources Research, v. 19, no. 4, p. 1019–1035, doi:10.1029/WR019i004p01019.

Jacot, R. H., L. W. Bazan, and B. R. Meyer, 2010, Technology Integration: A Methodology To Enhance Production and Maximize Economics in Horizontal Marcellus Shale Wells, *in* SPE-135262-MS, SPE: Society of Petroleum Engineers, doi:10.2118/135262-MS.

Kalantari Dahaghi, A., and S. Mohaghegh, 2011, Numerical Simulation and Multiple Realizations for Sensitivity Study of Shale Gas Reservoirs, *in* SPE Production and Operations Symposium.

Karimi-Fard, M., B. Gong, and L. J. Durlofsky, 2006, Generation of Coarse-scale Continuum Flow Models from Detailed Fracture Characterizations: Continuum Flow Models of Fracture Systems: Water Resources Research, v. 42, no. 10, p. n/a–n/a, doi:10.1029/2006WR005015.

Keshavarzi, R., and R. Jahanbakhshi, 2013, Investigation of Hydraulic and Natural Fracture Interaction: Numerical Modeling or Artificial Intelligence?, *in* R. Jeffrey, ed., Effective and Sustainable Hydraulic Fracturing: InTech.

King, G. E., 2012, Hydraulic Fracturing 101: What Every Representative, Environmentalist, Regulator, Reporter, Investor, University Researcher, Neighbor and Engineer Should Know About Estimating Frac Risk and Improving Frac Performance in Unconventional Gas and Oil Wells, *in* SPE-152596-MS, SPE: Society of Petroleum Engineers, doi:10.2118/152596-MS.

King, G. ., 1990, Material Balance Techniques for Coal Seam and Devonian Shale gas Reservoirs, *in* New Orleans, LA, USA: Society of Petroleum Engineers Inc.

Kodituwakku, R., K. R. Wijeweera, and Chimakara M. A .P, 2012, An Efficient Line Clipping Algorithm for 3D Space: International Journal of Advanced Research in Computer Science and Software Engineering, v. 2, no. 5, p. 96–101.

Kundert, D. P., and M. J. Mullen, 2009, Proper Evaluation of Shale Gas Reservoirs Leads to a More Effective Hydraulic-Fracture Stimulation, *in* SPE-123586-MS, SPE: Society of Petroleum Engineers, doi:10.2118/123586-MS.

Lapcevic, P. A., K. S. Novakoski, and E. A. Sudicky, 1999, Groundwater Flow and Solute Transport in Fractured Media, *in* The Handbook of Groundwater Engineering: USA, CRC Press, Ch 17, p. 1–38.

Larsen, B., and A. Gudmundsson, 2010, Linking of Fractures in Layered Rocks: Implications for permeability: Tectonophysics, v. 492, no. 1-4, p. 108–120, doi:10.1016/j.tecto.2010.05.022.

Leahy-Dios, A., M. Das, A. Agarwal, and R. D. Kaminsky, 2011, Modeling of Transport Phenomena and Multicomponent Sorption for Shale Gas and Coalbed Methane in an Unstructured Grid Simulator, *in* Proceedings of the SPE Annual Technical Conference, SPE: Society of Petroleum Engineers.

Liang, Y.-D., and B. A. Barsky, 1984, A New Concept and Method for Line Clipping: ACM Transactions on Graphics (TOG), v. 3, no. 1, p. 1–22.

Li, C., R. Lafollette, A. Sookprasong, and S. Wang, 2013, Characterization of Hydraulic Fracture Geometry in Shale Gas Reservoirs Using Early Production Data, *in* Proceedings of the International Petroleum Technology Conference (IPTC).

Linkov, A., 2012, Numerical Modeling of Hydraulic Fractures: State of Art and New Results.

Li, L. C., C. A. Tang, G. Li, S. Y. Wang, Z. Z. Liang, and Y. B. Zhang, 2012, Numerical Simulation of 3D Hydraulic Fracturing Based on an Improved Flow-Stress-Damage Model and a Parallel FEM Technique: Rock Mechanics and Rock Engineering, v. 45, no. 5, p. 801–818, doi:10.1007/s00603-012-0252-z.

Mahrer, K. D., 1999, A Review and Perspective on Far-Field Hydraulic Fracture Geometry Studies: Journal of Petroleum Science and Engineering, v. 24, no. 1, p. 13–28, doi:10.1016/S0920-4105(99)00020-0.

Mason, J., 2012, Well Production Profiles for the Fayetteville Shale Gas Play Revisited: Oil and Gas Journal.

Mattar, L., B. Gault, K. Morad, C. R. Clarkson, C. M. Freeman, D. Ilk, and T. Blasingame, 2008, Production Analysis and Forecasting of Shale Gas Reservoirs: Case History-Based Approach, *in* SPE Shale Gas Production Conference: Society of Petroleum Engineers.

Mohaghegh, S. D., 2013, A Critical View of Current State of Reservoir Modeling of Shale Assets, *in* SPE Eastern Regional Meeting: Society of Petroleum Engineers.

Moridis, G. J., T. A. Blasingame, C. M. Freeman, and others, 2010, Analysis of mechanisms of flow in fractured tight-gas and shale-gas reservoirs, *in* SPE Latin American and Caribbean Petroleum Engineering Conference: Society of Petroleum Engineers.

Muskat, M., 1946, The Flow of Homogenous Fluids through Porous Media: Ann Arbor, Michigan.

National Research Council, 1996, Rock Fractures and Fluid Flow: Contemporary Understanding and Applications: Washington, DC, The National Academies Press.

Nelson, R. A., 2001, Geologic Analysis of Fractured Reservoirs: 352 p.

Nordgren, R. P., 1972, Propagation of a Vertical Hydraulic Fracture: SPE-3009-PA, doi:10.2118/3009-PA.

NPC, 2011, Hydraulic Fracturing: Technology and Practices addressing Hydraulic Fracturing and Completions: National Petroleum Council.

NRDC, 2002, Hydraulic Fracturing of Coalbed Methane Wells: A Threat to Drinking Water: National Resources Defence Council.

Nuclear Energy Agency, 1992, Gas Generation and Release from Radioactive Waste Repositories, *in* NEA/OECD Workshop, Paris, Frannce: p. 23–26.

Oda, M., 1985, Permeability Tensor for Discontinuous Rock Masses: Geotechnique, v. 35, no. 4, p. 483–495.

OECD/IEA, 2012, Golden Rules for a Golden Age of Gas, World Energy Outlook Special Report on Unconventional Gas.

Osholake, T., 2010, Factors Affecting Hydraulically Fractured Well Performance in the Marcellus Shale Gas Reservoirs, Master's Thesis: State Park, PA, The Pennsylvania State University, 99 p.

Painter, S., and V. Cvetkovic, 2005, Upscaling Discrete Fracture Network Simulations: An alternative to Continuum Transport Models.: Water Resources Research, v. 41, no. 2, p. n/a–n/a, doi:10.1029/2004WR003682.

Pandey, A., and S. Jain, 2013, Comparison of Various Line Clipping Algorithm for Improvement: International Journal of Modern Engineering Research, v. 3, no. 1, p. 69–74.

Pankow, J. F., R. L. Johnson, J. P. Hewetson, and J. A. Cherry, 1986, An evaluation of contaminant migration patterns at two waste disposal sites on fractured porous media in terms of the equivalent porous medium (EPM) model: Transport and Transformations of Organic Contaminants, v. 1, no. 1–2, p. 65–76, doi:10.1016/0169-7722(86)90007-0.

Parker, B. L., J. A. Cherry, and S. W. Chapman, 2012, Discrete Fracture Network Approach for Studying Contamination in Fractured Rock: AQUAMundi: Journal of Water Science, v. 60, p. 101–116.

Perkins, T. K., and L. R. Kern, 1961, Widths of Hydraulic Fractures: SPE-89-PA, doi:10.2118/89-PA.

Pinder, G. ., P. . Huyakorn, and E. A. Sudicky, 1993, Simulation of Flow and Transport in Fractured Porous Media, *in* Flow and Contaminant Transport in Fractured Rock: Academic Press, p. 395–435.

Powers, B., 2011, The Fayetteville Shale Peaks: <http://www.financialsense.com/contributors/bill-powers/2011/05/02/the-fayetteville-shale-peaks> (accessed January 21, 2014).

Pruess, K., 2001, Two-Phase Unsaturated Flow at Yucca Mountain, Nevada: A Report on Current Understanding: Geophysical Monograph, v. 42, no. 2, p. 113 −133.

Rahman, M. M., and M. K. Rahman, 2010, A Review of Hydraulic Fracture Models and Development of an Improved Pseudo-3D Model for Stimulating Tight Oil/Gas Sand.: Energy Sources Part A: Recovery, Utilization & Environmental Effects, v. 32, no. 15, p. 1416–1436.

Rahman, M. M., and S. S. Rahman, 2013, Studies of Hydraulic Fracture-Propagation Behavior in Presence of Natural Fractures: Fully Coupled Fractured-Reservoir Modeling in Poroelastic Environments: International Journal of Geomechanics, v. 13, no. 6, p. 809–826, doi:10.1061/(ASCE)GM.1943-5622.0000274.

Ramakrishnan, H., E. Peza, S. Sinha, M. Woods, C. Ikeocha, F. Mengel, Y. Simon, P. Pearce, J. Kiester, and S. Mcketta, 2011, Understanding and Predicting Fayetteville Shale Gas Production Through Integrated Seismic-to-Simulation Reservoir Characterization Workflow, *in* Proceedings of the SPE Annual Technical Conference and Exhibition, Denver, Colorado.

Rao, V., 2012, Shale gas: The Promise and the Peril: Research Triangle Park, NC, RTI Press.

Rexer, T. F. T., M. J. Benham, A. C. Aplin, and K. M. Thomas, 2013, Methane Adsorption on Shale under Simulated Geological Temperature and Pressure Conditions: Energy & Fuels, v. 27, no. 6, p. 3099–3109, doi:10.1021/ef400381v.

Le Roux, D. Y., A. Staniforth, and C. A. Lin, 1998, Finite Elements for Shallow-Water Equation Ocean Models: Monthly Weather Review, v. 126, no. 7, p. 1931–1951.

Rubin, B., 2010, Accurate Simulation of Non Darcy Flow in Stimulated Fractured Shale Reservoirs, *in* Proceedings of the SPE Western Regional Meeting, Anaheim, California: doi:10.2118/132093-MS.

Rushing, J. A., A. D. Perego, T. A. Blasingame, and others, 2008, Applicability of the Arps Rate-Time Relationships for Evaluating Decline Behavior and Ultimate Gas Recovery of Coalbed Methane Wells, *in* CIPC/SPE Gas Technology Symposium 2008 Joint Conference: Society of Petroleum Engineers.

Sarda, S., L. Jeannin, R. Basquet, and B. Bourbiaux, 2002, Hydraulic Characterization of Fractured Reservoirs: Simulation on Discrete Fracture Models: SPE-77300-PA, doi:10.2118/77300-PA.

Schepers, K. C., R. J. Gonzalez, G. J. Koperna, and A. Y. Oudinot, 2009, Reservoir Modeling in Support of Shale Gas Exploration, *in* SPE-123057-MS, SPE: Society of Petroleum Engineers, doi:10.2118/123057-MS.

Seto, C., 2011, Role of Technology in Unconventional Gas Resources, *in* The Future of Natural Gas, An Interdisciplinary MIT Study: Supplementary Paper SP 2.3.

Soeder, D., 2012, Shale Gas Development in the United States, *in* H. Al-Megren, ed., Advances in Natural Gas Technology: InTech.

Song, B., 2010, Pressure Transient Analysis and Production Analysis for New Albany Shale Gas Wells: College Station, Texas A&M University.

Taleghani, A. D., 2009, Analysis of Hydraulic Fracture Propagation in Fractured Reservoirs: An Improved Model for the Interaction between Induced and Natural Fractures: ProQuest.

Todd Energy, 2012, Hydraulic Fracturing, Enterprise & energy: New Zealand, Parliamentary Commission for the Environment.

Urbancic, T., A. Baig, and S. Bowman, 2010, Utilizing b-values and Fractal Dimension for Characterizing Hydraulic Fracture Complexity, AAPG Search and Discovery Article #90172 CSPG/CSEG/CWLS GeoConvention: Calgary, Alberta, Canada, 3 p.

US DOE, 2009, Modern Shale Gas Development in the United States: A Primer.

Veatch, R. W. J., Z. A. Moschovidis, and C. R. Fast, 1989, An Overview of Hydraulic Fracturing, *in* Recent Advances in Hydraulic Fracturing: Richardson, Texas, USA, Society of Petroleum Engineers, p. 1 –38.

Walton, I., and J. McLe, 2013, The Role of Natural Fractures in Shale Gas Production, *in* R. Jeffrey, ed., Effective and Sustainable Hydraulic Fracturing: InTech.

Wang, C., D. Ding, and Y.-S. Wu, 2013, Characterizing Hydraulic Fractures in Shale Gas Reservoirs Using Transient Pressure Tests, *in* Proceedings of the SPE Hydraulic Fracturing Technology Conference, The Woodlands, Texas.

Wang, X., and A. Ghassemi, 2012, A 3D Thermal-Poroelastic Model for Geothermal Reservoir Stimulation, *in* Thirty-seventh workshop on geothermal reservoir engineering, California.

Wang, X., and A. Ghassemi, 2011, A Three-Dimensional Stochastic Fracture Network Model for Geothermal Reservoir Stimulation, *in* Thirty-Sixth Workshop on Geothermal Reservoir Engineering (in press), Stanford University, Stanford, California.

Warpinski, N. R., M. J. Mayerhofer, M. C. Vincent, C. L. Cipolla, and E. P. Lolon, 2009, Stimulating Unconventional Reservoirs: Maximizing Network Growth while Optimizing Fracture Conductivity: SPE-114173-PA, doi:10.2118/114173-PA.

Warren, J. E., and P. J. Root, 1963, The Behavior of Naturally Fractured Reservoirs: SPE Journal, v. 3, no. 3, p. 245–255.

Wu, Y.-S., J. Li, D.-Y. Ding, C. Wang, and Y. Di, 2013, A Generalized Framework Model for the Simulation of Gas Production in Unconventional Gas Reservoirs, *in* SPE Journal, The Woodlands, Texas.

Wu, Y.-S., and G. Qin, 2009, A generalized Numerical Approach for Modeling Multiphase Flow and Transport in Fractured Porous Media: Communications in computational physics, v. 6, no. 1, p. 85.

Yu, W., B. Gao, and K. Sepehrnoori, 2014, Numerical Study of the Impact of Complex Fracture Patterns on Well Performance in Shale Gas Reservoirs: Journal of Petroleum Science Research, v. 3, no. 2, p. 83, doi:10.14355/jpsr.2014.0302.05.

Yu, W., Z. Luo, F. Javadpour, A. Varavei, and K. Sepehrnoori, 2014, Sensitivity Analysis of Hydraulic Fracture Geometry in Shale Gas Reservoirs: Journal of Petroleum Science and Engineering, v. 113, p. 1–7, doi:10.1016/j.petrol.2013.12.005.

Zhang, X., and R. G. Jeffrey, 2006, The Role of Friction and Secondary Flaws on Deflection and Re-initiation of Hydraulic Fractures at Orthogonal Pre-existing Fractures: Geophysical Journal International, v. 166, no. 3, p. 1454–1465, doi:10.1111/j.1365-246X.2006.03062.x.

APPENDICES

APPENDIX A -Derivation of Cubic's Law

The derivation of the Cubic's Law describing flow in a fracture is described by Bear et al (1993) and is presented here for report completeness.

The three dimensional balance equation for the linear momentum of an incompressible fluid in a fracture, when combined in a mass balance form, takes the form

$$\rho \frac{\partial V}{\partial t} + \rho \nabla . (VV) + \nabla p - \rho g - \mu \nabla^2 V = 0, \qquad (A.1)$$

Where ρ and μ denotes the fluid's density and dynamic viscosity, respectively, p is pressure, V is the fluid's mass weighted velocity, t is time, **g** (= -g ∇z) denotes the gravitational acceleration, and z is the vertical coordinate (positive upward).

Hubbert's potential, φ^* , for a compressible fluid, $\rho = \rho(p)$ is defined by

$$\varphi^* = z + \int_{po}^{p} \frac{dp'}{gp(p')}.$$

We shall approximate it by the piezometric head, φ, defined for a fluid of constant density , by

$$\varphi = z + \frac{p}{\rho g}. \qquad (A.2)$$

Substituting (2) into (3), yields

$$\rho \frac{\partial V}{\partial t} + \rho \nabla . (VV) + \rho g \nabla \varphi - \mu \nabla^2 V = 0 \qquad (A.3)$$

By averaging (A.3) across the fracture width (normal to the fracture axis), a two-dimensional balance equation for linear momentum can be obtained in the fracture plane

$$\int_{f_1}^{f_2} \left\{ \rho \frac{\partial V}{\partial t} + \rho \nabla \cdot (VV) + \rho g \nabla \varphi - \mu \nabla^2 V \right\} dy' = 0. \tag{A.4}$$

Since the limits of integration are independent of time, the first term in the integrand of (A.4) yields

$$\int_{f_1}^{f_2} \rho \frac{\partial V}{\partial t} dy' = \rho \frac{\partial}{\partial t} \left(\int_{f_1}^{f_2} V dy' \right) = \rho \frac{\partial (b\tilde{V})}{\partial t}, \tag{A.5}$$

Where the average of quantity A over a fracture width is defined

$$\tilde{A}(x', z') \equiv \frac{1}{b} \int_{f_1}^{f_2} A(x', y', z') dy'. \tag{A.6}$$

By applying Leibnitz's rule (for taking the derivative of an integral) to the second term in the integrand of (A.4), we obtain

$$\int_{f_1}^{f_2} \rho \nabla \cdot (VV) dy' = \rho \nabla' \cdot \int_{f_1}^{f_2} \rho VV dy' - \rho VV|_{f_2} \cdot \nabla F_2 + \rho VV|_{f_1} \cdot \nabla F_1$$

$$= \rho \nabla' \cdot (b \widetilde{VV}) - \rho VV|_{f_2} \cdot \nabla F_2 + \rho VV|_{f_1} \cdot \nabla F_1, \tag{A.7}$$

where ∇' denoted differentiation only with respect to coordinates lying in the fracture $(x'z')$-plane. By definig a velocity deviation, $\dot{V}$, such that

$$V(x', y', z') \equiv \tilde{V}(x', z') + \dot{V}(x', y', z'), \quad \tilde{\dot{V}} = 0. \tag{A.8}$$

We then have the relation

$$\widetilde{VV} = \tilde{V}\tilde{V} + \widetilde{\dot{V}\dot{V}}, \tag{A.9}$$

143

With $\rho \widetilde{V\dot V}$ representing a *dispersive momentum* flux.

By introducing (A.9) into (A.7), we obtain

$$\int_{f_1}^{f_2} \rho \nabla.(VV)\nabla dy' = \rho\nabla'.(b\widetilde{V}\widetilde{V}) + \rho\nabla'.(b\widetilde{V\dot V})$$

$$- \rho VV|_{f_2}.\nabla F_2 + \rho VV|_{f_1}.\nabla F_1. \tag{A.10}$$

The third term in the integrand of (4) is evaluated by

$$\int_{f_1}^{f_2} \rho g \nabla \varphi \, dy' = \rho g \nabla'(b\tilde\varphi) - \rho g \varphi|_{f_2}\nabla F_2 + \rho g \varphi|_{f_1}\nabla F_1. \tag{A.11}$$

Applying Leibnitz's rule to the fourth term in the integrand of (4), gives

$$\int_{f_1}^{f_2} \mu \nabla^2 V \, dy' = \mu\nabla'^2(b\widetilde V) - \mu\nabla'.(V|_{f_2}\nabla F_2 - V|_{f_1}\nabla F_1)$$

$$- \mu(\nabla V|_{f_2}.\nabla F_2 - \nabla V|_{f_1}.\nabla F_1). \tag{A.12}$$

Finally substituting (A.5), (A.10), (A.11) and (A.12) into (A.4), produces the averaged linear momentum balance equation in the fracture plane in the form

$$\rho\frac{\partial b\widetilde V}{\partial t} + \rho\nabla'.(b\widetilde V\widetilde V) + \rho\nabla'.(b\widetilde{V\dot V})$$

$$- \rho VV|_{f_2}.\nabla F_2 + \rho VV|_{f_1}.\nabla F_1$$

$$+ \rho g\nabla'(b\tilde\varphi) - \rho g\varphi|_{f_2}\nabla F_2 + \rho g\varphi|_{f_1}T\nabla F_1.$$

$$+ \mu\nabla'^2(b\widetilde V) - \mu\nabla'.(V|_{f_2}\nabla F_2 - V|_{f_1}\nabla F_1)$$

$$- \mu(\nabla V|_{f_2}.\nabla F_2 - \nabla V|_{f_1}.\nabla F_1) = 0. \tag{A.13}$$

The averaged mass balance equation takes the form

$$\frac{\partial(b\tilde{\rho})}{\partial t} + \nabla'.\left(b\tilde{\rho}\tilde{V}\right) + (\rho V)|_{f_2}.\nabla F_2 + (\rho V)|_{f_1}.\nabla F_1 = 0. \tag{A.14}$$

With the assumptions of constant fluid density and stationary, non-deformable fracture walls employed above, (A.14) reduces to

$$\nabla'.(b\tilde{\rho}) - V|_{f_2}.\nabla F_2 + V|_{f_1}.\nabla F_1 = 0. \tag{A.15}$$

Substituting (A.15) into (A.13), yields

$$\rho\frac{\partial b\tilde{V}}{\partial t} + \rho b\tilde{V}(\nabla'.\tilde{V}) + \rho\nabla'.(b\widetilde{VV})$$

$$- \rho VV|_{f_2}.\nabla F_2 + \rho VV|_{f_1}.\nabla F_1 + \rho g\nabla'(b\tilde{\varphi})$$

$$-\rho g\varphi|_{f_2}\nabla F_2 + \rho g\varphi|_{f_1}\nabla F_1$$

$$+\mu\nabla'^2(b\tilde{V}) - \mu\nabla'.(V|_{f_2}\nabla F_2 - V|_{f_1}\nabla F_1)$$

$$-\mu(\nabla V|_{f_2}.\nabla F_2 - \nabla V|_{f_1}.\nabla F_1)$$

$$+\rho\tilde{V}(V|_{f_2}\nabla F_2 - V|_{f_1}\nabla F_1) = 0. \tag{A.16}$$

To further analyze (A.16), the simple case of steady, unidirectional flow through a two-dimensional fracture bounded by the planar, parallel walls defined in Fig. A1 is considered. In addition, the following assumptions are considered

- The dispersive momentum flux is much smaller than the advective one, i.e., $\left|\rho\widetilde{VV}\right| \ll |\rho\tilde{V}\tilde{V}|$, and

- Across any aperture, the piezometric heads at the fracture walls satisfy $\varphi|_{f_2} \cong \varphi|_{f_2}$ (the stronger condition, $\varphi|_{f_2} \cong \varphi|_{f_2} \cong \tilde{\varphi}$, is required if the fracture walls are not assumed parallel).
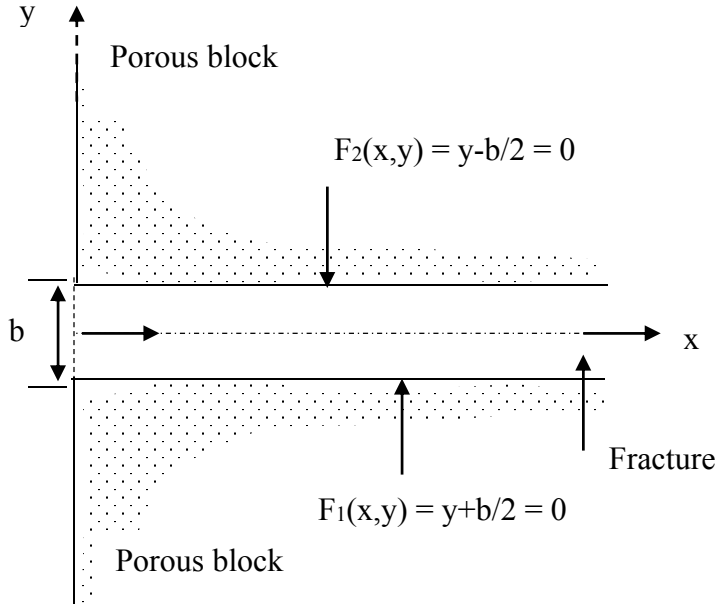
Figure A1   Fracture porous block geometry in one-dimensional case

Under these assumptions, and for steady flow, (A.16) reduces to

$$\rho g b \frac{\partial \tilde{\varphi}}{\partial x} - \mu \left(\frac{\partial V_x}{\partial y}|_{f_2} - \frac{\partial V_x}{\partial y}|_{f_1} \right) = 0. \tag{A.17}$$

146

Although (A.17) was developed for steady flow, this restriction would have been unnecessary had we neglected inertial effects already at the microscopic level, i.e., for the constant density assumed here.

$$\rho\left\{\frac{\partial V}{\partial t} + V\nabla V\right\} \cong 0, \text{ and } \nabla.V = 0.$$

If the fracture walls are stationary and impervious, and a no-slip condition (i.e. $V_x = 0$ at the walls) is imposed on them then the velocity distribution across the fracture width will be parabolic, symmetric about the fracture axis (Lamb, 1945), with

$$V_x(y) = \frac{6\widetilde{V_x}}{b^2}\left(\tfrac{1}{2}b + y\right)\left(\tfrac{1}{2}b - y\right), \quad \tfrac{1}{2}b \leq y \leq \tfrac{1}{2}b. \tag{A.18}$$

By differentiating (A.18), and substituting the result into (A.17), we obtain the average velocity in a fracture, in the form

$$\widetilde{V_x} = -\frac{\rho g}{\mu}\frac{b^2}{12}\frac{d\widetilde{\varphi}}{dx}. \tag{A.19}$$

Equation (A. 19) can be rewritten in the form

$$\widetilde{V_x} = -K_{fr}\frac{d\widetilde{\varphi}}{dx},$$

Where K_{fr}, is the *hydraulic conductivity in the fracture*, defined by

$$K_{fr} = \frac{\rho g}{\mu}\frac{b^2}{12}. \tag{A.20}$$

In general, the hydraulic conductivity, *K,* and the permeability, *k,* are related to each other by the expression

$$K = -\frac{\rho g}{\mu} k. \tag{A.21}$$

Hence the permeability in the fracture, K_{fr}, is defined as

$$K_{fr} = \frac{b^2}{12}. \tag{A.22}$$

The total discharge through a fracture, Q_{fr}, is expressed by

$$Q'_{fr} = b\tilde{V} = -\frac{\rho g}{\mu}\frac{b^3}{12}\nabla\tilde{\varphi} = -T_{fr}\nabla\tilde{\varphi}, \tag{A.23}$$

Where the prime indicates a vector in the fracture plane, and

$$T_{fr} = -\frac{\rho g}{\mu}\frac{b^3}{12} = K_{fr}b \tag{A.24}$$

APPENDIX B - Mathematical Background for Clipping Algorithm

Consider a clipping volume as defined in the figure below,
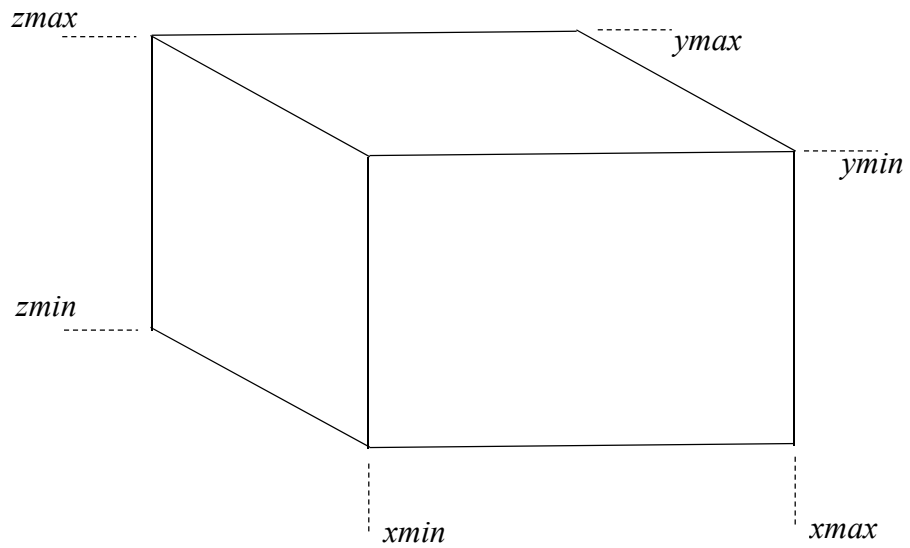
Figure B1   Clipping volume

and a line segment defined by the points (*X1, Y1, Z1)* and *(X2, Y2, Z2)* as shown
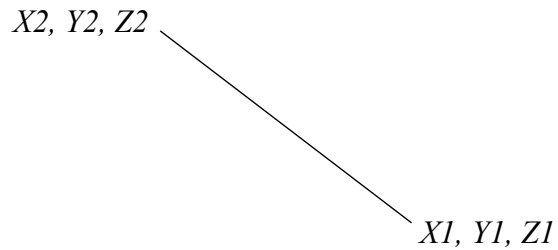
Figure B2   Straight line segment

The equation of the line above in parametric form is given by

$$\frac{(X_2 - X_1)}{l} = \frac{(Y_2 - Y_1)}{m} = \frac{(Z_2 - Z_1)}{n}$$

(B.1)

Where l, m and n are constants.

By rearranging equation (B.1), we obtain

$$\frac{X_2 - X_1}{Y_2 - Y_1} = \frac{l}{m} = \boldsymbol{a}$$

(B.2)

$$\frac{Y_2 - Y_1}{Z_2 - Z_1} = \frac{m}{n} = \boldsymbol{b}$$

(B.3)

Therefore,

$$\boldsymbol{ab} = \frac{l}{m} * \frac{m}{n} = \frac{l}{n} = \frac{X_2 - X_1}{Z_2 - Z_1}$$

(B.4)

Next, consider, the intersection of the line and the x=p plane depicted in Figure B3
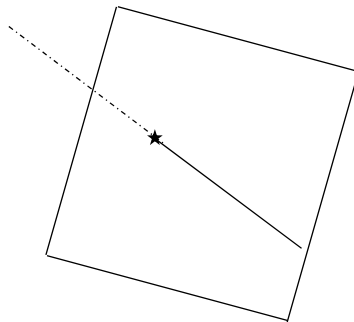
Figure B3   A straight line intersecting x= p plane.

150

To obtain the point of intersection, substitute for the point x = p using the parametric equations specified in B.2. Therefore,

$$\frac{(p - X_1)}{l} = \frac{(Y_2 - Y_1)}{m}$$

(B.5)

$$Y_2 = (p - X_1) * \frac{m}{l} + Y_1$$

(B.6)

Also from B.4,

$$\frac{(p - X_1)}{l} = \frac{(Z_2 - Z_1)}{n}$$

(B.7)

$$Z_2 = (p - X_1) * \frac{n}{l} + Z_1$$

(B.8)

The coordinates of the intersection point can thus be specified as:

$$[p, \quad \frac{(p - X_1)}{a} + Y_1, \quad \frac{(p - X_1)}{ab} + Z_1]$$

(B.9)

151

Similarly, we can consider the intersection of a line with a plane in the y-axis – y=q plane.

$$\frac{(X_2 - X_1)}{l} = \frac{(q - Y_1)}{m}$$

(B.10)

$$X_2 = (q - Y_1) * \frac{l}{m} + X_1$$

(B.11)

Also from B.4,

$$\frac{(q - Y_1)}{m} = \frac{(Z_2 - Z_1)}{n}$$

(B.12)

$$Z_2 = (q - Y_1) * \frac{n}{m} + Z_1$$

(B.13)

The coordinates of the intersection point can thus be specified as:

$$[a * (q - Y_1) + X_1, \quad q, \quad \frac{(q - Y_1)}{b} + Z_1]$$

(B.14)

Finally, consider the intersection of a line with a plane in the z-axis – z=r plane. The coordinates of the intersection point can be obtained in a similar way

152

$$\frac{(X_2 - X_1)}{l} = \frac{(r - Z_1)}{n}$$

(B.15)

$$X_2 = (r - Z_1) * \frac{l}{n} + X_1$$

(B.16)

Also from B.4,

$$\frac{(Y_2 - Y_1)}{m} = \frac{(r - Z_1)}{n}$$

(B.17)

$$Y_2 = (r - Z_1) * \frac{m}{n} + Y_1$$

(B.18)

The coordinates of the intersection point on the z-axis is then specified by:

$$[ab * (r - Z_1) + X_1, \quad b * (r - Z_1) + Y_1, \quad r]$$

(B.19)

To determine if any of the line segments lie in the clipping volume, the algorithm below is implemented.

Clipping Algorithm

Step 1: Calculate the constants a and b

Step 2: Test the line segments against the clipping volume boundaries

Lower boundaries (xmin, ymin, zmin); Upper boundaries (xmax, ymax, zmax)

For i = 1 to 2 (where i and 2 represent the end points of the line segment)

if x(i) < xmin

   y(i) = (xmin - x(i))/a + y(i);

   z(i) = (xmin - x(i))/(a*b) + z(i);

   x(i) = xmin;

elseif x(i) > xmax

   y(i) = (xmax - x(i))/a + y(i);

   z(i) = (xmax - x(i))/(a*b) + z(i);

   x(i) = xmax;

end

if y(i) < ymin

   x(i) = a*(ymin - y(i)) + x(i);

   z(i) = (ymin - y(i))/b + z(i);

   y(i) = ymin;

elseif y(i) > ymax

   x(i) = a*(ymax- y(i)) + x(i);

   z(i) = (ymax - y(i))/b + z(i);

   y(i) = ymax;

end

```
if z(i) < zmin

    x(i) = a*b*(zmin - z(i)) + x(i);

    y(i) = b*(zmin - z(i)) + y(i);

    z(i) = zmin;

elseif z(i) > zmax

    x(i) = a*b*(zmax - z(i)) + x(i);

    y(i) = b*(zmax - z(i)) + y(i);

    z(i) = zmax;

end


point (i,:) = [x(i) y(i) z(i)]; (Co-ordinates of new point)

end
```

APPENDIX C - Kriging spatial correlation algorithm

This kriging algorithm is implemented to smoothen the permeability tensor field over the computational domain of the finite element calculations. The kriging spatial correlation technique is used to interpolate for the data values at points in the formation where the data values are not explicitly calculated. The stepwise procedure to obtain the kriged data values is presented below.

i.   Compute the spatial mean of the permeability values.

ii.   Compute the distance between known locations $\Rightarrow$ distance matrix

iii. For each data pair (i, j), compute the covariance term:

$$(\mu_i - \bar{\mu})(\mu_j - \bar{\mu})$$

iv.   Order the data pairs from the lower to higher separation distance and group the data pairs within "separation rings" of distance r.

v.   Within each separation ring, compute the covariance of the data as :

$$\text{cov}\left[\mu(\vec{x}), \mu(\vec{x} + \vec{r})\right] = \frac{1}{n_r} \sum_{(i,j)=1}^{n_r} (\mu_i - \bar{\mu})(\mu_j - \bar{\mu})$$

where n_r = number of data pairs within the ring

vi.   This will result in a "covariance matrix" with each data pair (i,j) assigned a value of covariance. C_{ij} = Cov (μ_i, μ_j)

vii. Make a plot of the covariance of the data as a function of separation distance.

viii. For each data point (i), compute the distance between location (i) and the desired kriging location (o).

156

ix.   Compute the covariance C_{io} of each data pair by locating the value corresponding to distance (i,o) in the covariance plot computed in 7.

x.   Specify the weight to be assigned to each data pair

$$W_i = 1/D^2 \qquad i=1, 2......, n$$

xi.   Compute the kriging estimate as follows:

$$\hat{\mu}_o = \sum_{i=1}^{n} W_i \mu_i$$

APPENDIX D - Mesh Refinement Study

It is usually of great value to perform a mesh refinement study in order to verify the accuracy of the computational results obtained from a numerical modeling procedure. Before the results of a numerical model can be accepted as being representative of the solutions being sought for, it is essential to ensure that the results being obtained are free of any numerical effects that might be associated with the discretization of the system during the translation of the physical equations to the form being computed by the numerical solver.

The reservoir and fracture parameters utilized for this study are given in Table 4.1. To create a finite element mesh in COMSOL Multiphysics, certain input parameters need to be specified. These parameters and the values specified for these simulations are given in **Table E1** below. Control on the number of grid elements and is achieved by changing the scaling factor of the created mesh, which has a default software value of 1, after the other parameters have been specified.

Table E1   Mesh Parameters

Property	Value
Maximum element size	Model height/3
Minimum element size	Well- bore radius/3
Maximum element growth rate	1.25
Curvature factor	0.5
Resolution of narrow regions	0.6
Scaling Factor	0.55, 0.65, 0.75, 0.85, 0.95

Figure E1 presents the quality histogram of the mesh created for scaling factor values of 0.95, 0.75 and 0.55 respectively. The quality of the mesh is usually a good indication of how well the elements would approximate the solution. According to Griesmer (2014), a minimum element quality of 0.1 is satisfactory enough for numerical solutions using COMSOL Multiphysics.
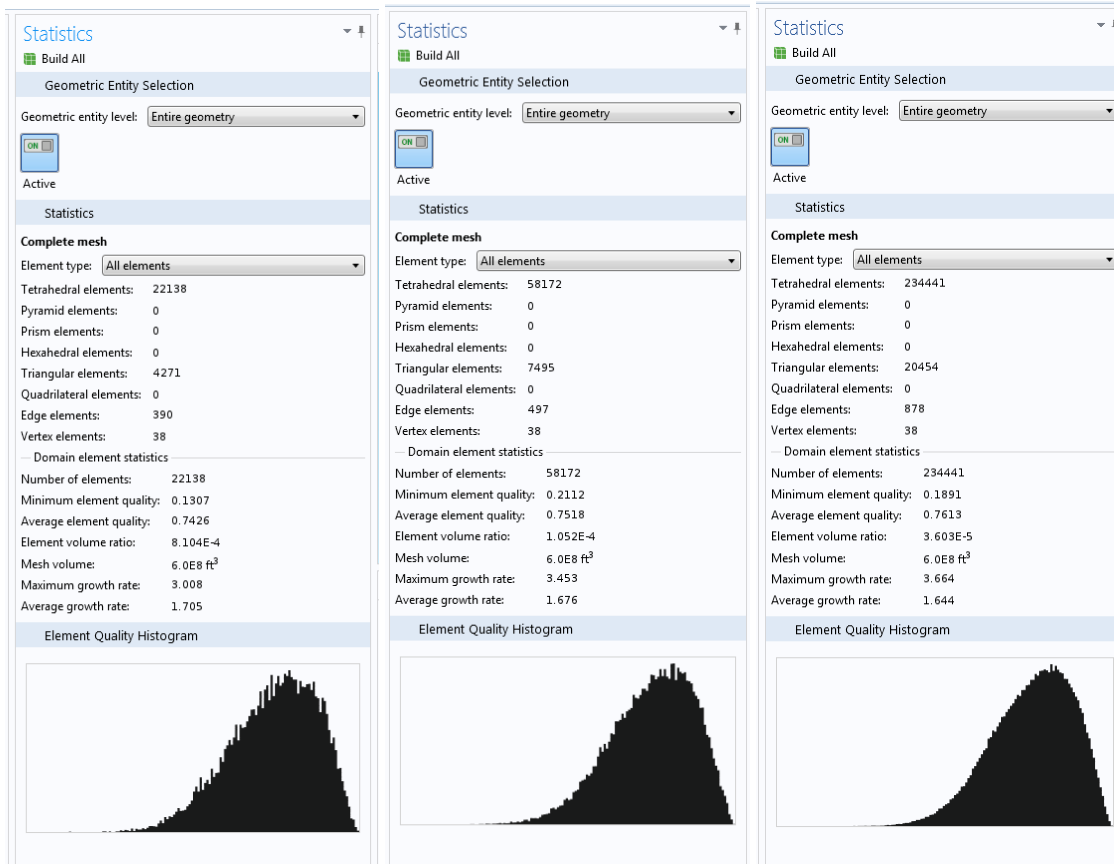
Figure E1   Mesh statistics for simulated model for scaling factor values of 0.95, 0.75 and 0.55 respectively.

The results of the steady state model study conducted utilizing the finite elements mesh obtained above is presented in **Table E2.**

Table E2   Mesh Refinement Simulation Results

Property	Scaling Factor				
	0.55	*0.65*	*0.75*	*0.85*	*0.95*
Number of tetrahedral elements	223246	100876	58172	32615	22138
Degree of freedom	312087	143050	83210	47480	32875
Computation time (s)	63	21	10	5	3
Memory Requirement (GB)	6.23	3.45	2.73	2.31	2.13
Flux (Bcf/day)	0.1203	0.1203	0.1205	0.1207	0.1209
Relative Error in Estimated Flux (%)	*0*	*0*	*0.0017*	*0.0033*	*0.005*
Relative Error in Simulated Pressure (%)	*0*	*0.04*	*0.09*	*0.10*	*0.09*

For this simulation study, an analytic solution is not available, therefore, we set up a reference solution to compare the numerical method with. The reference solution for this model is taken at a mesh scale factor of 0.55. Although the estimated steady state flux values obtained from the model do not differ significantly after the mesh simulation study, i.e. the associated errors in the estimated flux are all within a tolerance limit of 0.05, the maximum relative error associated with the approximated pressure in the simulation region exceeds the tolerance error for the coarse grids, as seen in **Table E2** and **Figure E2**. The relative error was calculated as

$$\frac{||reference\ solution - model\ solution||}{reference\ solution}$$

Alternately, in order to conserve the computational resources associated with choosing the fine scale mesh, the adaptive mesh refinement process is utilized to minimize the error associated with the computation in the zones where the maximum deviations occur. In numerical analysis, adaptive mesh refinement refers to the technique of changing the accuracy of a solution in certain

regions during the solution calculation process. This technique changes the spacing of the grid points, in order to change how accurately the solution is known in the region of interest. The advantage of this dynamic grid adaptation is that it requires less computational and storage space requirement as compared to a mesh convergence study carried out using static grids.

For the adaptive mesh refinement study, the initial mesh was chosen as the coarse mesh with a scale factor 0.95. The mesh is refined using a global refinement strategy and after 4 refinements, a better accuracy is obtained with a mesh consisting of 70118 elements as compared to the reference solution which makes use of 223, 246 elements. A comparison of the mesh parameters and simulation results is presented in **Table E3** and **Figure E3**.
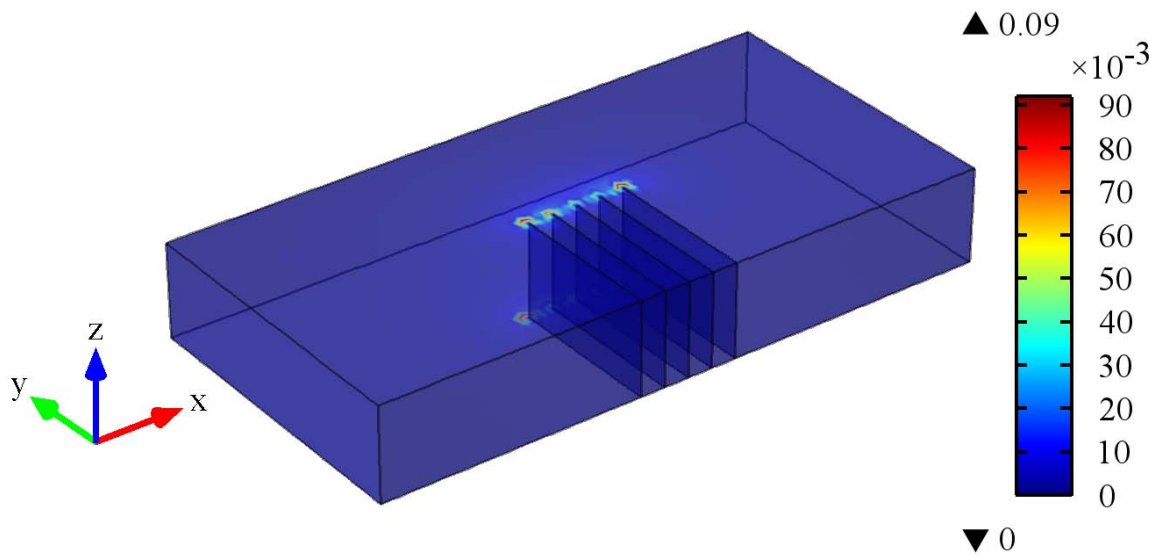
Figure E2   Distribution of error associated with estimated pressure values by comparing results from a coarse mesh (Mesh scale factor = 0.95) with reference solution (Mesh scale factor = 0.55)

Table E3   **Comparison of model results obtained using Adaptive mesh refinement**

Property	Scaling Factor		
	0.55	*0.95*	*Adapted mesh 0.95*
Number of tetrahedral elements	223246	22138	70118
Degree of freedom	312087	32875	100269
Computation time (s)	63	3	13
Memory Requirement (GB)	6.23	2.13	2.62
Flux (Bcf/day)	0.1203	0.1209	0.1203
Relative Error in Estimated Flux (%)	*0*	*0.005*	*0*
Relative Error in Simulated Pressure (%)	*0*	*0.09*	*0.05*
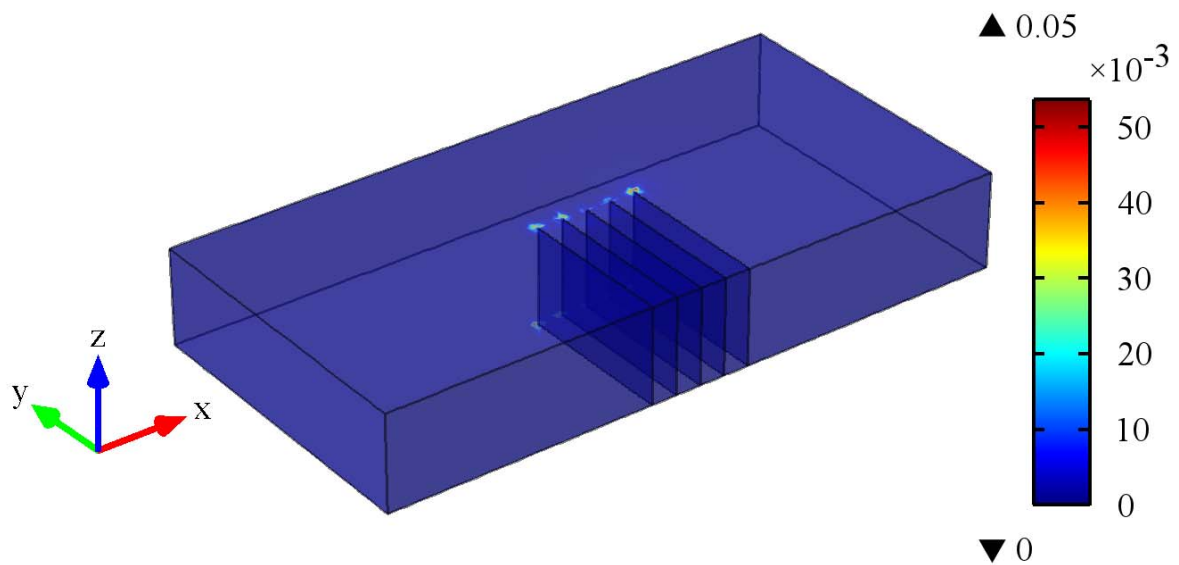
Figure E3   Distribution of error associated with estimated pressure values by comparing results from adapted mesh (Mesh scale factor = 0.95) with reference solution (Mesh scale factor = 0.55)

APPENDIX E - Model Production Validation data.

The cumulative production values obtained from the study by (Wei Yu et al., 2014) and

utilized for the construction of Figure 4.5 is presented here.

TIME (yr)	DATE	case1.irf Cumulative Gas SC (MMSCF)
0.002207	1/1/2000	0
0.002244	1/1/2000	0
0.002259	1/1/2000	0
0.002271	1/1/2000	0
0.002286	1/1/2000	0
0.002738	1/2/2000	25.51916122
0.027379	1/11/2000	82.49411011
0.054757	1/21/2000	121.9822159
0.084873	2/1/2000	156.1043243
0.112252	2/11/2000	181.7213593
0.13963	2/21/2000	204.6758118
0.164271	3/1/2000	223.7080231
0.202601	3/15/2000	250.4629974
0.249144	4/1/2000	279.8587341
0.287474	4/15/2000	302.3868713
0.33128	5/1/2000	326.3582153
0.416153	6/1/2000	367.7854309
0.498289	7/1/2000	404.0841675
0.583162	8/1/2000	438.2601013
0.668036	9/1/2000	469.6280212
0.750171	10/1/2000	497.7198486
0.835045	11/1/2000	524.6448975
0.91718	12/1/2000	548.9902344
1.002053	1/1/2001	572.562439
1.086927	2/1/2001	594.7248535
1.163587	3/1/2001	613.6907959
1.24846	4/1/2001	633.5171509
1.330595	5/1/2001	651.7043457
1.415469	6/1/2001	669.5274658
1.497604	7/1/2001	685.9487305

1.582478	8/1/2001	702.1143188
1.667351	9/1/2001	717.5443726
1.749487	10/1/2001	731.8406982
1.83436	11/1/2001	745.9848022
1.916496	12/1/2001	759.125061
2.001369	1/1/2002	772.1602783
2.086242	2/1/2002	784.6901855
2.162902	3/1/2002	795.6206665
2.247776	4/1/2002	807.2791748
2.329911	5/1/2002	818.1732178
2.414784	6/1/2002	829.0419312
2.49692	7/1/2002	839.2191772
2.581793	8/1/2002	849.394043
2.666667	9/1/2002	859.2504883
2.748802	10/1/2002	868.510498
2.833676	11/1/2002	877.800415
2.915811	12/1/2002	886.5446777
3.000685	1/1/2003	895.3331909
3.085558	2/1/2003	903.8891602
3.162218	3/1/2003	911.4381104
3.247091	4/1/2003	919.5874634
3.329227	5/1/2003	927.2870483
3.4141	6/1/2003	935.0523682
3.496236	7/1/2003	942.3955688
3.581109	8/1/2003	949.8076782
3.665982	9/1/2003	957.0512085
3.748118	10/1/2003	963.9094849
3.832991	11/1/2003	970.8411865
3.915127	12/1/2003	977.4098511
4	1/1/2004	984.0544434
4.249145	4/1/2004	1002.452698
4.498289	7/1/2004	1019.859375
4.750171	10/1/2004	1036.547119
5.002054	1/1/2005	1052.414673
5.24846	4/1/2005	1067.227051
5.497604	7/1/2005	1081.543945
5.749487	10/1/2005	1095.405029
6.001369	1/1/2006	1108.707764
6.247776	4/1/2006	1121.238647
6.49692	7/1/2006	1133.461548
6.748803	10/1/2006	1145.400024
7.000685	1/1/2007	1156.951416

7.247091	4/1/2007	1167.907471
7.496236	7/1/2007	1178.657471
7.748118	10/1/2007	1189.213867
8	1/1/2008	1199.479736
8.249145	4/1/2008	1209.368408
8.498289	7/1/2008	1219.007935
8.750172	10/1/2008	1228.514404
9.002053	1/1/2009	1237.795898
9.24846	4/1/2009	1246.672852
9.497604	7/1/2009	1255.452515
9.749487	10/1/2009	1264.139526
10.00137	1/1/2010	1272.647583
11.00068	1/1/2011	1304.555908
12	1/1/2012	1334.37207
13.00205	1/1/2013	1362.525757
14.00137	1/1/2014	1389.148926
15.00068	1/1/2015	1414.532959
16	1/1/2016	1438.84668
17.00205	1/1/2017	1462.291016
18.00137	1/1/2018	1484.851929
19.00068	1/1/2019	1506.687012
20	1/1/2020	1527.874756
21.00205	1/1/2021	1548.537964
22.00137	1/1/2022	1568.62207
23.00068	1/1/2023	1588.231445
24	1/1/2024	1607.407959
25.00205	1/1/2025	1626.237915
26.00137	1/1/2026	1644.650146
27.00068	1/1/2027	1662.723022
28	1/1/2028	1680.480591
29.00205	1/1/2029	1697.990723
30.00137	1/1/2030	1715.177002

APPENDIX F - MATLAB Programs

Single Fracture generator

```
% Model Building Interface

clear all   % - comment this line when in function mode
close all
clc


tic
%% Generate fractal pattern

n =2; % specified value of n must be 2 at least
% r =[2.4,0.4,0.4;0.7,0.3,0.3];
r =[0,0,0;0,0,0];
phi =[pi/2,0, 0];
chi =[2*pi,pi/2,-pi/2];

% axis equal

numofterms=length(phi);
if length(r)==1
    rM=ones(numofterms, 1)*r;
elseif length(r)==numofterms
    rM=r';
else
    warning on ('The sizes of scale vector and vector of angles in fractal`s generator are not
equal');
end

sumofterms = (1-numofterms^n)/(1-numofterms); % Sum of a Geometric progression

sumofprevterms = (1-numofterms^(n-1))/(1-numofterms) +1; %Required for color-coding of
fractal display

num = 1;
Startpoints = zeros(3, sumofterms, num);
Endpoints = zeros(3, sumofterms,num);

for ind = 1:num
    if ind== 1
        xb =[998 998]; yb =[10.5 10.5]; zb =[-7150 -7000];
    elseif ind==2
```

```matlab
    xb =[1001 1001]; yb =[10 11.2]; zb =[-7150 -7100];
else
    xb =[1002 1002]; yb =[10 11.2]; zb =[-7150 -7300];
end

% ----------------The matrix for coordinates for each branch----------------
% Reinitialize start and end points
A=ones(n+1,numofterms^n,3);
ndpoints = zeros(3, 1);
% ----------------- Coordinates of trunk ------------------

A(1,:,1)=ones(1,numofterms^n)*xb(1);
A(1,:,2)=ones(1,numofterms^n)*yb(1);
A(1,:,3)=ones(1,numofterms^n)*zb(1);
A(2,:,1)=ones(1,numofterms^n)*xb(2);
A(2,:,2)=ones(1,numofterms^n)*yb(2);
A(2,:,3)=ones(1,numofterms^n)*zb(2);

% ----------------- Coordinates of trunk ------------------

Startpoints(1,1,ind)=xb(1);
Startpoints(2,1,ind)=yb(1);
Startpoints(3,1,ind)=zb(1);

ndpoints(1,1)=xb(2);
ndpoints(2,1)=yb(2);
ndpoints(3,1)=zb(2);

% ------------The calculating of coordinates of branches on the base of Kantor`s array------------
--

NewCoords=zeros(3,numofterms);

count = 1;
for i=2:1:n

   z=1;
   for j=1:1:numofterms^(i-2)
      for k=1:1:numofterms
         for m=1:1:numofterms^(n-i)


            % --------------- Length of last branch --------------
            a=sqrt((A(i-1,z,1)-A(i,z,1))^2+(A(i-1,z,2)-A(i,z,2))^2+(A(i-1,z,3)-A(i,z,3))^2);
            b=sqrt((A(i,z,1)-A(i-1,z,1))^2+(A(i,z,2)-A(i-1,z,2))^2);
```

```
            theta1=acos((A(i,z,3)-A(i-1,z,3))/a);
            k2=(A(i,z,2)-A(i-1,z,2))/b;
            k1=(A(i,z,1)-A(i-1,z,1))/b;

            if (A(i,z,1)==A(i-1,z,1))&&(A(i,z,2)==A(i-1,z,2))
               k2=0;
               k1=1;
            end

            % the matrix of turning (k2 - sin(asimute), k1 - cos(asimute), theta1 - angle of
bending)
            B=[k1*cos(theta1),-k2,sin(theta1)*k1;k2*cos(theta1),k1,k2*sin(theta1);-
sin(theta1),0,cos(theta1)];
            %B=[cos(theta1),0,sin(theta1);0,1,0;-sin(theta1),0,cos(theta1)];

            for h=1:1:numofterms

               % the coordinates of base of branches
               %
               x2=a*rM(h, count)*sin(chi(h))*cos(phi(h));
               y2=a*rM(h, count)*sin(chi(h))*sin(phi(h));
               z2=a*rM(h, count)*cos(chi(h));

               NewCoords(:,h)=B*[x2,y2,z2]'+[A(i,z,1),A(i,z,2),A(i,z,3)]';

            end

            % define following coordinates
            A(i+1,z,1)=NewCoords(1,k);
            A(i+1,z,2)=NewCoords(2,k);
            A(i+1,z,3)=NewCoords(3,k);


            z=z+1;
          end

       end
       ndpoints= [ndpoints NewCoords];
    end
    count = count +1;
  end

  Endpoints(:,:, ind) = ndpoints;
  g= 2;
  for j= 1:sumofterms/3
```

```matlab
        Startpoints(:,g, ind)   = Endpoints(:,j, ind);
        Startpoints(:,g+1, ind) = Endpoints(:,j, ind);
        Startpoints(:,g+2, ind) = Endpoints(:,j, ind);
        % %     Startpoints(:,g+3) = Endpoints(:,j);
        g=g+3;

    end
end

Startpoints = reshape(Startpoints, 3, num*sumofterms);
Endpoints = reshape(Endpoints, 3, num*sumofterms);

Trans_d = [0 20 0]; % Translation is done in the positive y-direction
well_d = 0; % diameter of the wellbore - required for reflection
origin = Startpoints(:,1);

Startpointb = Ty_Transrotation(Startpoints,'ref',origin, well_d,Trans_d);
Endpointb = Ty_Transrotation(Endpoints,'ref', origin,well_d,Trans_d);

%Obtain co-ordinates for the clustered fracture network
clus_sp_1 = [Startpoints Startpointb];
clus_ep_1 = [Endpoints Endpointb];

% Replicate clustered network by translation

num_rep = 24;
[clus_dim1, clus_dim2]= size(clus_sp_1);
clus_sp = zeros(clus_dim1,clus_dim2, num_rep);
clus_ep = zeros(clus_dim1,clus_dim2, num_rep);

clus_sp(:,:,1) = clus_sp_1;
clus_ep(:,:,1) = clus_ep_1;
for i   =1 :num_rep

clus_sp(:,:, i+1) = Ty_Transrotation(clus_sp_1, 'trans',origin, well_d,Trans_d*i);
clus_ep(:,:,i+1)= Ty_Transrotation(clus_ep_1,'trans',origin, well_d,Trans_d*i);

end

% Obtain co-ordinate of all points
num_frac = clus_dim2 * (num_rep+1);

All_startpoint = reshape(clus_sp,[3 num_frac]);
All_endpoint = reshape(clus_ep,[3 num_frac]);

Parameter_vector = All_endpoint - All_startpoint;
```

```matlab
Vertices = [All_startpoint' All_endpoint' Parameter_vector'];

% Plotting Section elipses

h=figure;
axes('Parent',h,'Color',[0.,0.7,0.7]);
view(3);
hold on;
SP = Vertices(:,1:3); %start point
EP = Vertices(:,4:6); %end point
DV = Vertices(:,7:9); %direction vector
SegNorm = vectorNorm3d(DV); % length of segment
SegMid = SP + DV/2; % midpoint by vector addition
Orient = zeros(size(SP));
Orient(:,1) = atan2(DV(:,2),DV(:,1)); %angle to rotate around z axis to align x-axis with DV
Orient(:,2) = -atan2(DV(:,3),sqrt(DV(:,1).*DV(:,1) + DV(:,2).*DV(:,2)));  % angle to rotate
around new y axis to aligh new x axis with DV


for i = 1:length(Vertices)
    Start = struct('x', Vertices(i,1), 'y', Vertices(i,2),'z', Vertices(i,3));
    End = struct('x', Vertices(i,4), 'y', Vertices(i,5),'z', Vertices(i,6));
    Mid =  struct('x', SegMid(i,1), 'y', SegMid(i,2),'z', SegMid(i,3));
    Direct_vec = struct('x', Vertices(i,7), 'y', Vertices(i,8),'z', Vertices(i,9));
    Orient_vec = struct('phix', Orient(i,2), 'phiz', Orient(i,1));
    Fractures(i) = struct('Startpoint',Start,'Endpoint', End, 'Midpoint', Mid,'Dir_vec', Direct_vec,
'Length', SegNorm(i),'Orientation', Orient_vec);
end

% Plotting Section line segments

% ------------The branches of the tree---------------
count = 0;
for j = 1:50
    for i=count+1:count+sumofprevterms

line([All_startpoint(1,i),All_endpoint(1,i)],[All_startpoint(2,i),All_endpoint(2,i)],[All_startpoint(
3,i),All_endpoint(3,i)],'Color',[0.8,0.5,0.5],'LineWidth',2);
    end
    % ------------The end branches of the tree---------------

    for i=count+sumofprevterms:count+sumofterms

line([All_startpoint(1,i),All_endpoint(1,i)],[All_startpoint(2,i),All_endpoint(2,i)],[All_startpoint(
3,i),All_endpoint(3,i)],'Color',[0.4,0.75,0.4],'LineWidth',2);
```

```
    end
    count =count + sumofterms;
end

axis ([750 1250 0 1000 -7300 -7000])




% %Clip and Upscale

% Clip fracture line segments into different sub-domain configurations and
% generate upscaled permeabiity values.

BBox = [760 1240 0 1000 -7300 -7000]; %Specify extents of the Bounding box

Gridtype = 'logdiv'; % Grid size can be chosen either as regular or logarithmic
grd_sz = 3; % Select any of the numbers, 1, 2 or 3 to represent size of logarithmic subdomain
mesh. 1 is coarse, 3 is finer
NumSubDomain = [145 2 1]; % specify the number of subdomains in axis x, y, z
Interpdata = Clip_upscale(SP, DV, Orient, BBox, NumSubDomain, grd_sz, Gridtype);

%%% Krigging

% Krig the upscaled values and send to a data table


method = 'IDW';    % Method of interpolation to be used. 'IDW' or 'krig' are the options that can
be used.
r1 = 'ng';        % Type of interpolation to be utilized, 'fr' is the other option.
r2 = 8 ;          % Radius lenght if r1 == 'fr' & ...
              ...number of neighbours if  r1 =='ng'
krig_d =4 ;       % size of linear divisions in axis to be krigged

Final_interp_data=Toyin_InterpolationP(Interpdata,method,krig_d, BBox, r1,r2);

save ('C:\Users \Permeability Data\FineGrid_R26.out','Final_interp_data', '-ASCII')
% saves permeability data into file to be exported into COMSOL.


toc
```

Cluster replicating subroutine

```
function[Out] = Ty_Transrotation(SP, rotn, origin, well_d,Trans_d)

x = SP(1, :);
y = SP(2, :);
z = SP(3, :);

x_center = origin(1);
y_center = origin(2);
z_center = origin(3);

center = repmat([x_center; y_center; z_center], 1, length(x));
% choose a point which will be the center of rotation

v = [x;y;z]; % create a matrix which will be used later in calculations
well_trans = [0 0 -well_d];

rot = strcmp(rotn, 'ref');

if rot == 1
   %Reflection matrix construction - reflect about the z axis with
   R = [ 1 0 0; 0 -1 0; 0 0 -1];
   % do the rotation...
   s = v - center;
   so = R*s;          % apply the rotation about the origin

   vo = so + center;   % shift again so the origin goes back to the desired center of rotation

      Out = zeros(size(vo));

   for i = 1:3
      Out(i,:) = vo(i, :) +well_trans(i);    %translated matrix
   end

else
   %Translation matrix
%    Trans = [Trans_d 0 0];
   Trans = Trans_d;

   Out = zeros(size(v));

   for i = 1:3
      Out(i,:) = v(i, :) + Trans(i);    %translated matrix
   end
end %
```

Upscaling subroutine

```
function[Interpdata] = Clip_upscale(SP, DV, Orient, BBox, NumSubDomain, grd_sz, grid)
close all
clc
%%  Bounding box calculations

%  Generate co-ordinates of subdomain edges

if strncmp(grid, 'reg', 3)
    NumSubDomainX = NumSubDomain(1);
    XCorners = linspace(BBox(1),BBox(2),NumSubDomainX+1);
else
    XCorners = Toyin_logdivision(BBox, grd_sz);
    NumSubDomainX = length(XCorners)-1;
end

NumSubDomainY = NumSubDomain(2);
NumSubDomainZ = NumSubDomain(3);

XCorners = linspace(BBox(1),BBox(2),NumSubDomainX+1); YCorners =
linspace(BBox(3),BBox(4),NumSubDomainY+1);
ZCorners = linspace(BBox(5),BBox(6),NumSubDomainZ+1);

SubBox = zeros(NumSubDomainX*NumSubDomainY*NumSubDomainZ,6);
SubBox_centroid = zeros(1,3);

m=0;
for k= 1:length(ZCorners)-1
    for j = 1:length(YCorners)-1
        for i = 1:length(XCorners)-1
            m = m+1;
            SubBox(m,:)
=[XCorners(i),XCorners(i+1),YCorners(j),YCorners(j+1),ZCorners(k),ZCorners(k+1)];
            SubBox_centroid(m,:) =
[(XCorners(i+1)+XCorners(i))/2,(YCorners(j+1)+YCorners(j))/2,(ZCorners(k+1)+ZCorners(k))/
2];
        end
    end
    SubBox_volume = (XCorners(i+1)-XCorners(i))*(YCorners(j+1)-
YCorners(j))*(ZCorners(k+1)-ZCorners(k));
end

%% Upscaling code

Formation_permeability = [9.86923e-20 0 0; 0 9.86923e-20 0; 0 0 9.86923e-20];
```

```
Frac_porosity = 1;
Frac_width = 50; % reservoir width/grid size
Formation_porosity = 0.05;


SubBox_perm = zeros(m,9);
Total_frac_vol = zeros(m, 1);
Formation_volume = zeros(m, 1);



%
for j=1:m
   [Edge, SegmentsInBox, Radii] = newclipper([SP DV],SubBox(j,:));

   %    Radii = SegNorm(SegmentsInBox);              % Generation of the Fracture radii
   Aperture=0.02*ones(size(SegmentsInBox));    % Aperture of Fractures
   Phi = radtodeg(Orient(SegmentsInBox, 1)) ;   % Angles
   Omega = radtodeg(Orient(SegmentsInBox,2)) ;
   Total = length(SegmentsInBox);



   Permeability = (Aperture*0.3048).^2/12;  % Compute Permeability using the cubic law for
parallel plates in fractures
   L = sind(Phi).* cosd(Omega);       % directional cosine in x-direction
   M = sind(Phi).* sind(Omega);       % directional cosine in y-direction
   N = cosd(Phi);                     % directional cosine in z-direction

   Direction_Cosines = [(L.^2),(L.*M),(L.*N), (M.*L),(M.^2),(M.*N),(N.*L),(N.*M),(N.^2)];
   Fracvolume =  Aperture.*Radii*Frac_width;  %Volume of voids occupied by fractures
   Total_frac_vol(j) = sum(Fracvolume);
   Formation_volume(j) =SubBox_volume;
   Crack_tensor = zeros(3,3);

   %%
   for i = 1:Total
      OrientMatrix = [Direction_Cosines(i,1) Direction_Cosines(i,2) Direction_Cosines(i,3);
Direction_Cosines(i,4) Direction_Cosines(i,5) Direction_Cosines(i,6);Direction_Cosines(i,7)
Direction_Cosines(i,8) Direction_Cosines(i,9)];
      Crack_tensor = Crack_tensor + (Fracvolume(i)*Permeability(i)*OrientMatrix);
   end

   Fracture_crack_tensor = Crack_tensor/Formation_volume(j);

   Permeability_tensor = ((sum(diag(Fracture_crack_tensor))*eye(size(Fracture_crack_tensor)))-
Fracture_crack_tensor);

   [Eigval, Frac_k_tensor] = eig(Permeability_tensor);
```

```
    Percent_frac = Total_frac_vol(j)/Formation_volume(j) ;      %Percentage of formation
occupied by fractures


    Overall_upscaled_k = (Percent_frac*Frac_k_tensor) + (1-
Percent_frac)*Formation_permeability;                          %Upscaled Permeability
    Overall_upscaled_porosity = (Percent_frac* Frac_porosity) + (1-
Percent_frac)*Formation_porosity; %Upscaled Porosity


    SubBox_perm(j,:) = [Overall_upscaled_k(1,1), Overall_upscaled_k(1,2),
Overall_upscaled_k(1,3),Overall_upscaled_k(2,1), Overall_upscaled_k(2,2),
Overall_upscaled_k(2,3),Overall_upscaled_k(3,1), Overall_upscaled_k(3,2),
Overall_upscaled_k(3,3)];



end
Final_frac_vol = sum(Total_frac_vol);
Final_form_vol = sum(Formation_volume);
Equiv_HF_length = Final_frac_vol/(0.001*Frac_width);

Interpdata = [SubBox_centroid, SubBox_perm(:,1), SubBox_perm(:,5),SubBox_perm(:,9)];
% Matrix of co-ordinates and permeability points.
```

Logarithmic division subroutine

```
function xloc =Toyin_logdivision(BBox, grid_sz)
clc
close all
%code works for internal sections
%treat boundaries differently
Boundaries = [BBox(1) BBox(2)];
% grid_sz=3;
% Boundaries = [760 1240];
% divide x into logarithmic spaces

% determine the number of HF Locations
% HFloc = Nfracs;
HFloc = 5;
Fracloc = zeros(1, HFloc);
Fracspac = (Boundaries(2)- Boundaries(1))/(HFloc);
multiplier = Fracspac/2;

x1 = zeros(HFloc,6); %preallocate matrix of larger grids

if grid_sz == 1
    xgrid1 = zeros(HFloc,6); %preallocate matrix of smaller grids
    xgrid2 = zeros(HFloc-1,5); %to be used for reshaping

    for n= 1:HFloc
        if n == 1
            Fracloc(n) = Boundaries(1) + multiplier;
        else
            Fracloc(n) = Fracloc(1) + multiplier*(2*(n-1));
        end
        % determine number of subdivisions - total of 5 including HF

        x1(n,1) = Fracloc(n) - multiplier;
        x1(n,end) = Fracloc(n) + multiplier;

        x1(n,2) = x1(n,1) + (multiplier * 0.905);
        x1(n,3) = x1(n,2)+ (multiplier *0.0949948);
        x1(n,4) = x1(n,3)+ (multiplier *0.00104);
        x1(n,5) = x1(n,4)+ (multiplier *0.0949948);

        % get more grid points

        xgrid1(n, :) = x1(n,:);

        if n>=2
```

176

```matlab
        xgrid2(n-1, :) = xgrid1(n, 2:end);
      end
      % xgrid1(n, :) = [linspace(x1(n,1),x1(n,2),6), (x1(n,2)+ (multiplier *0.09499)/2), x1(n,3),
x1(n,4), (x1(n,4)+ (multiplier *0.09499)/2), linspace(x1(n,5),x1(n,end),6)]; end
      % end
    end
    if HFloc == 1
      xloc = xgrid1;
    else
      xloc_1 = xgrid1(1, :);
      xloc_a = xgrid2';
      xloc_2 = reshape(xloc_a, [1, (HFloc-1)*5]);
      xloc = [xloc_1, xloc_2];
    end

elseif grid_sz== 2
  xgrid1 = zeros(HFloc,16); %preallocate matrix of smaller grids
  xgrid2 = zeros(HFloc-1,15); %to be used for reshaping

  for n= 1:HFloc
    if n == 1
      Fracloc(n) = Boundaries(1) + multiplier;
    else
      Fracloc(n) = Fracloc(1) + multiplier*(2*(n-1));
    end
    % determine number of subdivisions - total of 5 including HF

    x1(n,1) = Fracloc(n) - multiplier;
    x1(n,end) = Fracloc(n) + multiplier;

    x1(n,2) = x1(n,1) + (multiplier * 0.905);
    x1(n,3) = x1(n,2)+ (multiplier *0.09499);
    x1(n,4) = x1(n,3)+ (multiplier *0.002);
    x1(n,5) = x1(n,4)+ (multiplier *0.09499);

    % get more grid points
    xgrid1(n, :) = [linspace(x1(n,1),x1(n,2),6), (x1(n,2)+ (multiplier *0.09499)/2), x1(n,3),
x1(n,4), (x1(n,4)+ (multiplier *0.09499)/2), linspace(x1(n,5),x1(n,end),6)];

    if n>=2
      xgrid2(n-1, :) = xgrid1(n, 2:end);
    end

  end
  if HFloc == 1
    xloc = xgrid1;
```

```matlab
    else
        xloc_1 = xgrid1(1, :);
        xloc_a = xgrid2';
        xloc_2 = reshape(xloc_a, [1, (HFloc-1)*15]);
        xloc = [xloc_1, xloc_2];
    end

else
    xgrid1 = zeros(HFloc,30); %preallocate matrix of smaller grids
    xgrid2 = zeros(HFloc-1,29); %to be used for reshaping

    for n= 1:HFloc
        if n == 1
            Fracloc(n) = Boundaries(1) + multiplier;
        else
            Fracloc(n) = Fracloc(1) + multiplier*(2*(n-1));
        end
        % determine number of subdivisions - total of 5 including HF

        x1(n,1) = Fracloc(n) - multiplier;
        x1(n,end) = Fracloc(n) + multiplier;

        x1(n,2) = x1(n,1) + (multiplier * 0.905);
        x1(n,3) = x1(n,2)+ (multiplier *0.09499);
        x1(n,4) = x1(n,3)+ (multiplier *0.002);
        x1(n,5) = x1(n,4)+ (multiplier *0.09499);

        % get more grid points

        xgrid1(n, :) = [linspace(x1(n,1),x1(n,2),11), (x1(n,2)+ 0.25*(multiplier
*0.09499)),(x1(n,2)+ 0.5*(multiplier *0.09499)), (x1(n,2)+ 0.75*(multiplier *0.09499)), x1(n,3),
x1(n,4), (x1(n,4)+ 0.25*(multiplier *0.09499)),(x1(n,4)+ 0.5*(multiplier *0.09499)), (x1(n,4)+
0.75*(multiplier *0.09499)), linspace(x1(n,5),x1(n,end),11)];


        if n>=2
            xgrid2(n-1, :) = xgrid1(n, 2:end);
        end
        % xgrid1(n, :) = [linspace(x1(n,1),x1(n,2),6), (x1(n,2)+ (multiplier *0.09499)/2), x1(n,3),
x1(n,4), (x1(n,4)+ (multiplier *0.09499)/2), linspace(x1(n,5),x1(n,end),6)]; end
        % end
    end
    if HFloc == 1
        xloc = xgrid1;
    else
        xloc_1 = xgrid1(1, :);
```

```
    xloc_a = xgrid2';
    xloc_2 = reshape(xloc_a, [1, (HFloc-1)*29]);
    xloc = [xloc_1, xloc_2];
  end
end
```

Clipping subroutine

```
function varargout = newclipper(line, box)

% Clipping algorithm

%% Variables
% line = M x 6 matrix specifying a point on the line and its direction...
%       vector
% box = 1 x 6 vector containing the end points of the clipping box.
% output_edge = M x 6 matrix specifying End points of clipped lines.
% index = index of line segments contained in clipped box
% Radii = calculated length of clipped line segments

%Examples
% Code functionality can be tested uncommenting lines 23 to 30 and running
% as a script.
% clear all
% close all
% clc
% line = [60 40 3 10 11 10];
% % 0.1 2 2 0 1.2 -0.56; 0.5 0.2 0.8 ...
% ...0.4 0.55 1.33; 0.1 0.1 0.1 0 1.9 1.9];
%     box = [50 65 0 50 0 50];

%% Initialization section

tol = 1e-12;
num_lines = size(line,1);
% determine the number of lines to be processed

edge = zeros(num_lines,6);
% Pre-allocate matrix of box edges

xmin = box(1);   xmax = box(2);
% Specify the box constraints in the x-direction

ymin = box(3);   ymax = box(4);
% Specify the box constraints in the y-direction

zmin = box(5);   zmax = box(6);
% Specify the box constraints in the z-direction

for j = 1 : num_lines
    point = zeros(2,3);
    % Preallocate the values of the first point
```

```matlab
point(1,:) = line(j, 1:3);
% Specify the co-ordinates of the first point on the line

point(2,:) = line(j, 1:3) + line(j, 4:6);
% Specify coordinates of the second point on the line

x = [point(1,1);point(2,1)];
% Specify the line values in the x-direction

y = [point(1,2);point(2,2)];
% Specify the line values in the y-direction

z = [point(1,3);point(2,3)];
% Specify the line values in the z-direction

l = (x(2) - x(1)); m =(y(2) - y(1)); n = (z(2) - z(1));

%% Computation Section
if l== 0 % line is parallel to yz plane
    numcase = 1;
    point = newclip2D(x, y, z, xmin, xmax , ymin, ymax, zmin, zmax, numcase);
elseif m == 0 % line is parallel to xz plane
    numcase = 2;
    point = newclip2D(x, y, z, xmin, xmax , ymin, ymax, zmin, zmax, numcase);
elseif n == 0 % line is parrallel to xy plane
    numcase = 3;
    point = newclip2D(x, y, z, xmin, xmax , ymin, ymax, zmin, zmax, numcase);
else % 3d computation
    a = l/m;    b = m/n;
    % Parametric constant required for scaling
    for i = 1:2

        if x(i) < xmin
            y(i) = (xmin - x(i))/a + y(i);
            z(i) = (xmin - x(i))/(a*b) + z(i);
            x(i) = xmin;
        end
        if x(i) > xmax
            y(i) = (xmax - x(i))/a + y(i);
            z(i) = (xmax - x(i))/(a*b) + z(i);
            x(i) = xmax;
        end
```

181

```matlab
            if y(i) < ymin
                x(i) = a*(ymin - y(i)) + x(i);
                z(i) = (ymin - y(i))/b + z(i);
                y(i) = ymin;
            end
            if y(i) > ymax
                x(i) = a*(ymax- y(i)) + x(i);
                z(i) = (ymax - y(i))/b + z(i);
                y(i) = ymax;
            end

            if z(i) < zmin
                x(i) = a*b*(zmin - z(i)) + x(i);
                y(i) = b*(zmin - z(i)) + y(i);
                z(i) = zmin;
            end
            if z(i) > zmax
                x(i) = a*b*(zmax - z(i)) + x(i);
                y(i) = b*(zmax - z(i)) + y(i);
                z(i) = zmax;
            end
            point(i,:) = [x(i) y(i) z(i)];

        end
        check = (abs(diff(x)))+(abs(diff(y)))+(abs(diff(z)));

        if check <=tol
            point =NaN(size(point)); % Not in selected box
        end
    end
    edge(j,:) =[point(1,:) point(2,:)];
end

%% Output Section

edge_for_indx = zeros((size(edge, 1)),1);

for i = 1:size(edge, 1)
    for j = 1:size(edge, 2)
        if isnan(edge(i,j)) == 1
            edge_for_indx(i) = NaN;
            break
        elseif isinf(edge(i,j)) == 1
            edge_for_indx(i) = NaN;
            break
        else
```

```matlab
        edge_for_indx(i) = edge(i,1);
    end
  end
end

[index]= find(~isnan(edge_for_indx));

output_edge = edge(index,:);

%calculate radii of clipped segments
Edge_dir_vec = output_edge(:, 4:6) - output_edge(:, 1:3);
Radii = vectorNorm3d(Edge_dir_vec); % length of segment

varargout{1} = output_edge;

if nargout == 3
   varargout{2} = index;
   varargout{3} = Radii;
end
```

2D clipping subroutine

```matlab
% Program for clipping of lines parallel to the bounding box planes

function point =  newclip2D(x, y, z, xmin, xmax , ymin, ymax, zmin, zmax, numcase)

point = zeros(2,3);
tol = 1e-14;

switch numcase
   %%
   case 1 % parallel to the yz plane

      if x(1) >= xmin && x(1) <= xmax

         if z(1) == z(2)
            if z(1) >= zmin && z(1) <= zmax
               for i = 1: 2
                  if y(i) < ymin
                     y(i) = ymin;
                  elseif y(i) > ymax
                     y(i) = ymax;
                  end
               end
```

```matlab
        if abs(diff(y)) <tol
            point =NaN(size(point)); % Not in selected box
        else
            point = [x(1) y(1) z(1); x(2) y(2) z(2)];
        end
    else
        point =NaN(size(point)); % Not in selected box
    end


elseif y(1) == y(2)
    if y(1) >= ymin && y(1) <= ymax
        for i = 1: 2
            if z(i) < zmin
                z(i) = zmin;
            elseif z(i) > zmax
                z(i) = zmax;
            end
        end
        if abs(diff(z)) <tol
            point =NaN(size(point)); % Not in selected box
        else
            point = [x(1) y(1) z(1); x(2) y(2) z(2)];
        end
    else
        point =NaN(size(point)); % Not in selected box
    end

else
    m = (z(2) - z(1)) / (y(2) - y(1));
    c= (y(1)*z(2) -y(2)*z(1))/( y(1) - y(2));
    for i = 1:2
        if y(i) < ymin
            z(i) = m*ymin + c;
            y(i) = ymin;
        elseif y(i) > ymax
            z(i) = m*ymax + c;
            y(i) = ymax;
        end

        if z(i) < zmin
            y(i) = (zmin -c)/m;
            z(i) = zmin;
        elseif z(i) > zmax
            y(i) = (zmax -c)/m;
            z(i) = zmax;
```

184

```
            end

         point(i,:) = [x(i) y(i) z(i)];
      end
      check = abs(diff(y))+ abs(diff(z));

      if check <=tol
         point =NaN(size(point)); % Not in selected box

      end
   end
 else
   point =NaN(size(point)); % Not in selected box
 end

 %%
case 2 % parallel to the xz plane

 if y(1) >= ymin && y(1) <= ymax

    if z(1) == z(2)
      if z(1) >= zmin && z(1) <= zmax
         for i = 1: 2
            if x(i) < xmin
               x(i) = xmin;
            elseif x(i) > xmax
               x(i) = xmax;
            end
         end
         if abs(diff(x)) <tol
            point =NaN(size(point)); % Not in selected box
         else
            point = [x(1) y(1) z(1); x(2) y(2) z(2)];
         end
      else
         point =NaN(size(point)); % Not in selected box
      end


    elseif x(1) == x(2)
      if x(1) >= xmin && x(1) <= xmax
         for i = 1: 2
            if z(i) < zmin
               z(i) = zmin;
            elseif z(i) > zmax
               z(i) = zmax;
```

185

```
                    end
                end
                if abs(diff(z)) <tol
                    point =NaN(size(point)); % Not in selected box
                else
                    point = [x(1) y(1) z(1), x(2) y(2) z(2)];
                end
            else
                point =NaN(size(point)); % Not in selected box
            end


        else
            m = (z(2) - z(1)) / (x(2) - x(1));
            c= (x(1)*z(2) -x(2)*z(1))/( x(1) - x(2));
            for i = 1:2
                if x(i) < xmin
                    z(i) = m*xmin + c;
                    x(i) = xmin;
                elseif x(i) > xmax
                    z(i) = m*xmax + c;
                    x(i) = xmax;
                end

                if z(i) < zmin
                    x(i) = (zmin -c)/m;
                    z(i) = zmin;
                elseif z(i) > zmax
                    x(i) = (zmax -c)/m;
                    z(i) = zmax;
                end
                point(i,:) = [x(i) y(i) z(i)];
            end
            check = abs(diff(x))+ abs(diff(z));

            if check <=tol
                point =NaN(size(point)); % Not in selected box

            end
        end
    else
        point =NaN(size(point)); % Not in selected box
    end

    %%
case 3 % parallel to the xy plane
    if z(1) >= zmin && z(1) <= zmax
```

```
if y(1) == y(2)
   if y(1) >= ymin && y(1) <= ymax
      for i = 1: 2
         if x(i) < xmin
            x(i) = xmin;
         elseif x(i) > xmax
            x(i) = xmax;
         end
      end
      if abs(diff(x)) <tol
         point =NaN(size(point)); % Not in selected box
      else
         point = [x(1) y(1) z(1); x(2) y(2) z(2)];
      end
   else
      point =NaN(size(point)); % Not in selected box
   end


elseif x(1) == x(2)
   if x(1) >= xmin && x(1) <= xmax
      for i = 1: 2
         if y(i) < ymin
            y(i) = ymin;
         elseif y(i) > ymax
            y(i) = ymax;
         end
      end
      if abs(diff(y)) <tol
         point =NaN(size(point)); % Not in selected box
      else
         point = [x(1) y(1) z(1); x(2) y(2) z(2)];
      end
   else
      point =NaN(size(point)); % Not in selected box
   end

else
   m = (y(2) - y(1)) / (x(2) - x(1));
   c= (x(1)*y(2) -x(2)*y(1))/( x(1) - x(2));
   for i = 1:2
      if x(i) < xmin
         y(i) = m*xmin + c;
         x(i) = xmin;
      elseif x(i) > xmax
```

```
            y(i) = m*xmax + c;
            x(i) = xmax;
        end

        if y(i) < ymin
            x(i) = (ymin -c)/m;
            y(i) = ymin;
        elseif y(i) > ymax
            x(i) = (ymax -c)/m;
            y(i) = ymax;
        end
        point(i,:) = [x(i) y(i) z(i)];
    end
    check = abs(diff(x))+ abs(diff(y));

    if check <=tol
        point =NaN(size(point)); % Not in selected box

    end
  end
else
    point =NaN(size(point)); % Not in selected box
end
end
```

Kriging subroutine

```
%%%%%%%%%%%%%%%%%%%%%%%%%%%%%%%%%%%%%%%%%%%%%%%%%%%%%
%%% Krigging Interpolation %%%
%%%%%%%%%%%%%%%%%%%%%%%%%%%%%%%%%%%%%%%%%%%%%%%%%%%%%

function Final_interp_data=Toyin_InterpolationP(Interp_Data, method,num, BBox, r1,r2)

%% Variable Specifications
% INPUTS
% Interp_data = Matrix [length(xc), 6] with co-ordinate...
%               values and determined properties
% n         = Number of divisions in each direction
% method    = String input for method of interpolation: 'krig' = krigging;...
%                               'IDW' = Inverse Distance Weighting
% r1        = String input for type of interpolation: 'fr' = fixed radius;...
%                               'ng' = neighbours
% r2        = Radius lenght if r1 == 'fr' & ...
%             number of neighbours if  r1 =='ng'

% OUTPUTS
% Final_interp_data = Matrix [length(z)*length(y)*length(x), 6] with ...
%               interpolated variable  and co-ordinate values.

% EXAMPLE
% --> Permeability_data =InterpolationP(Interp_data, 30,'ng',length(x1));

%%%%%%%%%%%%%%%%%%%%%%%%%%%%%%%%%%%%%%%%%%%%%%%%%%%%%%%%%%%
%%%%
%  $Adapted  from Simone Fatichi IDW code(MATLAB Xchange ...
%   ...and expanded by Toyin Aseeperi 2013/10/14
%%%%%%%%%%%%%%%%%%%%%%%%%%%%%%%%%%%%%%%%%%%%%%%%%%%%
clc
close all

% % % Initialize data to test when not in function mode.
% Interp_Data=load('C:\Users\Interp_data.out');
% % send in at least two data points
% % n= 20;
% BBox = [0 20 0 30 0 50];
% method = 'IDW';
% r1 = 'fr' ;
% r2 = 2;
```

189

```matlab
%% Extract data into new variables to be used for computation
xc = Interp_Data(:,1)';
yc = Interp_Data(:,2)';
zc = Interp_Data(:,3)';

VariableC = Interp_Data(:,4:end)';
Means = mean(VariableC, 2);


x = BBox(1):num:BBox(2);
y = BBox(3):num:BBox(4);
z = BBox(5):num:BBox(6);


count = 1;                              % Initiate count for use in obtaining the co-ordinate
positions later in the loop
Coord_index = length(x)*length(y)*length(z);          % Determine new length for generated
data
Coord=zeros(Coord_index ,3);        % Preallocate matrix of Co-ordinate indexes
Intp_Vari=zeros(length(x),length(y),length(z),size(VariableC, 1)); % Preallocate matrix of
inerpolated variables

%Generate Distance Matrix A
n = length(xc);
A= zeros(n);

for i = 1:n
    for j = 1:n
        A(i,j)= sqrt((xc(i)-xc(j))^2 +(yc(i)-yc(j))^2+(zc(i)-zc(j)).^2);
    end
end
% A(:, end) = 1;
% A(end, 1:end-1) = 1;
% A(end, end) = 0;
CovC = zeros(n);

%% Computation Section

% Fixed radius computation
if  strcmp(r1,'fr')
    if  (r2<=0)
        disp('Error: Radius must be positive')
        return
    end
%     for a = 1: size(VariableC, 1)
%         for l = 1:n
```

190

```matlab
%            for m = 1:n
%                vcc =VariableC(a, :);
        vcc =VariableC;
%     CovC(l,m)= (vcc(l)-mean(vcc))*(vcc(m)-mean(vcc));
%            end
%        end
%        CovC(:, end) = 1;
%        CovC(end, 1:end-1) = 1;
%        CovC(end, end) = 0;
%        plot(A, CovC)
    for k = 1:length(z)
        for j=1:length(y)
            for i =1:length(x)
                Distance= sqrt((x(i)-xc).^2 +(y(j)-yc).^2 +(z(k)-zc).^2);

%                if min(Distance)==0
%                    disp('Error: One or more stations have the coordinates of an
interpolation point')
%                    return
%                end

            if  strcmp(method,'krig')
                Weights = Toyin_krigweight(CovC, Distance);     % Krigging weights
            else
                Weights = ones(1, length(Distance))./Distance.^2;  % Inverse distance algorithm
weights
            end


%            Weights = Weights(Distance<10); vcc = vcc(Distance<10);
            % To utilize a fixed radius for computation, enable the line above.
            V = vcc.*Weights;

            if isempty(Distance)
                V=NaN;
            else
                V=sum(V)/sum(Weights);
                Intp_Vari(i, j, k)=V;
%                if a==1
                Coord(count, :)= [x(i) y(j), z(k)];
                count = count+1;
%                end
            end

        end
    end
```

191

```matlab
    end
% end

%%%%%%%%%%%%%%%%%%%%%%%%%%%%%%%%%%%%%%%%%%%%%%%%%%%%%%%%
% Nearest neighbor computation

else
    if r2 > length(VariableC)
        r2 = length(VariableC);
    end
    if r2<1
        disp('Error: Number of neighbours not congruent with data')
        return
    end
    for a = 1: size(VariableC, 1)
        for k = 1: length(z)
            for j=1:length(y)
                for i=1:length(x)
                    Distance= sqrt((x(i)-xc).^2 +(y(j)-yc).^2+(z(k)-zc).^2);
                    if min(Distance)==0
                        disp('Error: One or more stations have the coordinates of an interpolation point')
                        return
                    end
                    [Distance,I]=sort(Distance);
                    vcc=VariableC(a,I);
                    if  strcmp(method,'krig')

                        Weights = Toyin_krigweight(A, Distance);    % Krigging weights
                    else
                        Weights = ones(1, length(Distance))./(Distance.^2);          % Inverse distance
algorithm weights
                    end

                    Weights=Weights(1:r2); vcc = vcc(1:r2);
                    %                To utilize a fixed number of neighbors for
                    %                computation, enable the line above.
                    V = vcc.*Weights;
                    V=sum(V)/sum(Weights);
                    Intp_Vari(i, j, k, a)=V;
                    if a==1
                        Coord(count, :)= [x(i) y(j), z(k)];
                        count = count+1;
                    end
                end
            end
        end
    end
```

```
    end
end
%% Format output data

Data_length = length(x)*length(y)*length(z);
Perm = reshape(Intp_Vari,Data_length,size(VariableC, 1));
Final_interp_data = [Coord, Perm];

%% For debugging when not in function mode
% save C:\Users \Desktop\Final_interp_data.out Final_interp_data -ASCII

%%%%%%%%%%%%%%%%%%%%%%%%%%%%%%%%%%%%%%%%%%%%%%%%%%%%%%%%%%%
%%%%%%%%%%%%%%%%%%%
```
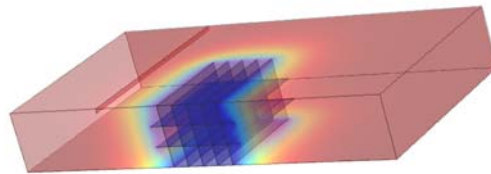
APPENDIXG – Sample COMSOL Report.

COMSOL
MULTIPHYSICS®

Report Generator

Author

Toyin Aseeperi

Summary

This report presents the steps involved in the geometry definition and flow solution in a fractured shale formation

Report Contents

1 Global Definitions

1.1 Parameters 1

Parameters

Name	Expression	Description
wellbore_pres	1000[psi]	Pressure at perforates
init_pres	3800[psi]	Initial Reservoir pressure
total_reservoir_width	22000[ft]	Overall Reservoir extent
depth_res	1000[ft]	Reservoir depth - y direction
height_res	300[ft]	Height of reservoir
num_stage	11	Number of stages in reservoir
width_res	total_reservoir_width/num_stage	Stage extent in wellbore direction
rad_well	5[ft]	Well radius
eta	0.02[cP]	Dynamic viscosity
rho_g	0.716[g/L]	Fluid density at standard conditions
IG_const	8.314[kJ/(kmol*K)]	Ideal Gas Constant
MMass	16[g/mol]	Molar mass of Methane
Temp	180[degF]	Reservoir Temperature
perm_mat	1e-4[mD]	Matrix Permeability
por_mat	0.06	Matrix Porosity
perm_frac	5000[mD]	Fracture permeability
aper_frac	0.02[ft]	Fracture Aperture
por_frac	1	Fracture Porosity

Name	Expression	Description
width_frac	500[ft]	Fracture width
height_frac	300[ft]	Fracture height
num_frac	5	Number of fractures
dist_frac	80[ft]	Fracture spacing
perm_sep	1e2[mD]	Shale separation pemeability
por_sep	0.2	Shale seperation porosity
aper_sep	0.02[ft]	Shale separation aperture
dist_sep	100[ft]	Separation distance
num_sep	2	Number of separation layers
width_sep	450[ft]	Separation width
height_sep	500[ft]	Separation height
Lang_pres	650[psi]	Langmuir Pressure
Lang_vol	96[ft^3/ton]	Langmuir volume
rock_dens	2580[kg/m^3]	Rock Density
prod_rate	5000e3[ft^3/d]	Pumping rate
Stage_flux	prod_rate*rho_g/num_stage	Overall Flux value
Mass_source	Stage_flux/(depth_res*width_res*height_res)	Mass source
Res_flux	prod_rate*rho_g	Flux Value
daily_vol_stage_flux	(Stage_flux/rho_g)*3.051e6	Flux value in cubic ft/day
mesh_scf	1	Mesh Scale factor
sat	0.7	

Name	Expression	Description
fault_dis	500[ft]	Distance to middle of reservoir
fault_width	1000[ft]	Fault width
fault_height	20[ft]	Fault height
fault_perm	100[mD]	Fault permeability

1.2 Variables

1.2.1 Variables 1

Selection

Geometric entity level	Entire model

Name	Expression	Description
comp	(zfac(comp1.p)/comp1.p) * d(comp1.p/zfac(comp1.p), comp1.p)	
rho_f	(MMass*comp1.p)/(zfac(comp1.p)*IG_const*Temp)	
fluid_com	comp*sat	
ads_com	((rock_dens*Lang_vol*Lang_pres)/(comp1.p + Lang_pres)^2)*(rho_g/rho_f)	
Shale_com	1e-6[1/psi]	
Shale_com2	Shale_com + ads_com	
Flow_rate	(comp1.p_lm1/rho_g)*3.051	flow rate in MMcf/day
kappax	permx(x[1/ft], y[1/ft], z[1/ft])	
kappay	permy(x[1/ft], y[1/ft], z[1/ft])	
kappaz	permz(x[1/ft], y[1/ft], z[1/ft])	

1.3 Functions

1.3.1 Interpolation 3

Function name	pbound
Function type	Interpolation

pbound(t) (psi)
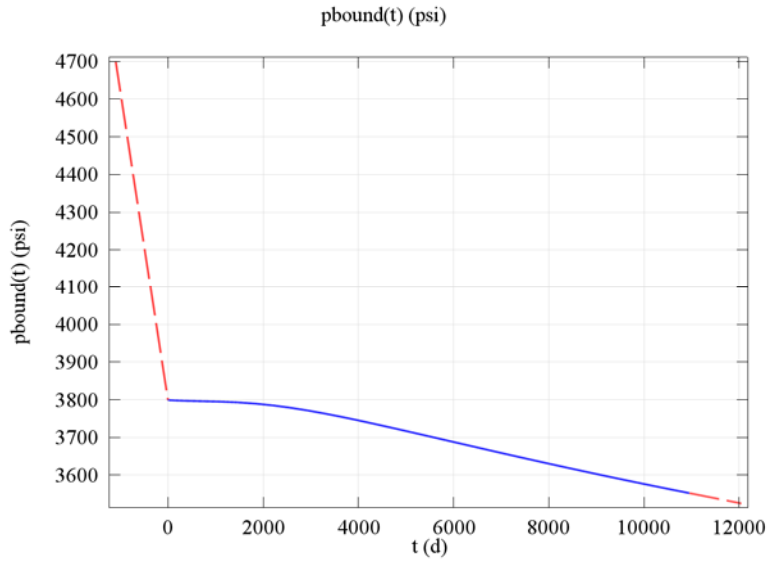
Interpolation 3

1.3.2 Interpolation 4

Function name	permea
Function type	Interpolation
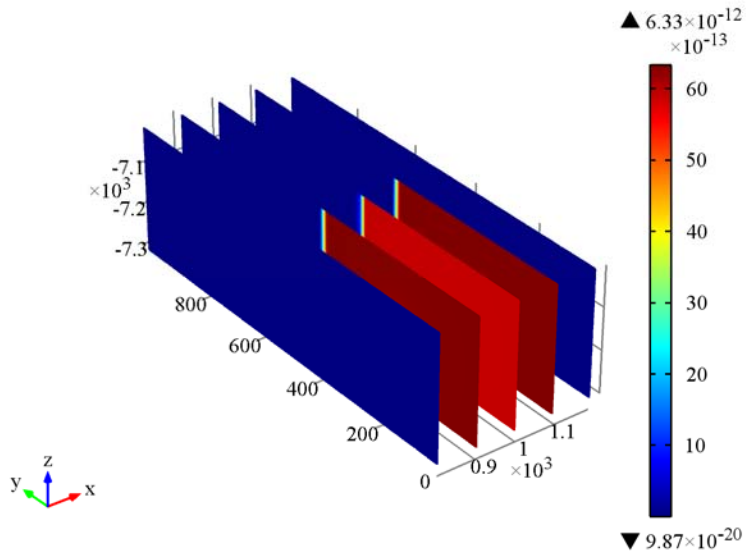
Interpolation 4

2 Component 1 (comp1)

2.1 Definitions

2.1.1 Functions

Step 1

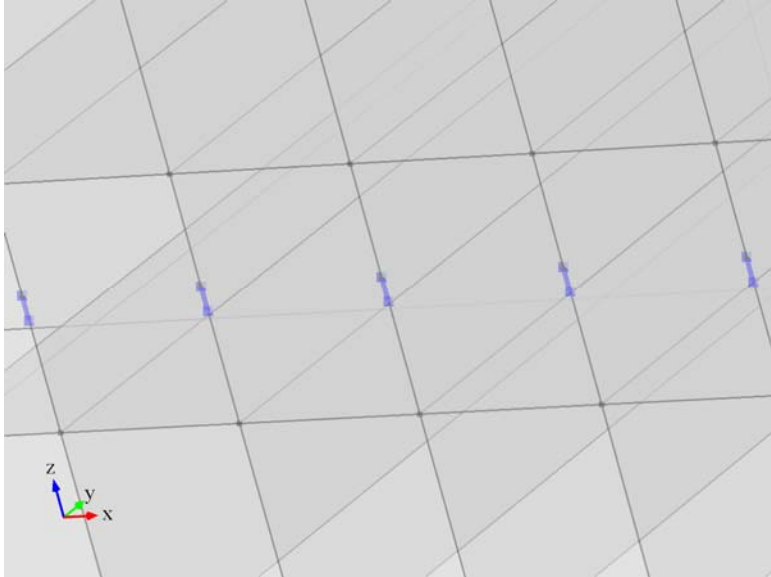| Function name	step1
Function type	Step
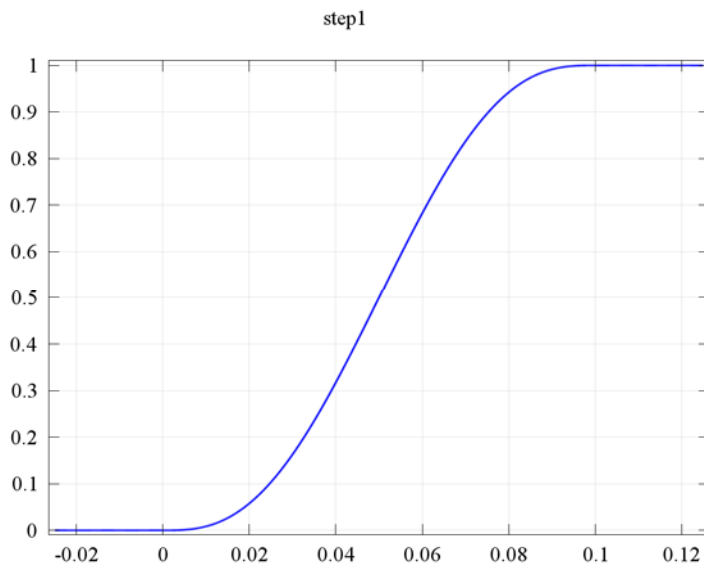
Step 1

2.1.2 Component Couplings

Boundp

Coupling type	Average
Operator name	aveop1

2.1.3 Selections

Perforations

Selection type
Explicit

Selection
Edges 28, 46, 64, 82, 100

Perforations

Fractures

Selection type
Explicit

Selection
Boundaries 10, 12, 15, 18, 20, 23, 26, 28, 31, 34, 36, 39, 42, 44, 46
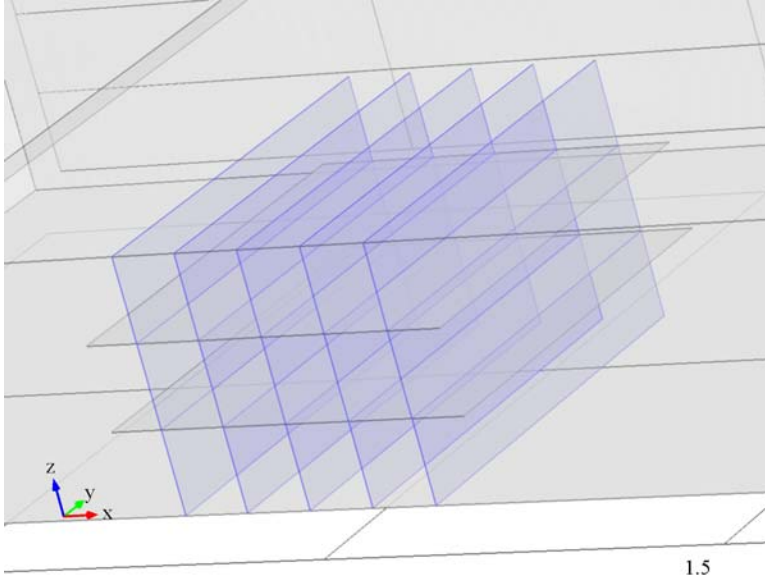
Fractures

Secondary fractures

Selection type
Explicit

Selection
Boundaries 8–9, 14, 17, 22, 25, 30, 33, 38, 41, 45, 47
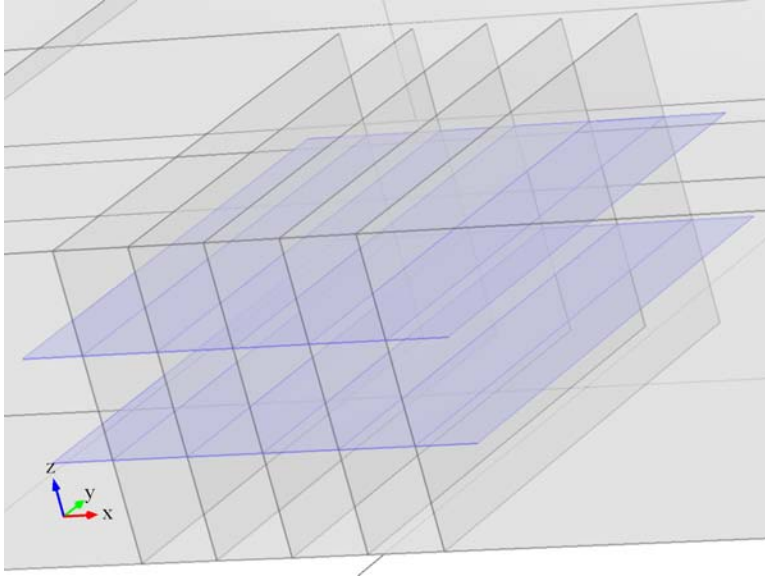
Secondary fractures

Fault

Selection type
Explicit

Selection
Boundary 6
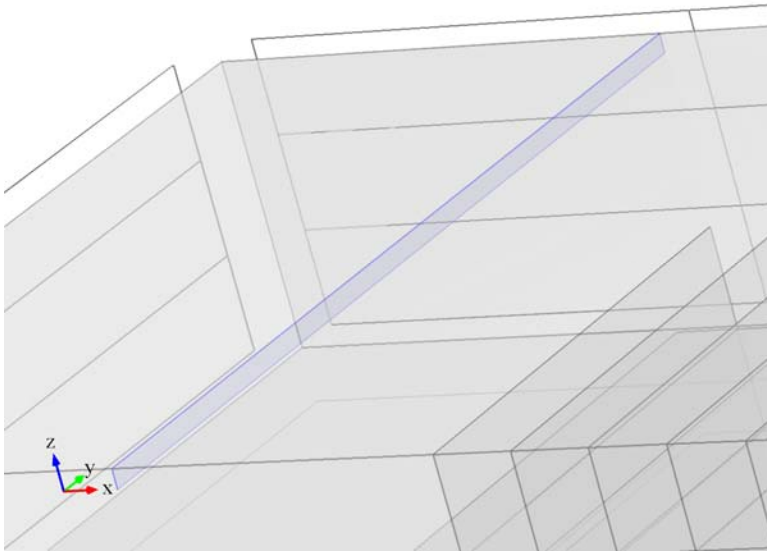
Fault

Fault Edge

Selection type
Explicit

Selection
Edge 12
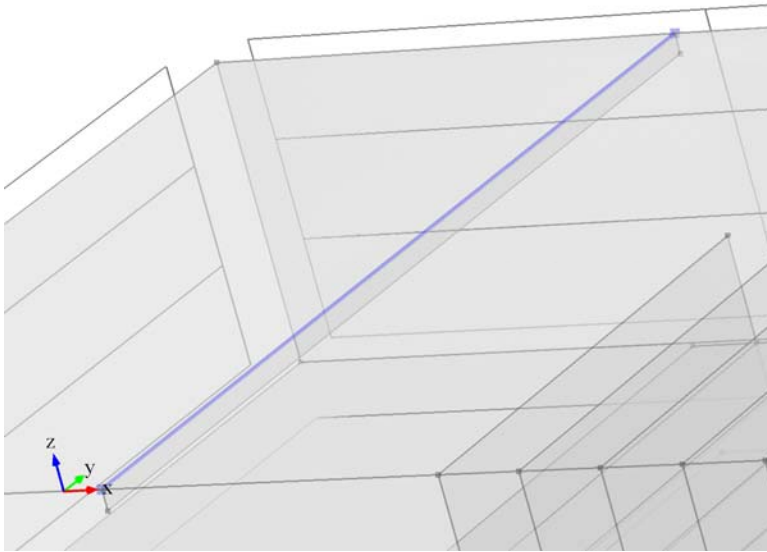
Fault Edge

2.1.4   Coordinate Systems

Boundary System 1

Coordinate system type	Boundary system
Identifier	sys1

206
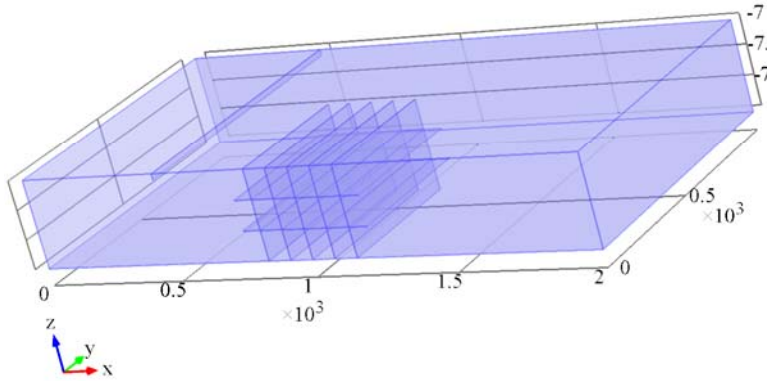
2.2 Darcy's Law (dl)

Darcy's Law

Features

Fluid and Matrix Properties 1
No Flow 1
Initial Values 1
Storage Model 1
Fracture Flow 1
Fracture Flow 2
Fracture Flow 3

2.2.1 No Flow 1
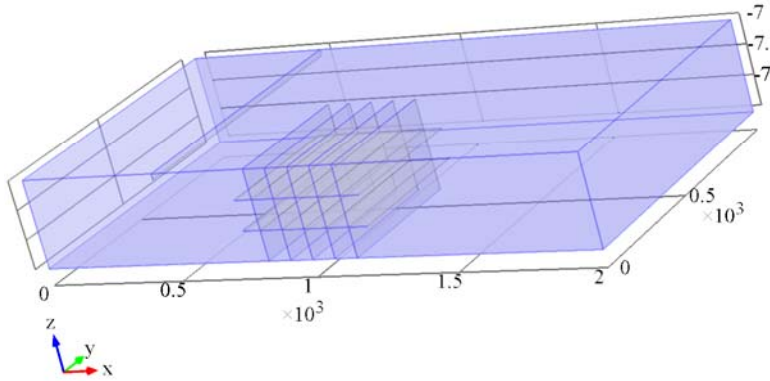
No Flow 1

2.2.2 Storage Model 1
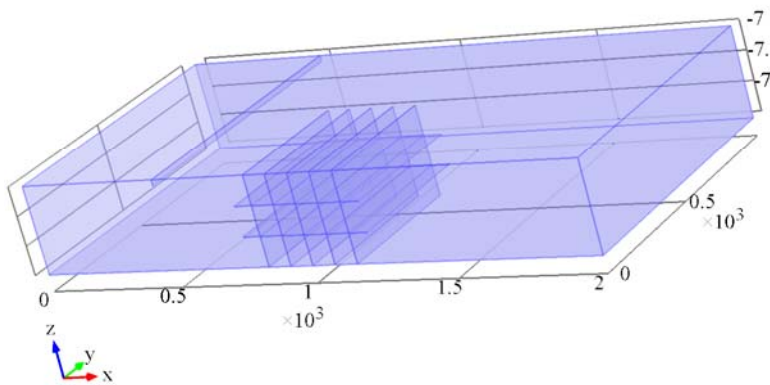

Storage Model 1

Settings

Settings

Description	Value
Density	User defined

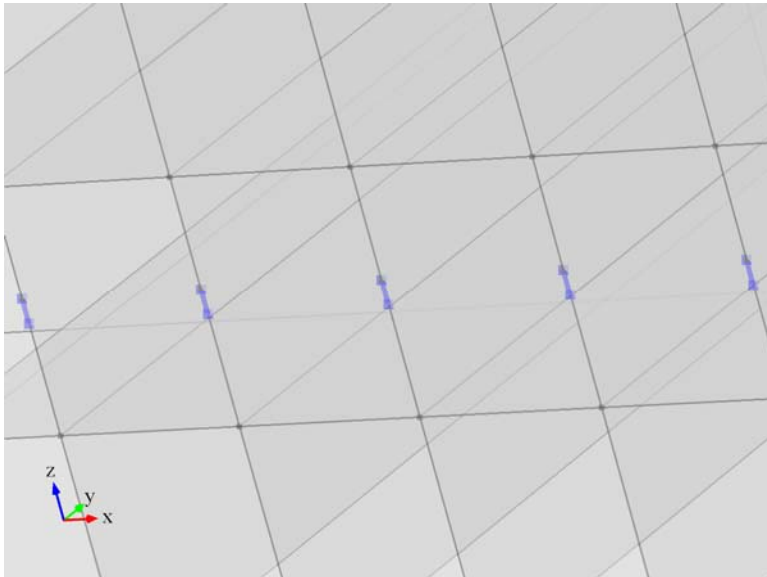| Description	Value
Density	rho_f
Dynamic viscosity	User defined
Dynamic viscosity	eta
Permeability	User defined
Permeability	{{perm_mat, 0, 0}, {0, perm_mat, 0}, {0, 0, perm_mat}}
Porosity	User defined
Porosity	por_mat
Compressibility of fluid	User defined
Compressibility of fluid	fluid_com
Permeability model	Permeability
Storage	Stor1
Effective compressibility of matrix	Shale_com2
Storage	Linearized storage
Porous material	Domain material
Fluid material	Domain material

Weak expressions

Weak expression	Integration frame	Selection
dl.rho*(-dl.S*pt*test(p)+dl.u*test(px)+dl.v*test(py)+dl.w*test(pz))	Material	Domain 1

2.2.3   Fracture Flow 1
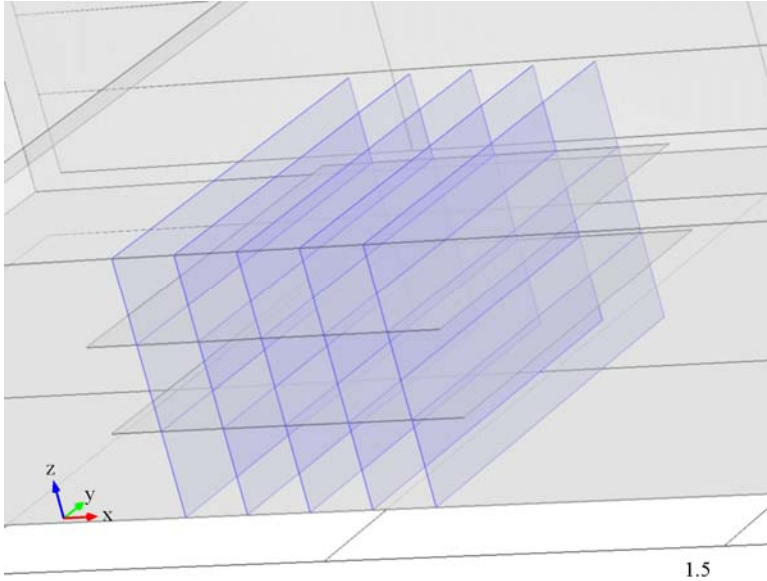
Fracture Flow 1

Pressure 1

Pressure 1

Settings

Settings

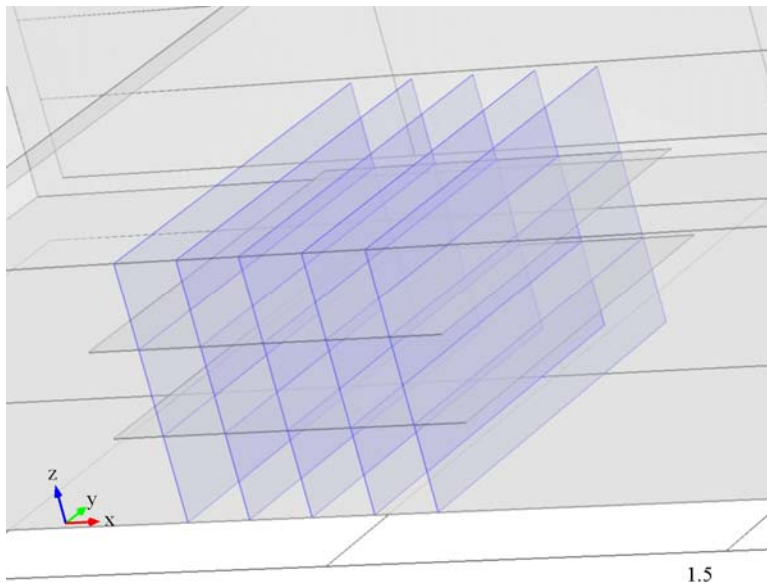| Description	Value
Pressure	(wellbore_pres - init_pres)*step1(t[1/d]) + init_pres

Description	Value
Apply reaction terms on	All physics (symmetric)
Use weak constraints	On

Weak expressions

Weak expression	Integration frame	Selection
(p-dl.p0)*test(-p_lm1)	Material	Edges 28, 46, 64, 82, 100
-test(p-dl.p0)*p_lm1	Material	Edges 28, 46, 64, 82, 100

Fluid and Matrix Properties 1

Fluid and Matrix Properties 1

Settings

Settings

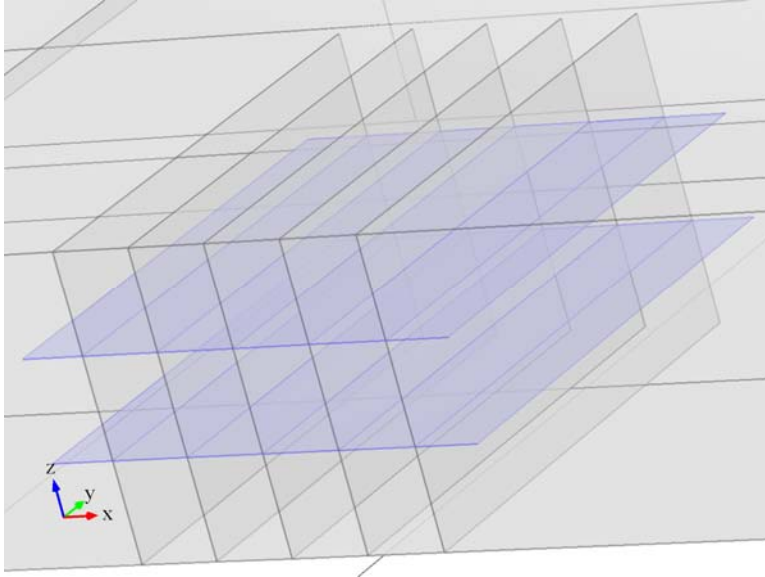| Description	Value
Density	User defined
Density	rho_f
Dynamic viscosity	User defined

Description	Value
Dynamic viscosity	eta
Permeability in fracture	User defined
Permeability in fracture	{{perm_frac, 0, 0}, {0, perm_frac, 0}, {0, 0, perm_frac}}
Porosity in fracture	User defined
Porosity in fracture	por_frac
Permeability model	Permeability
Storage	0
Fracture thickness	aper_frac
Porous material	Boundary material
Fluid material	Boundary material

Weak expressions

Weak expression	Integration frame	Selection
dl.df*dl.rho*(dl.u*test(pTx)+dl.v*test(pTy)+dl.w*test(pTz))	Material	Boundaries 10, 12, 15, 18, 20, 23, 26, 28, 31, 34, 36, 39, 42, 44, 46

2.2.4 Fracture Flow 2

Fluid and Matrix Properties 1

Fluid and Matrix Properties 1

Settings

Settings

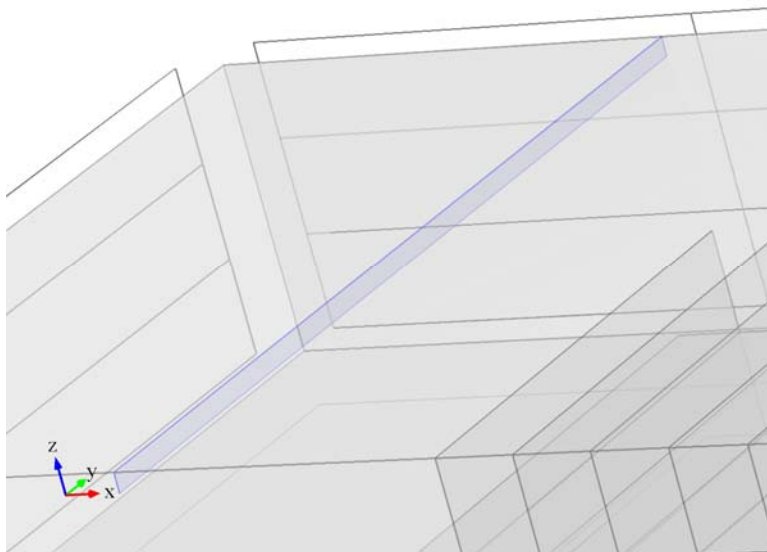| Description	Value
Density	User defined
Density	rho_f
Dynamic viscosity	User defined
Dynamic viscosity	eta
Permeability in fracture	User defined
Permeability in fracture	{{perm_sep, 0, 0}, {0, perm_sep, 0}, {0, 0, perm_sep}}
Porosity in fracture	User defined
Porosity in fracture	por_sep
Permeability model	Permeability

Description	Value
Storage	0
Fracture thickness	aper_sep
Porous material	Boundary material
Fluid material	Boundary material

Weak expressions

Weak expression	Integration frame	Selection
dl.df*dl.rho*(dl.u*test(pTx)+dl.v*test(pTy)+dl.w*test(pTz))	Material	Boundaries 8–9, 14, 17, 22, 25, 30, 33, 38, 41, 45, 47

2.2.5 Fracture Flow 3

Fracture Flow 3

Fluid and Matrix Properties 1

Fluid and Matrix Properties 1

Settings

Settings

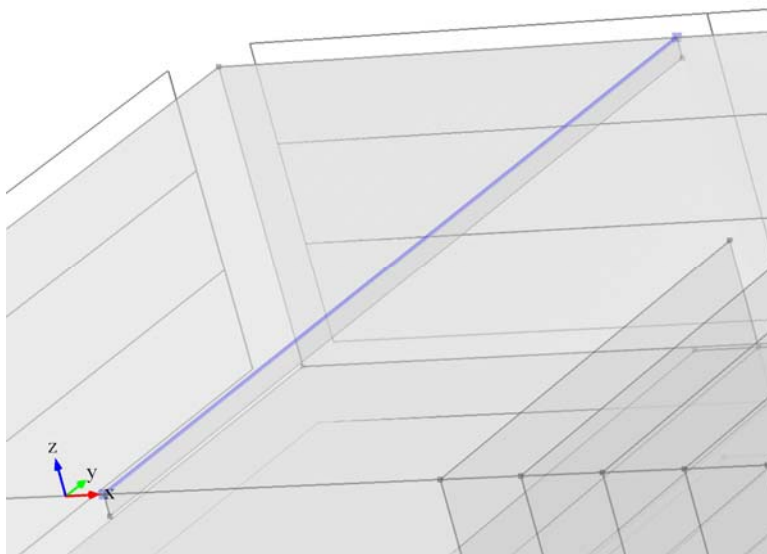| Description	Value
Density	User defined
Density	rho_f
Dynamic viscosity	User defined
Dynamic viscosity	eta
Permeability in fracture	User defined
Permeability in fracture	{{fault_perm, 0, 0}, {0, fault_perm, 0}, {0, 0, fault_perm}}
Porosity in fracture	User defined
Porosity in fracture	por_sep
Permeability model	Permeability
Storage	0

Description	Value
Fracture thickness	aper_sep
Porous material	Boundary material
Fluid material	Boundary material

Weak expressions

Weak expression	Integration frame	Selection
dl.df*dl.rho*(dl.u*test(pTx)+dl.v*test(pTy)+dl.w*test(pTz))	Material	Boundary 6

Pressure 1

Pressure 1

Settings

Settings

Description	Value
Pressure	(pbound(t) - init_pres)*step1(t[1/d]) + init_pres
Apply reaction terms on	All physics (symmetric)
Use weak constraints	On

Weak expressions

Weak expression	Integration frame	Selection
(p-dl.p0)*test(-p_lm1)	Material	Edge 12
-test(p-dl.p0)*p_lm1	Material	Edge 12

2.3   Mesh 2
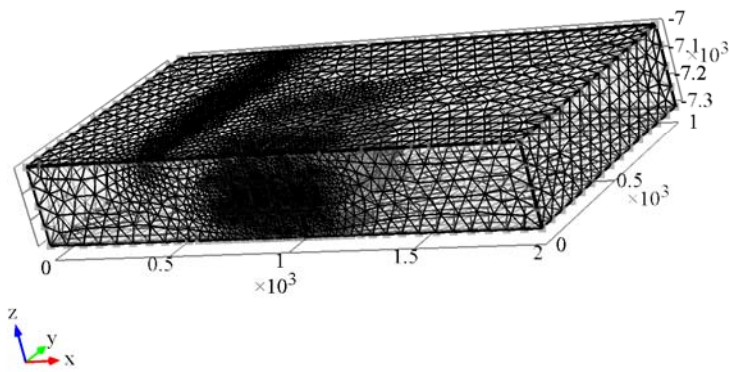
Mesh 2

3   Study 1

3.1   Time Dependent

Study settings

Property	Value
Include geometric nonlinearity	Off

Times: range(0,1,30) range(31,30,361) range(365,365,10950)

Mesh selection

Geometry	Mesh
Geometry 1 (geom1)	mesh1

Physics selection

Physics	Discretization
Darcy's Law (dl)	physics

4   Results

4.1   Derived Values

4.1.1   Wellbore Flux1

Selection

Geometric entity level	Edge
Selection	Edges 28, 46, 64, 82, 100

Data

Name	Value
Data set	Overall data

Expression

Name	Value
Expression	Flow_rate
Unit	m^4/kg
Description	flow rate in MMcf/day

4.1.2   Wellbore Flux2

Selection

Geometric entity level	Edge
Selection	Edges 28, 46, 64, 82, 100

Data

Name	Value
Data set	Overall data

Expression

Name	Value
Expression	Flow_rate
Unit	m^4/kg

219

Name	Value
Description	flow rate in MMcf/day

4.1.3   Fault Boundary pressure

Selection

Geometric entity level	Edge
Selection	Edge 12

Data

Name	Value
Data set	Overall data

Expression

Name	Value
Expression	p
Unit	psi
Description	Pressure

4.1.4   Fault Flux1

Selection

Geometric entity level	Edge
Selection	Edge 12

Data

Name	Value
Data set	Overall data

Expression

Name	Value
Expression	Flow_rate

Name	Value
Unit	m^4/kg
Description	flow rate in MMcf/day

4.1.5   Fault Flux2

Selection

Geometric entity level	Edge
Selection	Edge 12

Data

Name	Value
Data set	Overall data

Expression

Name	Value
Expression	Flow_rate
Unit	m^4/kg
Description	flow rate in MMcf/day

4.2   Plot Groups

4.2.1   Mesh
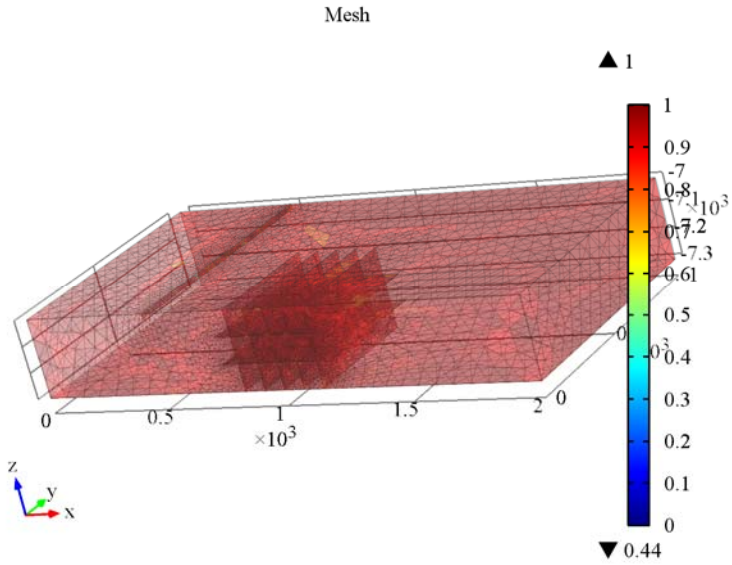
Mesh

Mesh

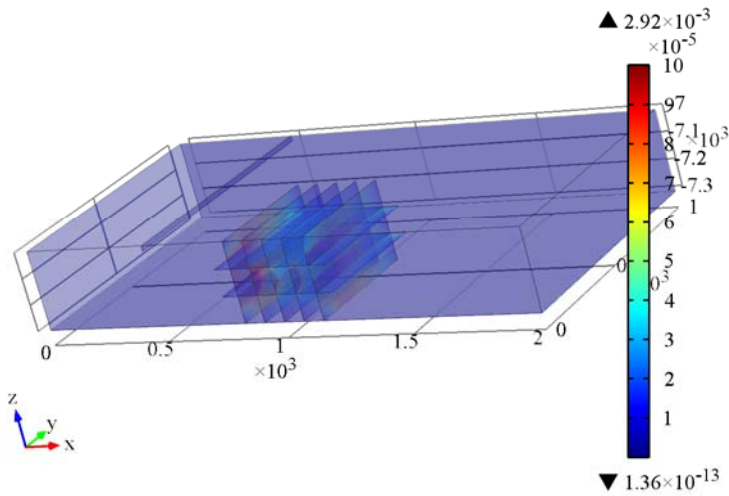### 4.2.2   Pressure (dl) 1

Time=7300 d   Surface: Pressure (Pa)
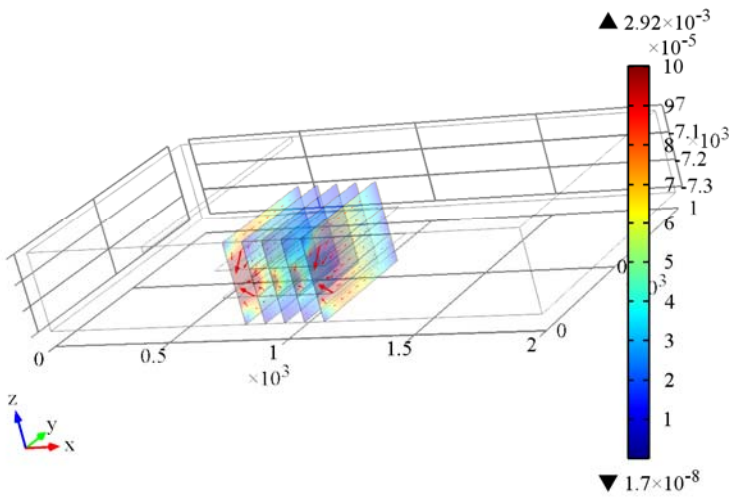
Time=7300 d Surface: Pressure (Pa)

222
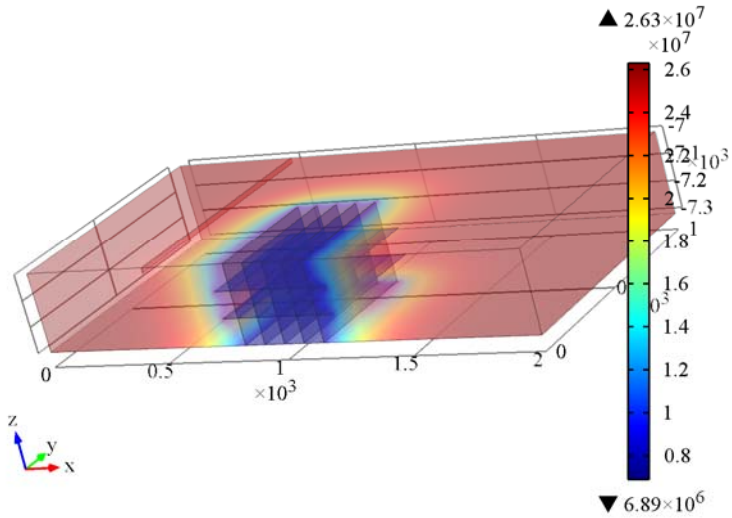
4.2.3 velocity

Time=7300 d Surface: Darcy's velocity magnitude (m/s) Arrow Volume: Darcy's velocity field

4.2.4 Fracture velocity

Time=7300 d Surface: Darcy's velocity magnitude (m/s) Arrow Surface: Darcy's velocity field